



5-2007

Structure and Transport Properties of Epitaxial Oxide Thin Films: From Synthesis to Characterization

Junsoo Shin

University of Tennessee - Knoxville

Recommended Citation

Shin, Junsoo, "Structure and Transport Properties of Epitaxial Oxide Thin Films: From Synthesis to Characterization. " PhD diss., University of Tennessee, 2007.
https://trace.tennessee.edu/utk_graddiss/300

This Dissertation is brought to you for free and open access by the Graduate School at Trace: Tennessee Research and Creative Exchange. It has been accepted for inclusion in Doctoral Dissertations by an authorized administrator of Trace: Tennessee Research and Creative Exchange. For more information, please contact trace@utk.edu.

To the Graduate Council:

I am submitting herewith a dissertation written by Junsoo Shin entitled "Structure and Transport Properties of Epitaxial Oxide Thin Films: From Synthesis to Characterization." I have examined the final electronic copy of this dissertation for form and content and recommend that it be accepted in partial fulfillment of the requirements for the degree of Doctor of Philosophy, with a major in Physics.

E. Ward Plummer, Major Professor

We have read this dissertation and recommend its acceptance:

Arthur P. Baddorf, Hanno H. Weitering, John J. Quinn, Philip Rack

Accepted for the Council:

Dixie L. Thompson

Vice Provost and Dean of the Graduate School

(Original signatures are on file with official student records.)

To the Graduate Council:

I am submitting herewith a dissertation written by Junsoo Shin entitled "Structure and transport properties of epitaxial oxide thin films: from synthesis to characterization." I have examined the final electronic copy of this dissertation for form and content and recommend that it be accepted in partial fulfillment of the requirements for the degree of Doctor of Philosophy, with a major in Physics.

E. Ward Plummer

Major Professor

We have read this dissertation
and recommend its acceptance:

Arthur P. Baddorf

Hanno H. Weitering

John J. Quinn

Philip Rack

Accepted for the Council:

Carolyn Hodges

Vice Provost and

Dean of the Graduate School

(Original signatures are on file with official student records.)

Structure and transport properties of epitaxial oxide thin films: from synthesis to characterization

A Dissertation

Presented for the

Doctor of Philosophy Degree

The University of Tennessee, Knoxville

Junsoo Shin

May 2007

Copyright © 2007 by Junsoo Shin
All rights reserved.

Dedication

To my parents and my wife.

Acknowledgments

There was a big turning point of my study in physics, from field theory to experimental condensed matter physics, which happened at almost 2 years later after joining UT as a doctorate student. At that time, the studying of new area in physics is quite challengeable for me because I have little knowledge of condensed matter physics and experimental experience. It is almost impossible for me to complete my dissertation without many people's helps as well as my deep thirst to learn the fundamental principles in nature.

My first, and most earnest, acknowledgement has to go to my advisors, Ward Plummer and Art Baddorf, who was willing to guide and encourage me to finish my dissertation with their great scientific insight. They have also helped me to open my eyes toward a beauty of the nature and science.

I would also like to acknowledge Sergei Kalinin for teaching SPM and giving lots of scientific advice on ferroelectricity and more. I am sure that I had to climb a steeper mountain for me to finish my dissertation without his helps.

Over the years I have enjoyed the life in lab with Stephen Jesse, Brian Rodriguez, and Jing Zhou. I would like to thank all of them for teaching me PFM and STM and willing to lend a hand whenever I needed while working in the lab.

I would like to thank all people in the Low Dimensional Materials by Design Group at ORNL, especially John Wendelken, Jian Shen, and Gary Ownby who helped me to design and build the new NanoTransport system and maintain that it always

worked very well. In addition to construction of system, I would like to thank Jianxing Ma for giving lots of useful information about PLD growth. I would also like to thank Vickie Barnes for her assistance.

I am very thankful to Von Braun Nascimento for his fantastic LEED I-V calculations to support our experimental results and stimulating discussion about them. I would also like to thank Albina Borisevich for providing TEM images of our epitaxial films to support high quality films.

I would like to appreciate advices and comments coming from the other member of my committee, Hanno Weitering, John Quinn, and Philip Rack.

My final, and most heartfelt, acknowledgment must go to my parents and my wife, Jung-Im Seo. Their support, encouragement, and endless love make it possible for me to complete my work successfully without any difficulties.

Abstract

Epitaxial thin films and heterostructures based on perovskite oxides have attracted significant attention in physics since perovskites exhibit an enormous range of electrical, magnetic, and optical properties, making them exciting systems for studies of the fundamental physical mechanisms of interactions between electron, lattice, and spin degrees of freedom. This dissertation has been focused on ferroelectricity in low-dimensional ferroelectric materials using ultra-thin ferroelectric epitaxial films (BaTiO_3) with a metallic electrode (SrRuO_3) by studying polarized ordering of the crystal structure and electronic transport through the films. High quality and highly oxidized epitaxial films are a prerequisite for the clear observation of physical properties such as ferroelectricity which depends on a sensitive balance of lattice structure, dynamics, and charge distribution. Measurements in low dimensional, ultra-thin films require a controlled surface status through *in-situ* characterization. As is demonstrated here, fundamental physical phenomena on surfaces and in ultra-thin films are easily modified due to reactivity in ambient air, even for oxide materials generally considered inert. This study is centered on *in-situ* low energy electron diffraction and scanning tunneling spectroscopy of BaTiO_3 films grown on SrRuO_3 electrodes on a SrTiO_3 substrate. Results show out-of-plane polarized structure and polarization switching, which provide evidence of ferroelectricity in films down to 4 ML. Surface reconstruction in 1-2 ML thick BaTiO_3 films is seriously affected by the interface between BaTiO_3 films and SrRuO_3 bottom electrode. Our observation in epitaxial BaTiO_3 films indicates the existence of ferroelectricity with a lower limit (4 ML) for the minimum thickness than

theoretical expectation (6 ML), which results from the difference of film stress, termination on films, and depolarizing screening.

Table of Contents

1	Introduction.....	1
1.1	Physics and properties of ferroelectric materials	5
1.1.1	Background of ferroelectrics	5
1.1.2	Theory of the ferroelectricity (Ginzburg-Landau theory)	9
1.2	Heteroepitaxial oxide thin films	14
1.2.1	Epitaxial growth	14
1.2.2	Ferroelectric oxide thin films	18
1.2.3	Metallic ruthenium oxide thin films	23
1.3	The ferroelectric thickness limit	26
1.4	Ferroelectric tunneling junction	29
2	Characterization Techniques	34
2.1	Laser molecular beam epitaxy	34
2.2	X-ray diffraction	37
2.2.1	θ - 2θ scan	39
2.2.2	ω -scan	39
2.3	Electron diffraction	41
2.3.1	Reflective high energy electron diffraction	41
2.3.2	Low energy electron diffraction	46
3.3.2.1	Diffraction pattern formation	46

3.3.2.2	Surface Structure determination by LEED	50
2.4	Scanning Probe Microscopy	59
2.4.1	Scanning tunneling microscopy and spectroscopy	60
2.4.2	Atomic force microscopy	64
3	Epitaxial thin film growth	67
3.1	SrTiO ₃ substrate preparation	67
3.2	Epitaxial SrRuO ₃ thin films	72
3.3	Epitaxial BaTiO ₃ /SrTiO ₃ thin films	76
3.4	Epitaxial BaTiO ₃ /SrRuO ₃ /SrTiO ₃ multilayers	89
4	Surface stability of epitaxial SrRuO ₃ films: the need for <i>in-situ</i> analysis	94
4.1	Introduction	94
4.2	Thermodynamic analysis	95
4.3	Experiment and results	100
4.3.1	Surface stability	100
4.3.2	STM analysis	101
4.3.3	Thermal Desorption Spectroscopy	103
4.3.4	Electron Spectroscopies of Surface Chemistry of SrRuO ₃	106
4.3.5	RHEED patterns before and after cleaning SrRuO ₃ films	115
4.4	Discussion	119
4.5	Conclusions	121

5	Crystal structure of thin films, <i>in-situ</i> analysis	123
5.1	Epitaxial SrRuO ₃ thin films: atomic structure and electronic properties ...	124
5.2	Epitaxial BaTiO ₃ /SrRuO ₃ /SrTiO ₃ multilayers: polar structure in ultra-thin films	131
5.2.1	The LEED experiment	131
5.2.2	The surface structure of ultra-thin BaTiO ₃ films	133
5.2.2.1	The clean surface of BaTiO ₃	133
5.2.2.2	The surface of BaTiO ₃ exposed to H ₂ O	151
5.2.3	The surface reconstruction of 1~2 ML BaTiO ₃ films	159
6	Ferroelectric tunnel junctions at the nanoscale and future directions	164
6.1	Ferroelectricity of ultra-thin BaTiO ₃ films	164
6.2	Summary and future directions	169
	References	173
	Appendix	187
	<u>A.1</u> Chamber Construction	188
	Vita	190

List of Tables

1.1	Summary of possible epitaxial BaTiO ₃ phases	20
5.1	Final structure refinement for 10 ML BaTiO ₃ films	141
5.2	Rumpling parameters for 10 ML BaTiO ₃ films	142
5.3	Final structure refinement for 4 ML BaTiO ₃ films	147
5.4	Rumpling parameters for 4 ML BaTiO ₃ films	149
5.5	Final structure refinement for 10 ML BaTiO ₃ films exposed to H ₂ O	156
5.6	Rumpling parameters for BaTiO ₃ films exposed to H ₂ O	158

List of Figures

1.1	Ideal perovskite structure for an ABO_3 compound	8
1.2	Hysteresis of the polarization P as a function of the field E for ferroelectric	8
1.3	Various structure of barium titanate as a function of temperature	10
1.4	The free energy as a function of polarization for a ferroelectric	12
1.5	Energy barrier of thin film surface	16
1.6	The main epitaxial growth modes	17
1.7	Possible domain structure of tetragonal (100) thin films at RT	20
1.8	Phase diagram of epitaxial BaTiO_3 by semi-empirical method	21
1.9	Diagram of epitaxial BaTiO_3 by DFT	22
1.10	Ruddlesden-popper homologous series $\text{Sr}_{n+1}\text{Ru}_n\text{O}_{3n+1}$	24
1.11	History of ferroelectric thickness limit	30
1.12	The current-voltage characteristics of FTJ	33
2.1	Synthesis and characterization	36
2.2	Schematic of four-circle x-ray diffractometry	38
2.3	Probing of the crystalline planes parallel to the surface	40
2.4	RHEED patterns dependent on the surface roughness of BaTiO_3 films	43
2.5	Mechanisms of RHEED oscillations during growth of a monolayer	44
2.6	Principles of 2 dimensional diffraction pattern formations	48
2.7	Schematic of LEED set-up	50
2.8	The position vector of atoms in j^{th} unit cell	51

2.9	Kinetic approximation	53
2.10	Hierarchy of dynamic (multiple scattering) LEED intensity evaluation	54
2.11	Multiple scattering	55
2.12	Comparison of kinematic spectrum and dynamical spectrum	57
2.13	Atomically resolved STM images of Si (111) surface at RT	61
2.14	The principle of scanning tunneling microscopy	62
2.15	The principle of atomic force microscopy	65
2.16	Distance dependence of atomic forces	65
3.1	Schematic diagram of SrTiO_3 crystal structure in cubic unit cell at RT	68
3.2	Chemical etching treatment	69
3.3	<i>Ex-situ</i> AFM topographic images of (100) SrTiO_3 substrates	71
3.4	In-plane lattice mismatch between pseudocubic SrRuO_3 and cubic SrTiO_3 at RT	73
3.5	SrRuO_3 films growth	74
3.6	In-plane lattice mismatch between tetragonal BaTiO_3 and cubic SrTiO_3 at RT	78
3.7	The surface of BaTiO_3 films after growth	81
3.8	RHEED oscillation and roughness of BaTiO_3 film	82
3.9	XRD measurements	85
3.10	Cross-sectional TEM studies of BaTiO_3 thin films	87
3.11	In-plane lattice mismatch between tetragonal BaTiO_3 and fully strained SrRuO_3 films grown on SrTiO_3 at RT	91

3.12	BaTiO ₃ films growth on SrRuO ₃ /SrTiO ₃	92
4.1	Thermodynamic analysis	96
4.2	<i>Ex-situ</i> LEED pattern of SrRuO ₃ films at RT	101
4.3	STM images of SrRuO ₃ film dependent on temperature.....	102
4.4	Depth of Pits on the surface of SrRuO ₃ films	104
4.5	TDS from SrRuO ₃ film in high vacuum as a function of temperature	105
4.6	HREELS experiment	107
4.7	XPS analysis for O and Ru spectra	109
4.8	XPS analysis for Sr	112
4.9	Intensity ratios from XPS as a function of annealing temperature	114
4.10	RHEED patterns of air-exposed SrRuO ₃ films at different temperatures	117
4.11	Schematics of possible surface configurations	120
5.1	Atomically resolved STM images of SrRuO ₃ films	126
5.2	<i>In-situ</i> p(2x2) LEED images of SrRuO ₃ films taken at RT	127
5.3	Line profile of surface defect on SrRuO ₃ films	128
5.4	Surface defects in ruthenates	129
5.5	Schematics of the fully relaxed structure near the surface of BaTiO ₃	135
5.6	<i>In-situ</i> (1x1) LEED images of 10 and 4 ML thick BaTiO ₃ films taken at RT ...	137
5.7	I-V curves of 10 ML BaTiO ₃ films	138
5.8	R _p contour plot for 10 ML BaTiO ₃ films	140
5.9	Final structure refinement for 10 ML BaTiO ₃ films	141

5.10	Polarization in 10 ML BaTiO ₃ films	143
5.11	I-V curves of 4 ML BaTiO ₃ films	145
5.12	R _p contour plot for 4 ML BaTiO ₃ films	146
5.13	Final structure refinement for 4 ML BaTiO ₃ films	147
5.14	Polarization in 4 ML BaTiO ₃ films	149
5.15	LEED patterns for BaTiO ₃ films	153
5.16	Experimental I-V curves of 10 ML BaTiO ₃ films without and with exposure to H ₂ O	153
5.17	Optimizing R _p factors	155
5.18	Final structure refinement for 10 ML BaTiO ₃ films exposed to H ₂ O	156
5.19	I-V curves of BaTiO ₃ films exposed to H ₂ O	157
5.20	Polarization in BaTiO ₃ films exposed to H ₂ O	158
5.21	Evolution of LEED patterns dependent on BaTiO ₃ film thickness	161
5.22	Experiment I-V curves of different thick BaTiO ₃ films	161
5.23	STEM for 10 ML BaTiO ₃ films on SrRuO ₃ /SrTiO ₃	163
6.1	Experimental setting for FTJ using STS	167
6.2	I-V curves for FTJ	168
6.3	Two loops of I-V curves for FTJ	170
6.4	IV curves of non-ferroelectric 10 ML SrTiO ₃ films on SrRuO ₃ /SrTiO ₃	170

Chapter 1

Introduction

Transition metal oxides (TMOs) display diverse and fascinating properties covering a wide range of physics and materials properties. The nature of cation-oxygen bonding results in electronic properties that are described using covalent bonding for one system and highly ionic for the other, but often best understood by combining aspects of both approaches. This interplay in cation-oxygen bonding characteristics yields TMOs possessing a wide range of electronic properties, for example with electrical conductivity ranging from metals, and superconductors, to insulators, ferromagnets, and ferroelectrics. These properties can in many cases be tuned by electronic doping or by changing temperature, leading to phase transitions with an abrupt change in one or more physical properties, which can be interpreted by a symmetry-based analysis. For example, ferroelectric oxide materials exhibit phase transitions given by crystallographic structure change and cation-oxygen displacement related to symmetric breaking in crystals. Therefore, the phase transitions due to symmetric ordering exhibit different domain structures with characteristic physical properties in ferroelectric oxide materials.

In 1937, Landau [1] described the equilibrium behavior of a system near a phase transition based solely on symmetry considerations. This phase transition can be expressed in terms of an order parameter, a physical entity that is zero in the high-symmetry (disordered) phase, and changes continuously to a finite value once the symmetry is lowered. For the case of a paraelectric-ferroelectric transition, the order

parameter is the polarization P . The phase transition in ferroelectric materials is related to symmetric changes by temperature-dependent structure deformation, which forms the spontaneous polarization P . For example, highly symmetrical ferroelectric materials can have a paraelectric cubic phase with no polarization P and lower symmetrical ferroelectric materials can have a tetragonal phase with polarization P due to cation-oxygen displacement.

Ferroelectricity is a collective phenomenon, associated with the alignment of localized dipoles within a “correlation volume”, producing a polarization [2]. These dipoles spontaneously form from a “soft phonon” response of the atomic structure displacing the center of the ion cores and electrons. The strong, long range electrostatic interaction of the dipoles is responsible for the correlation of adjacent cells. This interaction is highly anisotropic and consists of short-range repulsion for parallel dipoles perpendicular to the polarization axis and long-range Coulomb attraction for parallel dipoles along the polarization axis. Ferroelectric phase transitions are highly dependent on the competition between short-range and long-range Coulomb forces. In bulk ferroelectrics, the long range attraction can always dominate, so that macroscopic domains can exist.

The properties of thin films often differ significantly from those of the bulk. One obvious source of difference is the magnitude of the strain resulting from lattice-matching between the films and the substrate. In the case of ferroelectric thin films, there are convincing experimental evidences that the strain due to lattice and/or thermal expansion mismatch between a film and a substrate may result in dramatic increases in phase transition temperatures as well as large variations of domain structures. However,

very few materials have a small lattice mismatch between the film and substrate, which is required for fully strained epitaxial films. Practically, it is extremely difficult to grow highly oxidized and highly strained epitaxial thin films with relatively large lattice mismatch without lattice relaxation. Therefore, understanding the growth mechanism for high quality, highly oxidized, and highly strained epitaxial thin films is indispensable to study physics in low dimensions different from physical phenomena in bulk materials.

Even well grown ferroelectric films can show new behavior such as a size dependence of the paraelectric-to-ferroelectric “phase transition,” or “critical thickness,” below which the ferroelectric phase disappears. This critical thickness can be due to the increased contribution of short-range repulsive forces relative to long-range attractive forces imposed by the geometry and by boundary conditions such as the depolarizing electrostatic field formed by the effective charge at the surface, which increasingly counters the polarization. However, such a critical thickness is not universally accepted [3,4]. Meyer and Vanderbilt [4] reported the absence of a critical size of ferroelectricity because the observed suppression of ferroelectricity in thin films is not a purely intrinsic effect caused solely by the presence of the surface, but is related to extrinsic factors like perturbations of the chemical composition of the surface, surface-induced strains, or variations in boundary conditions. For this reason, strong debate has recently erupted over the existence of a critical size for ferroelectricity [3,4,5,6,7,8,9,10,11,12,13].

An additional novel feature of thin film ferroelectrics is the “ferroelectric tunneling effect,” which suggests that the electronic tunneling through a thin ferroelectric film should depend on the polarization direction. If the thickness of a ferroelectric layer is small but above the critical thickness, polarization reversal in the ferroelectric barrier

may produce a change in the potential profile across the junction and lead to a polarization dependent resistance by the influence of both intrinsic and extrinsic effects such as the converse piezoelectric effect and the depolarizing field effect. There is currently little understanding of the relationship between transport properties and polarization effects due to a lack of valid experimental data and to the complex nature of the ferroelectric-electrical contact interaction. This latter can include electronic, phonon, and strain effects. The following fundamental questions remain: “Is the potential barrier to tunneling influenced by the polarization in a ferroelectric even without influence by boundary conditions? Is the tunneling altered by polarization switching?”.

These ferroelectric transitions and transport properties in ultra-thin films must be explored with in situ techniques highly sensitive to the surface after careful synthesis. The approach in this dissertation includes combining low energy electron diffraction (LEED) and scanning tunneling spectroscopy (STS) after in-situ synthesis by laser molecular beam epitaxy (MBE). To understand the growth mechanism for high quality of thin films, atomic force microscopy (AFM), x-ray diffraction (XRD), and transmission electron microscopy (TEM) are explored. Additionally, topographical images of scanning tunneling microscopy (STM) are studied to show atomic structure and electronic properties on the atomically flat surface of thin films, which are non-cleavable and non-layered TMOs with a 113-perovskite structure. For the structure analysis of atomic positions in the surface unit cell, LEED-IV analysis can produce an accuracy of less than a few thousandths of a nanometer. For this reason, *in-situ* LEED-IV characterization of epitaxial ultra-thin ferroelectric films has been applied for the first time to explore the ferroelectric thickness limit by checking the cation-oxygen displacement and polar

ordering. Due to the unique abilities of STM to study low dimensional systems in real space, direct mapping of defect ordering and observation of reconstruction on the surface can be demonstrated. Finally, only Scanning Tunneling Spectroscopy can provide information on ferroelectric tunneling junctions while avoiding the defect effects which dominate macroscopic measurements and thus distinguish intrinsic and extrinsic effects.

1.1 Physics and properties of ferroelectric materials

1.1.1 Background of ferroelectrics

Ferroelectricity is perhaps even today almost as much an art as it is a science. It is now some 85 years since the phenomenon known as ferroelectricity was first recognized in Rochelle salt [14]. However, the term ferroelectricity was not commonly in use much before the early 1940s, partly due to the fact that Rochelle salt remained the only known example of the phenomenon for over a decade after the initial discovery, but also because the full significance of the phenomenon in terms of a theoretical interpretation was not given until 1933 [15]. One of the major turning points in ferroelectricity came during the 1940s with the discovery of a number of simple mixed oxides that crystallize with the perovskite structure. Prior to the perovskite era, ferroelectricity was mostly a scientific curiosity unique to two rather friable water-soluble crystals, Rochelle salt and KH_2PO_4 (KDP) and at that time was thought to be an order-disorder phenomenon associated with the hydrogen bonds. These compounds

contained hydrogen bonds led to the erroneous assumption that the existence of hydrogen bonding is a precondition for ferroelectricity and therefore the search for new ferroelectric materials performed over these two decades was limited to hydrogen-containing compounds.

The situation changed in the early forties when the search for materials with high dielectric constants led to the discovery of ferroelectricity in the perovskite BaTiO_3 simultaneously in the USA, Russia, and Japan [16,17,18]. The discovery of ferroelectricity in BaTiO_3 and related ferroelectric perovskites was extremely important, as it demonstrated for the first time that ferroelectricity could exist in simple oxide materials, and it was not always associated with hydrogen bonding. These materials rapidly became widespread due to high chemical stability, good mechanical properties, and ease of preparation. In addition, the relatively simple perovskite structure made ferroelectric perovskites more amenable for theoretical treatment originating a number of models ranging from the original “rattling atom” model to soft-mode based description of ferroelectricity and thermodynamic Ginzburg-Devonshire type models [19].

Ferroelectricity is defined as a physical phenomenon in which a spontaneous electric dipole moment can be reoriented from one crystallographic direction to another by an applied electric field. Materials which show this ferroelectricity are called ferroelectrics. Among the different ferroelectrics, oxides showing a perovskite structure or a related structure are of particular importance. The ideal perovskite structure of the general formula ABO_3 is cubic with the A and B cations situated at the corners and the center of the cube respectively, and the O^{2-} anions at the centers of the faces. The BO_6 octahedra are corner-linked. In the cubic high temperature phase, this material does not

display any spontaneous polarization and, hence, the system is paraelectric. Upon cooling, a phase transition occurs during which the positive and negative metal ions displace with respect to each other, leading to a tetragonal deformation. Due to the asymmetry in this displacement, a spontaneous polarization in the direction of the tetragonal axis appears. [Figure 1.1](#) schematically shows the displacement of the ions in an ABO_3 perovskite structure due to an applied electric field. Ferroelectric materials exhibit an electric dipole moment, even in the absence of an external electric field [\[20\]](#). Ferroelectrics possess at least two equilibrium orientations of the spontaneous polarization vector, \mathbf{P}_s . The spontaneous polarization vector may be switched between those orientations by application of an oppositely oriented electric field [\[21\]](#).

The key experiment for ferroelectricity is the existence of a hysteresis loop between polarization and electric field, analogous to the ferromagnetic hysteresis loop between magnetization and magnetic field. The characteristic hysteresis of the polarization P , as a function of the field E , is shown in [Figure 1.2](#) for single-domain single crystals and poly-domain samples [\[22\]](#). The polarization at zero field is called remanent polarization P_r . At zero field the electric displacement within a single domain has two values corresponding to the opposite orientations of the spontaneous polarization, which is reoriented when the electric field E applied opposite to the polarization exceeds the coercive field E_c leading to the unidirectional jumps in the P - E curve. In a multi-domain crystal the average zero-field displacement can have any value between these two extremes.

As in ferromagnetic materials, ferroelectrics form domain structures. A domain is a region where there is a uniform direction for the spontaneous polarization. In the

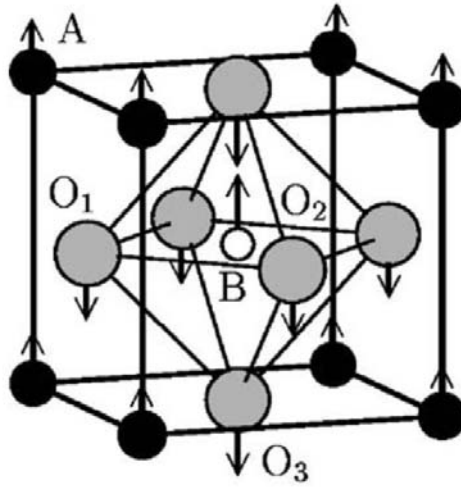


Figure 1.1: Ideal perovskite structure for an ABO_3 compound. The z-polarized soft-mode atomic displacements are indicated by arrows. Figures adapted from [20].

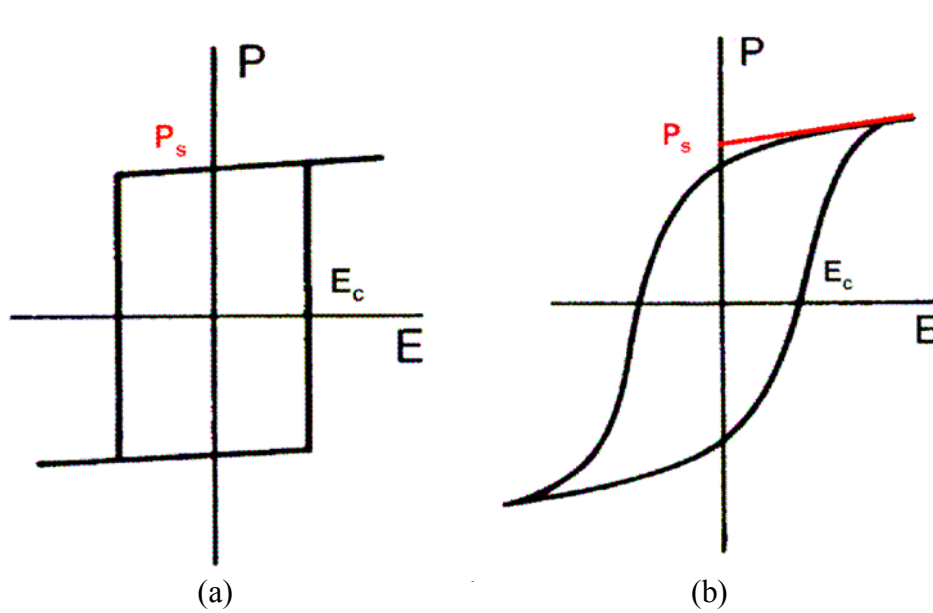


Figure 1.2: Hysteresis of the polarization P as a function of the field E for ferroelectric. (a) Single-domain. (b) Poly-domain materials. Figures adapted from [22].

case of bulk BaTiO_3 , there are three phase transitions and four possible domain structures dependent on temperature. It undergoes a succession of phase transitions, from the high-temperature high-symmetry cubic perovskite phase to slightly distorted ferroelectric structures with tetragonal, orthorhombic, and rhombohedral symmetry [Figure 1.3]. The different phases of BaTiO_3 are a system with a degenerate order parameter; a single order parameter (essentially the displacement of the Ti from the centre of its octahedral coordination polyhedron) can initially act along one of three perpendicular directions. The subsequent phase transitions occur as the second and third components of the order parameter vector are activated.

1.1.2 Theory of the ferroelectricity (Ginzburg-Landau theory)

In 1937 and 1945, Landau [1] and Ginzburg [23] expanded the thermodynamical potential in the vicinity of the phase transition temperature as a power series and introduced the spontaneous polarization as an order parameter where only symmetry-compatible terms are retained. This symmetry-based treatment of phase transition [1] was first applied to the case of ferroelectrics by Devonshire [19] with assumption of describing both ferroelectric and non-ferroelectric phases by the same polynomial with specific reference to BaTiO_3 .

In general, a fundamental postulate of thermodynamics applied to a ferroelectric is that its free energy F can be expressed as a function of several variables such as polarization, strain field, and temperature. However, in order to be more specific, we can

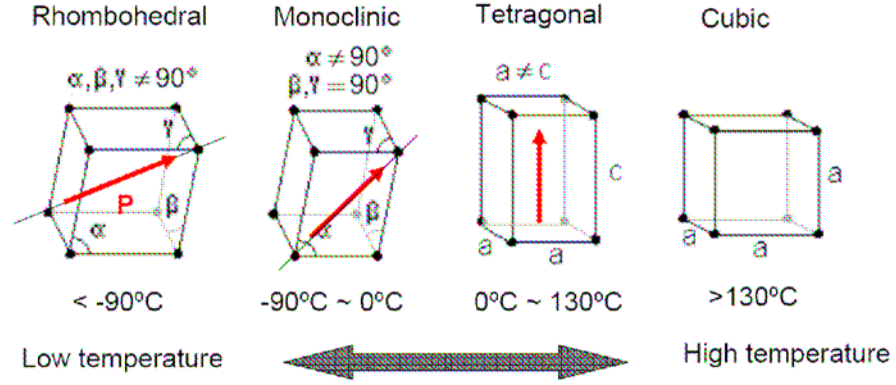


Figure 1.3: Various structure of barium titanate as a function of temperature. Figures adapted from [22].

consider a simple example where we expand the free energy in terms of a single component of the polarization P . Close to the phase transition, the free energy can be written as a functional of powers of the order parameter P

$$F(P, T) = \frac{1}{2} g_2 P^2 + \frac{1}{4} g_4 P^4 + \frac{1}{6} g_6 P^6 - \frac{1}{2} P E, \quad (1.1)$$

where the coefficients g_2 , g_4 , and g_6 depend on the temperature and g_2 and g_6 are both positive in all known ferroelectrics [2]. In particular the coefficient g_2 may be approximately by

$$g_2 = C^{-1}(T - T_c), \quad (1.2)$$

resulting of a temperature expansion around T_c . The equilibrium configuration is determined by finding the minima of F with the electric field $E = 0$,

$$\frac{\partial F}{\partial P} = 0 = P(g_2 + g_4 P^2 + g_6 P^4) \quad (1.3)$$

$$\frac{\partial^2 F}{\partial^2 P} = \chi^{-1} = g_2 + 3g_4 P^2 + 5g_6 P^4 > 0. \quad (1.4)$$

Paraelectric Phase

One of the solution for [Equations \(1.3\) and \(1.4\)](#) can be $P = 0$ with $g_2 > 0$, which corresponds to the condition of the paraelectric phase. From [Equation \(1.2\)](#), g_2 can be expressed by the susceptibility χ , for which a Curie-Weiss Law is found with a critical exponent $\gamma = 1$:

$$\chi(T) = \frac{C}{T - T_c} \propto (T - T_c)^{-\gamma}; \quad \gamma = 1. \quad (1.5)$$

Ferroelectric Phases – Second order (continuous) Transition

If we take $g_4 > 0$ and neglect the coefficient g_6 , then a continuous transition occurs at $T = T_c$ and the free energy will evolve continuously as a function of decreasing temperature from upper curve ($T > T_c$) in [Figure 1.4\(a\)](#) to the lower curve ($T < T_c$), that has minima at finite polarizations $P = \pm P_s$. Therefore, we can see that a spontaneous polarization P_s exists for $T < T_c$ and increases with decreasing temperature from the point $T = T_c$, which is given by

$$P_s = \left(\frac{T_c - T}{Cg_4} \right)^{1/2} \propto (T_c - T)^\beta \quad (1.6)$$

where the critical exponent β assumes the values $1/2$. [Figure 1.4\(a\)](#) shows that the free energy is close to the second order phase transition for different temperatures as a function of the order parameter P_s^2 .

The specific heat is obtained by the derivative of the entropy with respect to the temperature. This gives

$$\Delta C_v = C_v(T = T_c^+) - C_v(T = T_c^-) \quad \text{where} \quad C_v \equiv -T \frac{\partial^2 F}{\partial T^2} \quad (1.7)$$

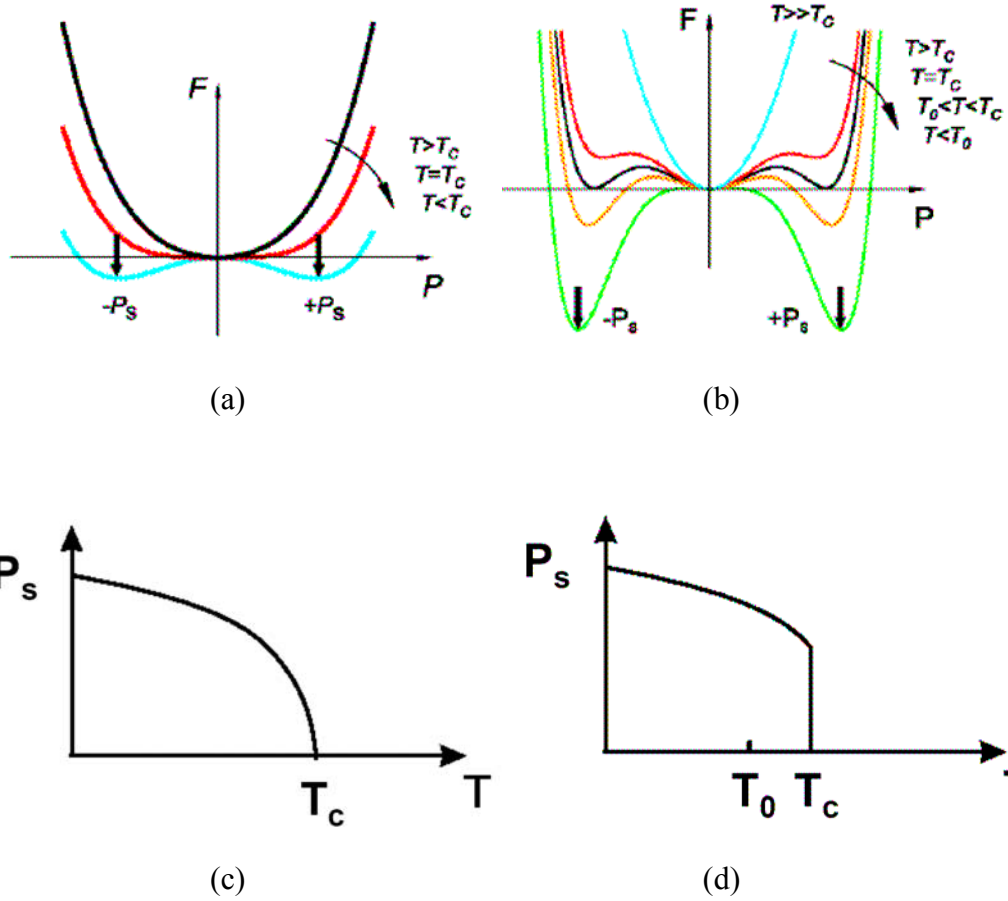


Figure 1.4: The free energy as a function of polarization for a ferroelectric. (a) Continuous and (b) discontinuous phase transition as a function of temperature. Spontaneous polarization $P_s(T)$ as a function of temperature for (c) continuous and (d) discontinuous transition. Figures adapted from [22].

Then, we obtain

$$\Delta C_v = \frac{T_c}{2g_4 C^2} \quad (1.8)$$

for the Landau expression for this quantity.

Ferroelectric Phases – Discontinuous Transition

If we choose $g_4 < 0$ and $g_6 > 0$, discontinuous phase transitions can occur, which means the paraelectric phase coexists with the ferroelectric phase in a certain regime of temperature. This is sketched in [Figure 1.4\(b, d\)](#). At the regime of $T \gg T_c$ and $T < T_o$, [Figure 1.4\(b\)](#) shows both stable paraelectric and ferroelectric phases, respectively. However, during cooling from stable paraelectric phase, secondary minima at finite polarizations become visible. In the regime of $T > T_c$, the paraelectric phase is stable whereas the ferroelectric phase is metastable. Similarly, in the regime between T_c and T_o , the metastable paraelectric phase coexists with the stable ferroelectric phase. Somewhere during cooling through this regime, the first order phase transition to the ferroelectric state will occur with a corresponding jump of the spontaneous polarization from zero to a finite value.

Most perovskites are materials with discontinuous phase transitions including $\text{PbZr}_x\text{Ti}_{1-x}\text{O}_3$ ($x < 0.28$) whereas the first known ferroelectric materials such as Rochelle salt as well as $\text{PbZr}_x\text{Ti}_{1-x}\text{O}_3$ ($x > 0.28$) undergo a continuous phase transition. [\[24\]](#). However, it has been show that epitaxial films of PbTiO_3 and BaTiO_3 , which will be discussed in detailed at section 1.2, change the phase transition from discontinuous in bulk to continuous in thin films [\[25\]](#).

1.2 Heteroepitaxial oxide thin films

1.2.1 Epitaxial growth

The study of film growth has been widely investigated by the application of surface science methods to understand growth at the atomic level. The mechanism of this film growth usually involves deposition of a controlled amount of atoms onto a well-prepared crystalline substrate at a prescribed set of growth conditions. Vapor atoms and molecules that impinge onto the substrate surface are adsorbed to the surface, called adatoms. Small nuclei and individual clusters are formed from adatoms in the vapor phase on a substrate by a process of the nucleation and coalescence in the initial stage. Then, these islands merge and diffuse to the clusters or to a kink, and finally form a continuous film. The diffusion of an adatom on a flat surface is the most important kinetic and thermodynamic process in film growth. The growth mechanism is controlled by growth temperature and deposition rate, which together determine the surface diffusion length l_d , which is given by

$$l_d = \sqrt{D(T)\tau}, \quad (1.9)$$

where $D(T)$ is the temperature dependent surface diffusion coefficient and τ is the mean residence time of atoms at the surface [26].

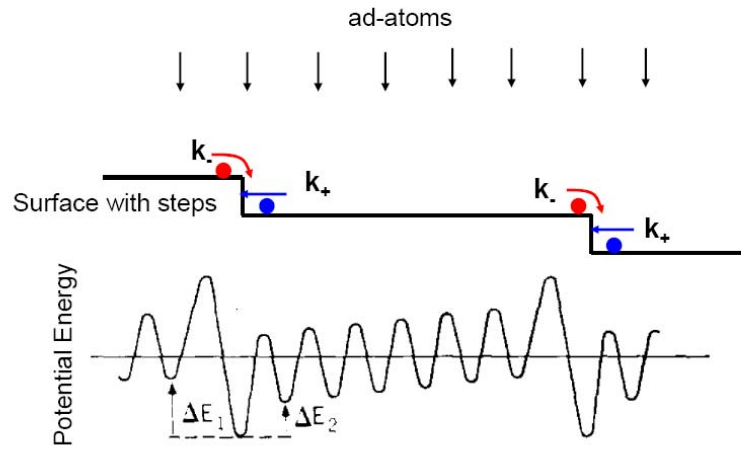
If surface diffusion of atoms happens only along and between layers, ideal thin films are deposited one atomic layer at a time. However, atoms traveling over the surface can tumble over ‘cliffs’ between layers [27]. These cliffs can be expressed as several

different energetic barriers, called Ehrlich-Schwoebel (ES) barriers [28] shown in Figure 1.5(a), where k_+ and k_- are the rate constants for capture of adsorbed atoms adjacent to the left and right step. As shown in Figure 1.5(b), the terrace-step-kink (TSK) model of a thin film surface displays different dimensional barriers which are related to growth mechanisms dependent on kinetic and thermodynamic adatoms. First, atoms experience the “corner-crossing” barrier, a one-dimensional version of the ES barrier. Second, atoms moving over steps that are one-atomic-layer high must cross the two-dimensional ES barrier. Finally there are three-dimensional ES barriers for atoms traveling over steps that are four or more atomic layers high, or over the edges between two facets [29]. This suggests that higher energetic adatoms can easily overcome those barriers following the step flow growth mode, which is usually observed with fully strained films at high temperature growth conditions.

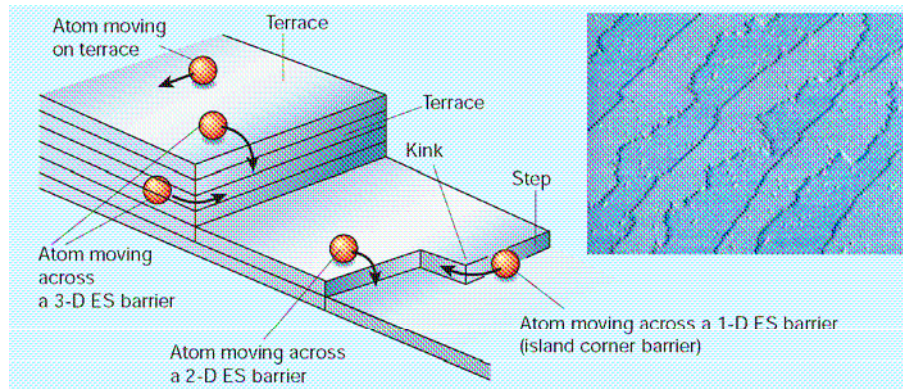
Strictly speaking, an epitaxial film is defined as fully strained grow on a single crystalline material on top of a substrate with the same crystal orientation as the intended layer. However, epitaxial films can be commonly identified by three different growth modes dependent on film relaxation: the layer-by-layer (Frank-van der Merwe) growth, the layer-then-3D island (Stranski-Krastanov) growth, and the 3D island (Volmer-Weber) growth [Figure 1.6] [30]. Lattice relaxation of films, which provokes different growth modes, is strongly related to the lattice mismatch f , which can be defined as

$$f = \frac{a_{film} - a_{substrate}}{a_{substrate}} \quad (1.10)$$

where a_{film} and $a_{substrate}$ are the lattice constants of the deposited material and the substrate, respectively. In general, almost perfectly lattice matched materials can grow in



(a)



(b)

Figure 1.5: Energy barrier of thin film surface. (a) Enrich-Schwoebel barrier. (b) The terrace-step-kink (TSK) model of a thin film surface. Figure (a) and (b) adapted from [27] and [28] respectively.

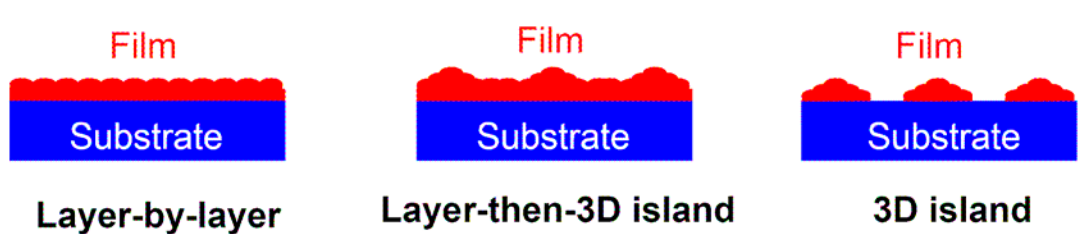


Figure 1.6: The main epitaxial growth modes.

a layer-by-layer mode [30]. For relatively large lattice mismatched materials, 3D island or layer-then-3D island are the energetically favored growth modes [30].

The different kinds of growth modes are also characterized by the total free energies of the system during growth. The energy determining the growing film has contribution from three terms, namely γ_f , γ_s , and γ_i , where γ_f is the surface free energy of the film, γ_s is the surface free energy of the substrate, and γ_i is the interfacial energy between the substrate and the film [31]. The relation between these contributions strongly influences the film growth since during the initial stages of growth which determines the growth mode one can neglect the volume energy of the film. For instance, 3D island growth occurs when the atoms are more strongly bound to each other than to the substrate, i.e.

$$\gamma_f + \gamma_i > \gamma_s, \quad (1.11)$$

so that it is energetically favored to leave some substrate exposed. In layer-by-layer growth, it is always energetically favorable to distribute the film uniformly over the surface when the bonds between the film atoms and the substrate atoms are stronger than

between the atoms of the film, i.e.

$$\gamma_f + \gamma_i < \gamma_s. \quad (1.12)$$

However, it is possible that over time, the lattice mismatch associated with the growth creates too much strain in the film and the energetic relationship switches to [Equation \(1.11\)](#), which corresponds to the layer-then-3D island growth mode.

The ability to control thin film growth has not only advanced our current understandings of two-dimensional physics, but also directly led to the observation of important physical phenomena such as giant electroresistance (GER) [\[32\]](#), ferroelectric tunneling junction (FTJ) [\[33,34\]](#), and ferroelectric thickness limit [\[3,4,5,6\]](#). Especially, epitaxial thin films provide unique and different physical properties compared to the bulk due to the strained effect on films by the substrate, which will be discussed in the next section.

1.2.2 Ferroelectric oxide thin films

In the perovskite ferroelectrics, it is well known that polarization as well as the ferroelectric phase transition due to temperature are strongly coupled to strain [\[35\]](#). This suggests that external stress is contributed strongly to ferroelectric transition temperature and polarization magnitude. Enormous strains can exist in epitaxial thin films, resulting from lattice mismatch of the film to the substrate. Experimentally, the properties of ferroelectricity in epitaxial thin films can be significantly different from the intrinsic properties of the corresponding unstrained bulk [\[11,36,37,38\]](#). Recent results report that

epitaxial compressive strain has been used to significantly enhance the ferroelectric properties of thin films compared to those of bulk materials [39,40].

In Figure 1.7, possible 2-dimensional domain patterns of tetragonal (100) thin films ($0 < T < 130$ °C) are depicted. In the case of free strained films, the mixed in-plane and out-of-plane polarizations coexist similar to bulk phase. However, when compressive strain is applied to thin films, only out-of-plane polarizations are expected, while the films under tensile strain show only in-plane polarizations.

Real epitaxial films have more complicated domain patterns, called 3-D intermediate domain, different from 3-D unstrained bulk domains in Figure 1.3 (the previous section). Table 1.1 shows a 3-D intermediate domain description of the six possible epitaxial BaTiO₃ phases considered by Pertsev *et al.* [25]. The two phase diagrams (Pertsev diagrams) for BaTiO₃ presented in terms of 3-D intermediate phases in Figure 1.8(a) and (b), are computed using two different sets of Landau-Devonshire parameters, used by Pertsev and coworkers in Refs. [25] and [41]. These results are based on an empirical thermodynamic potential with parameters fitted at temperatures in the vicinity of the bulk phase transitions. The Pertsev diagrams in Figure 1.8 show that imposed stresses can markedly affect the stability of the ferroelectric phase, as well as the ease with which polarization can be reoriented in some directions.

However, Vanderbilt and coworkers recently mapped out the structure of epitaxial BaTiO₃ using parameter-free total-energy methods based on density functional theory (DFT) [20,42]. The phase diagram in Figure 1.9(a) obtained from DFT calculations [42,43] differ from the Pertsev diagrams computed previously using a Landau-Devonshire theory where the parameters needed were obtained from

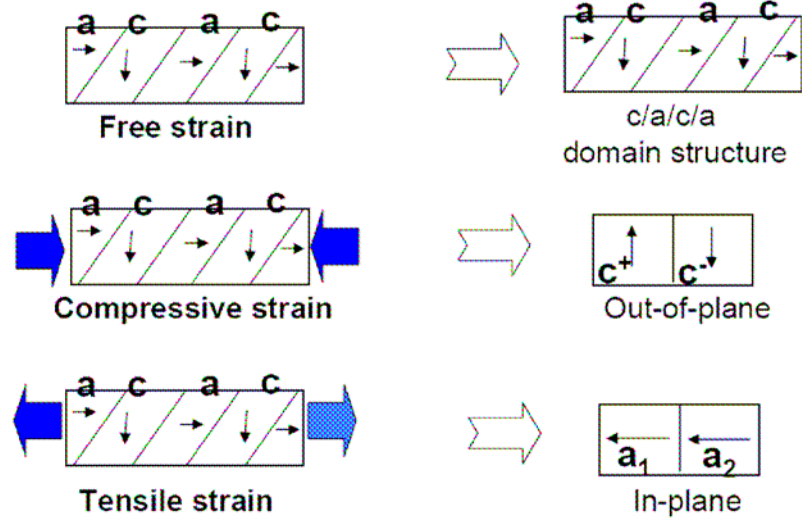


Figure 1.7: Possible domain structure of tetragonal (100) thin films at RT.

Table 1.1: Summary of possible epitaxial BaTiO₃ phases. Columns list, respectively: phase; space group; out-of-plane lattice vector; number of free internal displacement coordinates; and form of the polarization vector [42].

Phase	SG	\mathbf{a}_3	N_p	Polarization
p	$P4mmm$	$c\hat{z}$	0	0
c	$P4mm$	$c\hat{z}$	3	$P_z\hat{z}$
aa	$Amm2$	$c\hat{z}$	4	$P(\hat{x} + \hat{y})$
a	$Pmm2$	$c\hat{z}$	4	$P\hat{x}$
ac	Pm	$c_\alpha\hat{x} + c\hat{z}$	8	$P\hat{x} + P_z\hat{z}$
r	Cm	$c_\alpha(\hat{x} + \hat{y}) + c\hat{z}$	7	$P(\hat{x} + \hat{y}) + P_z\hat{z}$

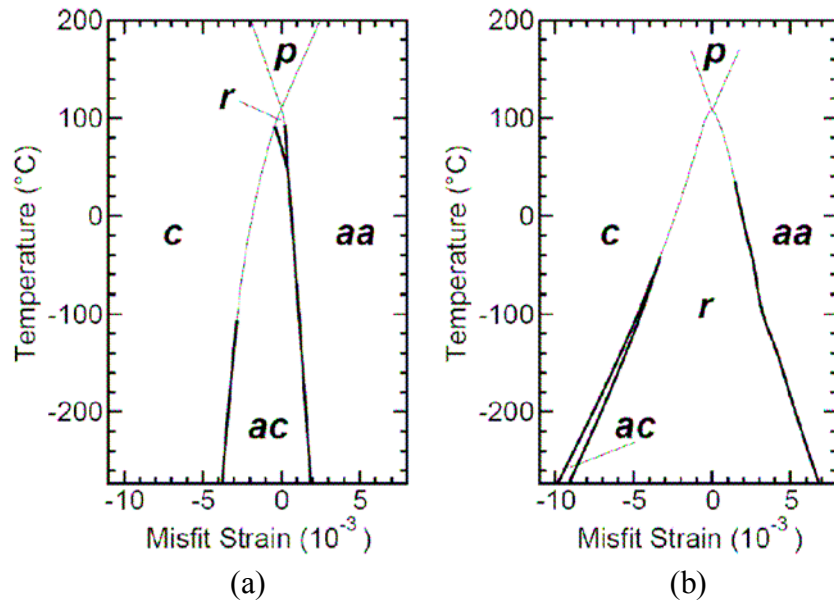


Figure 1.8: Phase diagram of epitaxial BaTiO₃ by semi-empirical method. (a) Using the parameters quoted in [25]. (b) Using the parameters quoted in [41]. The second- and first-order phase transitions are presented by thin and thick lines, respectively.

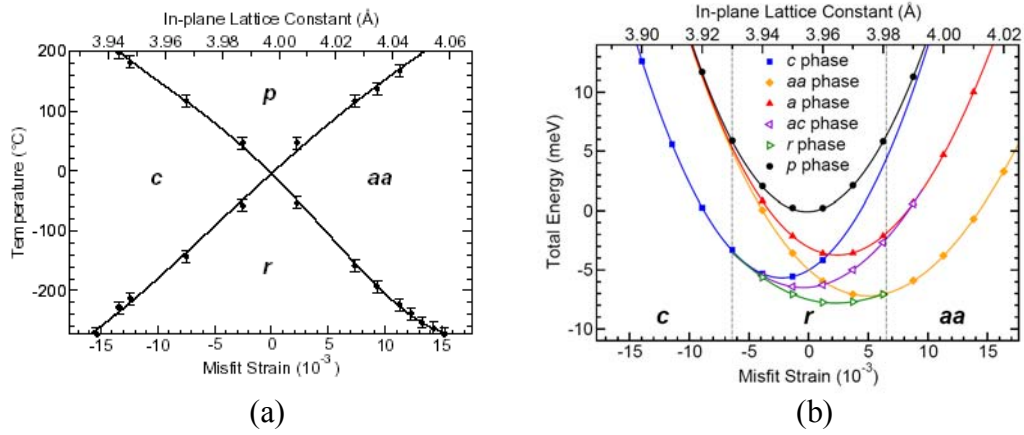


Figure 1.9: Diagram of epitaxial BaTiO₃ by DFT. (a) Phase diagram using the effective Hamiltonian [43]. (b) Energies of the possible epitaxial BaTiO₃ phases for different misfit strains, as obtained from the full ab initio calculation. The vertical lines denote the phase transition points given by the stability analysis. Figures adapted from [42].

experimental information about bulk BaTiO_3 at the phase transitions temperatures. According to DFT calculations shown in Figure 1.9(b), the energy of the ac phase is always higher than that of the r phase, which makes sense given that the r phase is an epitaxial distortion of the ground-state rhombohedral phase of bulk BaTiO_3 , while the ac phase is related to the higher energy bulk orthorhombic phase. Therefore, we can expect that the phase sequence at low temperatures is not $c \rightarrow ac \rightarrow aa$ as given in [42], but $c \rightarrow r \rightarrow aa$.

1.2.3 Metallic ruthenium oxide thin films

Considerable attention has been given to mixed strontium ruthenates with perovskite-based crystal structures, which form in alternating layers of Sr-O and Ru-O planes, both because of their interesting electronic and magnetic properties and because of the recent discovery of non-doped superconductivity in the layered ruthenate Sr_2RuO_4 [44]. The layered structure can take on many different arrangements as they form a metallic $\text{Sr}_{n+1}\text{Ru}_n\text{O}_{3n+1}$ Ruddlesden-Popper (RP) homologous series as shown in Figure 1.10(a) [45]. Figure 1.10(b) summarizes several different phase diagram and the complexity of $\text{Sr}_{n+1}\text{Ru}_n\text{O}_{3n+1}$ materials, all of which have metallic behavior, by exhibition of a wide array of magnetic, structural, and conductive properties [46]. The tetravalent ruthenium in the RP series has highly correlated electron system in $4d$ orbital. $4d$ ions generally have more extended d orbital than the corresponding $3d$ ions, and as a result $4d$ oxides tend to have greater overlap and strong hybridization between Ru $4d$ and O $2p$ orbital in the Ru-O plane [47], which leads to more interplay between structural degrees

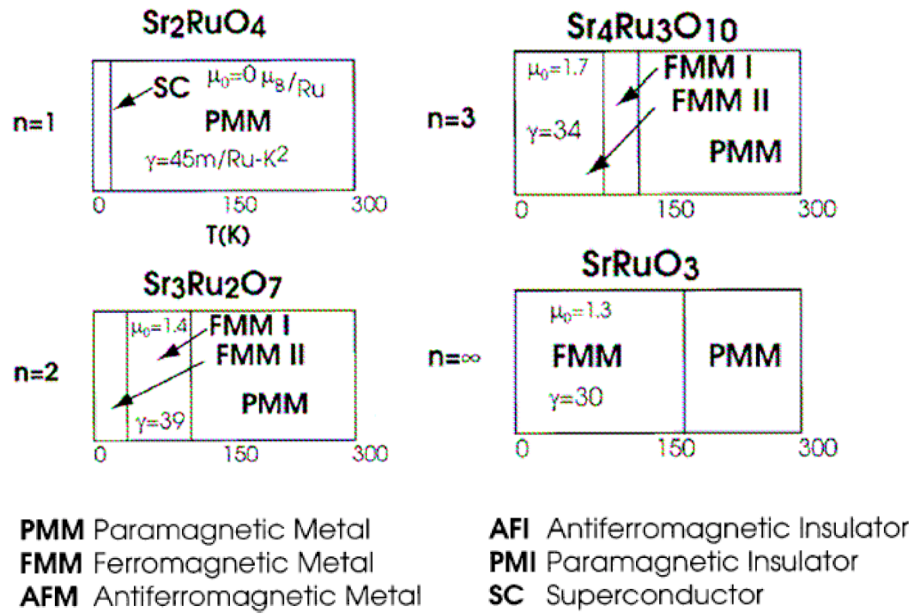
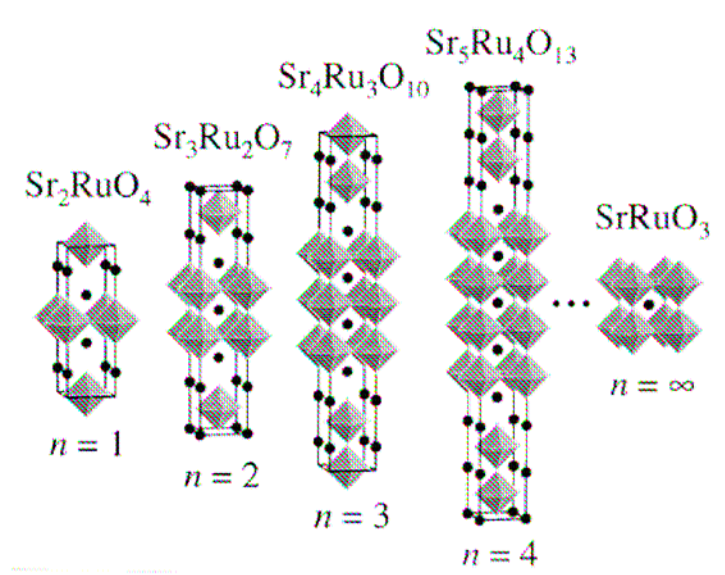


Figure 1.10: Ruddlesden-popper homologous series $\text{Sr}_{n+1}\text{Ru}_n\text{O}_{3n+1}$. (a) Crystal structure. (b) A general phase diagram for all members of $\text{Sr}_{n+1}\text{Ru}_n\text{O}_{3n+1}$ with $n = 1, 2, 3$, and ∞ . Figures adapted from [45,46].

of freedom and the magnetic and electronic properties. The extended $4d$ shell suggests that the intra-atomic Coulomb interaction U becomes weaker, relative to the $3d$'s, which would tend to drive the $4d$ TMO toward metallic behavior characterized by $U/W < 1$, where W is the conduction band width [46].

Recent surface studies of $\text{Sr}_{n+1}\text{Ru}_n\text{O}_{3n+1}$ series have been performed on Sr_2RuO_4 and $\text{Sr}_3\text{Ru}_2\text{O}_7$ [48,49,50,51]. However, the perovskite structure of SrRuO_3 precludes surface preparation through cleaving, which produces atomically flat surfaces for layered ruthenates such as Sr_2RuO_4 and $\text{Sr}_3\text{Ru}_2\text{O}_7$. For this reason, epitaxial SrRuO_3 thin films with surface studies by *in-situ* characterization are required to understand a variety of its interesting physical phenomena due to the closeness of the structural phase transition from cubic to orthorhombic phases, which in similar layered compounds triggers metal-insulator and magnetic phase transitions. Recent advances of laser MBE techniques have allowed the growth of high quality thin films of the $\text{Sr}_{n+1}\text{Ru}_n\text{O}_{3n+1}$ RP series, especially very successful in growth of SrRuO_3 films, which provides highly strained films with atomically flat surfaces [45,52]. It has also allowed the orientation of $\text{Sr}_{n+1}\text{Ru}_n\text{O}_{3n+1}$ thin film to be controlled by choosing appropriate substrates [45].

SrRuO_3 is the only known itinerant ferromagnetic perovskite, with a Curie temperature about 160 K and a moment $1.1 \mu_B$ at $T = 0$ K [53]. It is also well known that this material displays excellent chemical stability and good metallic conductivity [54,55,56]. Strain-free SrRuO_3 crystallizes in the orthorhombic distorted perovskite structure (space group $Pbnm$ symmetry) below 850 K, which arises from the tilting and rotating of the corner-sharing RuO_6 octahedra zig-zag chains [57]. Experimentally, strained SrRuO_3 films can grow epitaxially exhibiting two out-of-plane orientations

([001] and [110]) and two in-plane arrangements per orientation [58,59]. For the [001] oriented films, the in-plane lattice parameters (a and b) of the orthorhombic $Pbnm$ lattice are constrained to be equal in order to match the square lattice of the substrate, called $e-Pbnm[001]$ group symmetry where “e” indicates “epitaxial”. However, for the [110] oriented films, $SrRuO_3$ is subject to substantially different constraints compared with the [001] orientation, called $e-Pbnm[110]$ group symmetry. Two different orientations of the $SrRuO_3$ epitaxial films, $e-Pbnm[001]$ and $e-Pbnm[110]$, exhibit significant differences in their structural properties. The film with $e-Pbnm[001]$ symmetry remains orthorhombic at any reasonable value of the strain while the film with $e-Pbnm[110]$ symmetry has monoclinic symmetry unless there is no in-plane strain [57].

Finally, note that strontium ruthenate, $SrRuO_3$, is broadly used as a conductive electrode for perovskite oxide electronics due to good conductivity, chemical stability, and a relatively small lattice mismatch to $SrTiO_3$ substrates and many perovskite ferroelectrics. In this dissertation, the surface structure of $SrRuO_3$ thin films, serving as an electrode for electrical contact, will be investigated to understand the interface between conductive $SrRuO_3$ and ferroelectric $BaTiO_3$ films, which leads to reconstruction in ultra-thin $BaTiO_3$ films.

1.3 The ferroelectric thickness limit

Bulk ferroelectric perovskites experience spontaneous macroscopic polarization due to a lattice distortion which involves relative displacements between ions of opposite charge. This distortion is associated with a vanishing restoring force corresponding to

zero transverse optic mode frequency, and is called a “soft phonon mode” [35]. Although the ferroelectric soft mode is a collective motion of atoms in bulk materials, ferroelectricity, viewed as a collective phenomenon, is expected to be strongly influenced by surface and finite-size effects. In these pictures, the long-range electrostatic interaction along the polarization axis may not favor the parallel anisotropic alignment of dipoles anymore and probably does not dominate over the short-range repulsion between dipole-dipole interactions. There are theoretical predictions and experimental results that the length scale for ferroelectricity can be reduced down to a nanometer range and it will cease to exist under the critical thickness [3,5,6,7,8,9,10,11,12,13]. Recent developments, however, suggest that this is not a purely intrinsic behavior of ferroelectric materials, but a reflection of the mechanical and electrical boundary conditions resulting from the synthetic methods used [4]. As a result, the size dependence of the ferroelectricity remains an unresolved issue, in particular for the technologically important perovskites.

The existence of a critical thickness for ferroelectricity in perovskite thin films is usually explained by depolarizing fields \mathbf{E}_D produced by polarization charges σ_p accumulated on the two surfaces of the films:

$$\mathbf{E}_D = -4\pi \mathbf{P}, \quad \sigma_p = \mathbf{P} \cdot \hat{\mathbf{n}}, \quad (1.13)$$

where \mathbf{P} is the polarization generated in the ferroelectric thin film and $\hat{\mathbf{n}}$ is a unit vector normal to the surface that points out of the film. While the polarization and the accumulated surface charge are independent of the film thickness, the depolarizing field, \mathbf{E}_D , increases as the film becomes thinner. Thus a critical thickness may exist, where the depolarizing field is sufficiently large to suppress the polarization.

There are two mechanisms available to reduce the depolarizing field energy:

compensation by screen charges at the boundaries [8] or the formation of equilibrium 180° stripe domains with oppositely oriented polarization [3]. Here we focus on stabilization of the single-domain state in ferroelectric films by interfacial charge. If the ferroelectric film is placed between two electrodes M_1 and M_2 , the polarization charges are screened with the screen charges σ_s , which are given by

$$\sigma_s = \frac{dP}{\varepsilon(\delta_1 + \delta_2) + d}, \quad (1.14)$$

where d is the thickness of film, ε is the dielectric constant, and $\delta_{1,2}$ are the Thomas-Fermi screening lengths in the $M_{1,2}$ electrodes [32,60]. From Equation (1.14), the following cases can be distinguished:

- Complete screened, i.e., $\sigma_s = -\sigma_p$ (no depolarizing field E_D in the ferroelectric.) for “good” metals in which the screening length is small and for not too thin ferroelectrics, such as $\varepsilon(\delta_1 + \delta_2)/d \ll 1$.
- Completely unscreened, i.e., $\sigma_s = 0$ (the depolarization field increases to saturation at $E = -P/\varepsilon$ [61]) in the opposite limit, $\varepsilon(\delta_1 + \delta_2)/d \gg 1$.

However, when the thickness of the ferroelectric film is sufficiently reduced, such as $\varepsilon(\delta_1 + \delta_2)/d \gg 1$, the screening becomes incomplete and the depolarizing field that results from an incomplete compensation of the polarization charges becomes significant. Batra and Silverman showed that the incomplete compensation of the polarization charges changes the stability of the ferroelectric phase [62,63,64]. The depolarization field that results from an incomplete compensation of the polarization charges becomes significant when the thickness of the ferroelectric film is reduced. It is then energetically difficult for the sample to sustain its uniform polarization. At some critical thickness the electrostatic energy associated with the depolarizing fields overcomes the energy gained

due to ferroelectric ordering [8]. At this thickness the ferroelectric state becomes unstable.

The predicted minimum thickness for ferroelectricity has decreased significantly over time [Figure 1.11]. Early works from Batra and Silverman predicted a minimum thickness of 400 nm [64]. Recent first principles calculations assuming short circuit boundary conditions suggest a critical thickness of 2.4 nm for $\text{SrRuO}_3/\text{BaTiO}_3/\text{SrRuO}_3$, 1.2 nm for stress-free PbTiO_3 , and 1 nm for $\text{Pt}/\text{KNbO}_3/\text{Pt}$, physically resulting from the imperfect screening of the depolarization field [8,9,12], while the predictions of some groups imply that no thickness limit is imposed on practical devices by an intrinsic ferroelectric size effects [4]. This substantial change of the predictions over time is mainly due to a better understanding of the influence of electrical and mechanical boundary conditions. Experimentally, in the last 10 years a lot of work has been done and the outcome of the improved deposition and analytical techniques has been quite considerable. However, most ultra-thin films show large leakage currents, which makes direct electrical measurements difficult, and therefore methods other than the traditional P-E hysteresis loop have been reported to characterize the stability of the ferroelectric phase state down to 1.2 nm for PbTiO_3 and 4 nm for $\text{Pb}(\text{Zr}_{0.2}\text{Ti}_{0.8})\text{O}_3$ [3,5].

1.4 Ferroelectric tunneling junction

Since tunneling current was predicted by Wilson, Frenkel, and Joffe 70 years ago, the tunnel effect has played a significant role during the development of quantum mechanics and its applications. This physical phenomenon has recently been described in

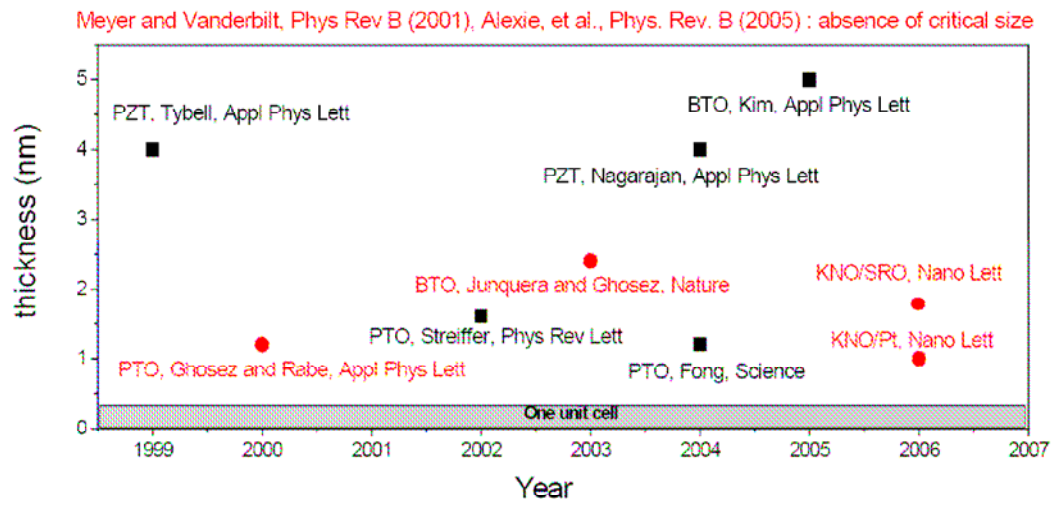


Figure 1.11: History of ferroelectric thickness limit.

etal-ferroelectric-metal (MFM) devices, termed a “ferroelectric tunnel junction (FTJ)”, with ultra-thin (< 6 nm thick) barriers and the polarization state of a barrier [32,33,34,65,66]. Conventionally, a ferroelectric is treated as an insulator, which has very small leakage current due to free carriers. If the thickness of a ferroelectric layer is small enough, the dominant transport mechanism may be even the direct quantum mechanical electron tunneling rather than the leakage current phenomena across the whole barrier (local measurements of tunneling current can also reduce the possibility of the large leakage current due to film defects).

Recent theoretical studies on the FTJ suggest that the polarization reversal in the ferroelectric barrier produces a change in the potential profile across the junction and leads to the resistance switching by the influence of converse piezoelectric effect and depolarizing field effect [32,33]. The effect of a ferroelectric on the tunneling current is complex and not well understood. To first order, a switch in the direction of ferroelectric polarization changes to location (depth) of the tunneling barrier, but not its height. Since the effective barrier height is not changed directly, this has no influence on the tunneling rate. Indirect effects thought to be important include (1) barrier width modification by the converse piezoelectric effect, (2) changes in the electron mass by structural changes in the ferroelectric, and (3) the depolarizing electric field of the screening electrons in the conducting elements. None of these theories has been directly tested. The purpose of this work is to investigate the electron transport by tunneling through FTJs with ultra-thin barriers in order to understand the physics and its dependence on the polarization state of the barrier.

In Ref. [32], Zhuravlev, et al., calculated the changes in the tunneling

conductance associated with the polarization switching using a model (M_1 -FE- M_2) which takes into account screening of polarization charges in metallic electrodes (M_1 and M_2) and direct quantum tunneling across a ferroelectric barrier. The different depolarizing fields due to the finite electron screening length in metals modify the potential barrier in a M_1 -FE- M_2 junction for electron tunneling. However, for symmetric FTJs ($M_1 = M_2$), the potential profile changes neither the mean barrier height nor the average slope of the barrier even if $M_1 = M_2 =$ bad and good metals. Therefore, according to this work, the depolarizing field cannot change the tunneling conductance and induce significant resistive switching. In the case of asymmetric FTJs, the potential profile for different electrodes changes the mean barrier and tunneling conductance. Especially, polarization switching with the same electrodes (but $M_1 \neq M_2$) can also provide a different average potential barrier height, which means the changes in the tunneling conductance depend on polarization status.

In [Ref. \[33\]](#), the current-voltage characteristics of FTJs are analyzed under the assumption that the direct electron tunneling represents the dominant conduction mechanism. In this ref., Kohlstedt *et al.* describe the influence of a converse piezoelectric effect inherent in ferroelectric materials and the influence of the depolarization field arising due to imperfect screening of polarization charges by electrons in metal electrodes with respect to symmetric and asymmetric FTJs. When a potential difference, V , between the electrodes is applied, the out-of-plane strain, S_3 , can vary due to the converse piezoelectric effect. After the polarization reversal, the effective longitudinal piezoelectric coefficient d_{33}^* ($\Delta S_3 \sim d_{33}^*$) changes its sign, which make a jump of current or conductance at the critical voltage ($J(V) = C_1V + C_2(d_{33}^*)V^2 + C_3(d_{33}^{*2})V^3 + \dots$).

These phenomena can happen to both symmetric and asymmetric FTJs. They also mentioned the depolarization field effect, which changes the hysteretic I-V curve drastically in asymmetric FTJs. An asymmetric curve [Figure 1.12(a)] can be obtained due to the converse piezoelectric and depolarizing field effects, whereas a symmetric curve [Figure 1.12(b)] can be obtained only by the converse piezoelectric effect.

The idea and very preliminary study of a FTJ was presented already in 1971 by Esaki. However, the realization of this idea is a task with many obstacles, because it requires the fabrication of ultrathin films retaining pronounced ferroelectric properties at a thickness of only a few unit cells. Recent experimental work shows ferroelectricity was observed down to a nanometer scale in perovskite ferroelectric oxides shown in the previous section. We study FTJ with BaTiO_3 films (< 6 nm thick) by nanoscale measurement such as *in-situ* scanning tunneling spectroscopy (STS) to avoid the leakage current due to film defects and to tunnel through a homogenous film.

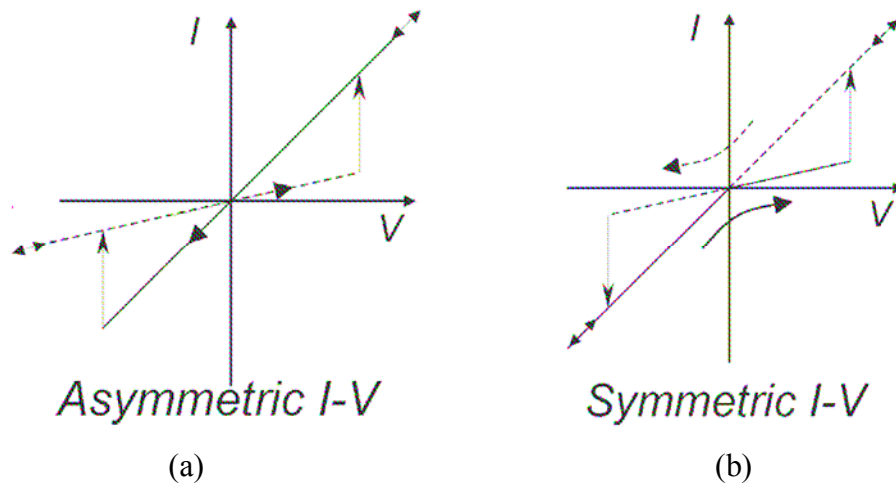


Figure 1.12: The current-voltage characteristics of FTJ. Figures adapted from [33].

Chapter 2

Characterization Techniques

2.1 Laser molecular beam epitaxy

Depending on the characteristics of materials, a number of techniques are now available to produce high quality of single and multilayered thin films. These include thermal evaporation, sputter deposition, molecular beam epitaxy, chemical vapor deposition, and pulsed laser deposition (PLD). Especially, physical vapor deposition techniques such as plasma and ion beam sputter deposition and pulsed laser ablated deposition are extensively used for synthesizing thin films [67]. Compared to other growth techniques conducted in ultrahigh vacuum (UHV) environment, PLD is uniquely able to obtain high quality and highly oxidized thin films and multilayer of complex materials [31]. Complex materials such as transition metal oxides have a perovskite-based crystal structure similar to many ferroelectric materials and can be successfully deposited as epitaxial films in high oxygen pressure by PLD.

Laser molecular beam epitaxy (laser MBE) is essentially a sub-category of PLD in which a pulsed laser rapidly evaporates a target material forming a thin film that retains target composition. Ideal for nanoscale thin films, the combination of PLD and *in-situ* high pressure reflection high energy electron diffraction (RHEED) provides precise control of film growth at the monolayer level (MBE-like monolayer control of thin film growth), called “laser MBE”. This laser MBE can operate to grow highly oxidized thin

films in high oxygen pressure up to ~ 500 mTorr using high pressure RHEED, which will be explained in [Section 2.4.1](#).

A sketch of our laser MBE system is schematically shown in [Figure 2.1\(top\)](#). This system consists of a KrF excimer laser ($\lambda = 248\text{nm}$) and a growth chamber, which is connected to the complex UHV system for *in-situ* characterization [[Figure 2.1\(bottom\)](#)]. A pulsed laser beam from an excimer laser, external to the growth chamber, is focused onto the rotating target through an optical system of lenses. The lenses and windows passed through by the laser beam are chosen to minimize any absorption of intensity and to maximize the attainable laser power on the target. A pyrolytic Boron Nitride (PBN) heater, which is covered with Hastelloy (a stainless steel alloy) housing for good conservation of heat, is used to heat the substrate up to ~ 850 °C in high oxygen pressure (~ 500 mTorr). For *in-situ* characterization, the growth system needs the specially designed Hastelloy sample holder, which can be transferred to the characterization chambers. When the laser beam interacts with the ceramic target, a plume is formed from a target so that the material of target is deposited on the heated substrate. A plume in [Figure 2.1\(top\)](#) consists of a plasma containing energetic neutral atoms, ions, and molecules.

To get high quality thin films, several the adjustable experimental parameters play an important role in laser MBE growth. These parameters include target material, substrate temperature, oxygen pressure, target-substrate distance, laser energy and repetition rate, and film-substrate lattice mismatch. Note that all parameters are not independent, which means there is no universal correct value of parameters, but every parameter has to be considered for the best growth conditions of a particular material.

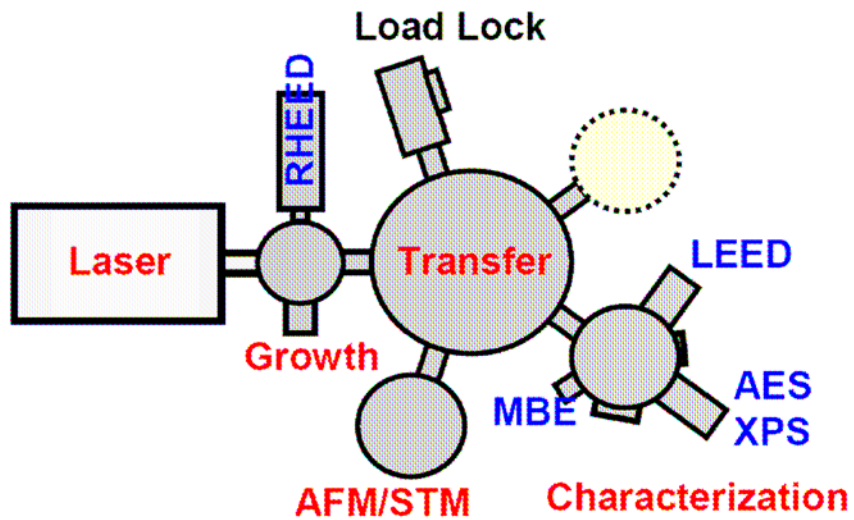
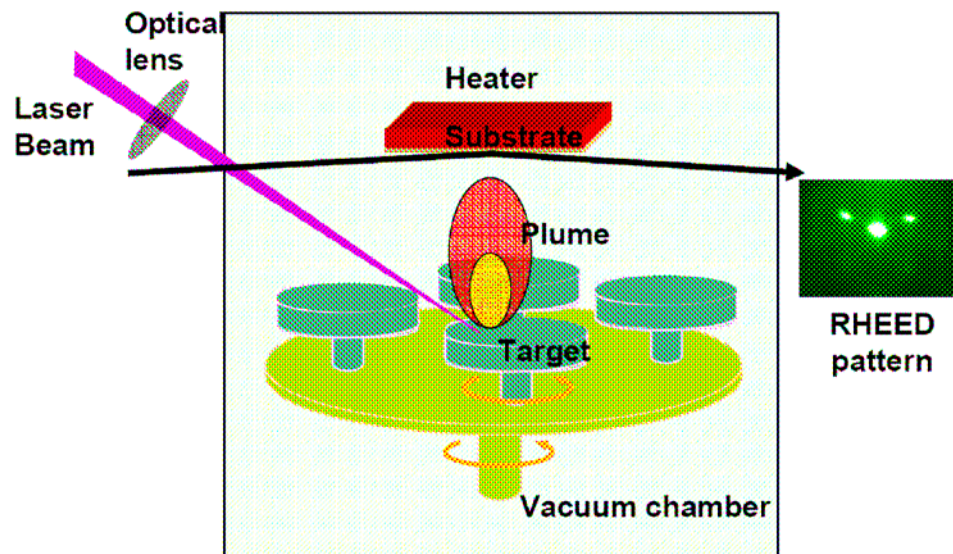


Figure 2.1: Synthesis and characterization. Schematic of Laser Molecular Beam Epitaxy (top). The complex UHV system for *in-situ* characterization (bottom).

For example, relatively high oxygen pressure conditions may require a reduction in the target-substrate distance due to the change of a plume size. Too many adjustable parameters suggest that laser MBE growth is not easy to get high quality of films. Therefore, it is very important to understand the parameters which influence the growth in order to control them and to determine the film properties. In the present study, laser MBE parameters are optimized for each material under investigation.

2.2 X-ray diffraction

The diffraction of x-rays by the closely spaced lattice of atoms in a crystal produces a pattern, which can be recorded and analyzed to identify crystalline and structural properties. X-ray diffraction is now a standard tool for materials science with many available references [68,69]. The $(\theta-2\theta, \varphi, \psi, \omega)$ x-ray diffraction (XRD) patterns of thin films were measured using the four-circle x-ray diffractometry. Figure 2.2 shows a schematic of the four-circle x-ray geometry. The detector ($\theta-2\theta$) and the sample (φ, ψ, ω) can be rotated independently to measure the patterns and provide specific information with respect to each angle scan. The $\theta-2\theta$ and ω circles enable probing of the crystalline planes in a film parallel to the substrate surface. The φ and ψ circles allow probing of reflections and planes that are not parallel to the surface of the substrate.

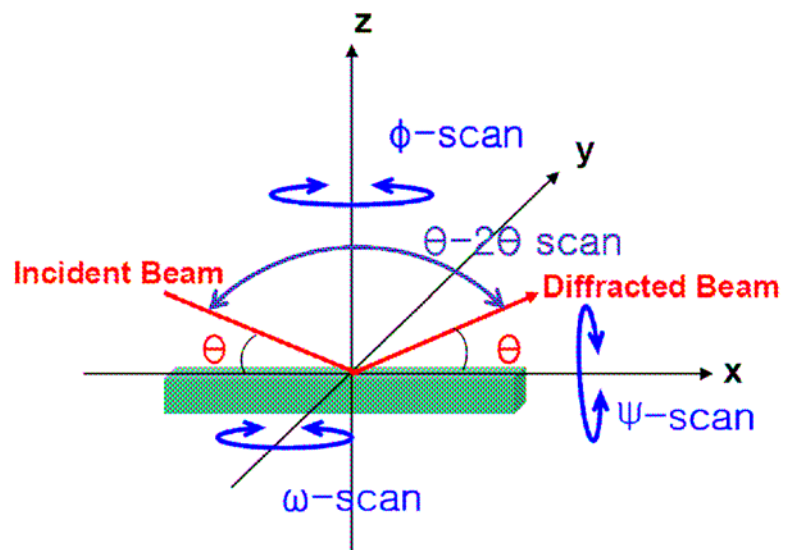


Figure 2.2: Schematic of four-circle x-ray diffractometry

2.2.1 θ -2 θ scan

The θ -2 θ scan provides information about the crystalline orientation of the crystal and the out-of-plane lattice parameters. A beam of x-rays, with wavelength λ , that reaches the crystal surface at angle θ is elastically scattered by electrons [Figure 2.3(a)]. The sample consists of rows of crystal planes that are separated by d , which is a distance between the atomic layers in a crystal. The constructive interference of the scattered probe results in sharp diffraction peaks determined by the celebrated Bragg's law

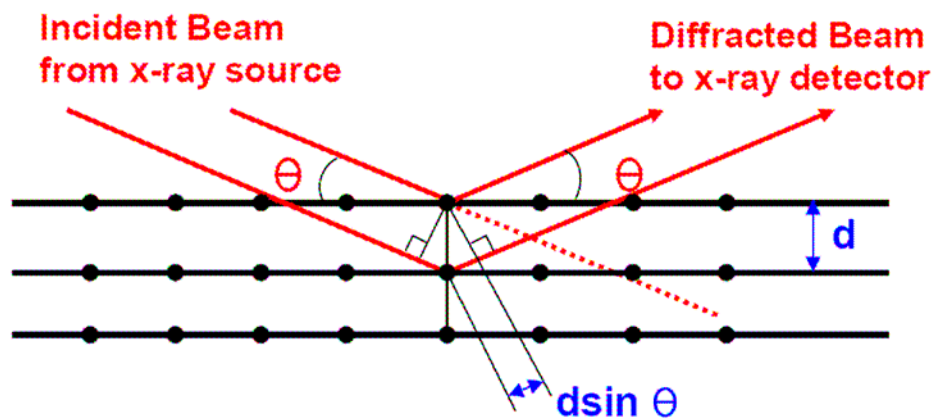
$$n\lambda = 2d \sin \theta \quad (2.1)$$

where n is integer.

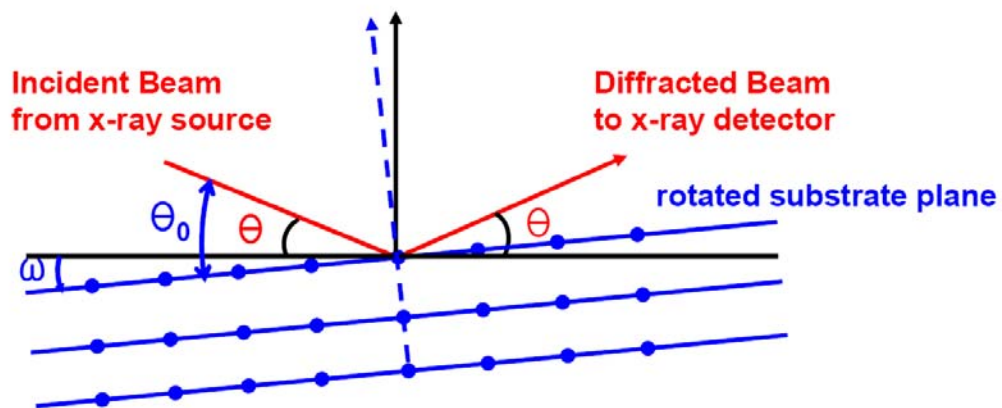
2.2.2 ω -scan

The ω -scan, known as a rocking curve measurement, gives the information on the texture and the crystalline quality of the films. For a (00 l) oriented thin film, the ω -scan of a Bragg reflection, is performed to determine whether atomic layers are perfectly aligned the each other, i.e. the spread and tilt of the film. To measure a ω -scan, the peak from the θ -2 θ scan diffractogram should be chosen and then the detector remains at a fixed position (black lines in Figure 2.3(b)) while the rocking curve is measured by rotating (or rocking) the sample around the ω circle. The ω -scan is defined as θ_0 - θ shown as in Figure 2.3(b). If the sample is a single crystal, the intensity of the reflected beam

becomes zero because θ_0 does not satisfy the Bragg condition. On the other hand, if the



(a)



(b)

Figure 2.3: Probing of the crystalline planes parallel to the surface. (a) Bragg diffraction of x-ray and (b) Schematic describing the ω -scan (Rocking curve).

sample is composed by atomic layers that are not perfectly aligned each other, a finite intensity is measured. Therefore, the full width at half maximum (FWHM) in ω provides a measure of the spread in the orientation of the atomic layers aligned the each other.

2.3 Electron diffraction

Electron diffraction is in the arsenal of surface science techniques to investigate the structure and the symmetry of surfaces. These techniques are based on the wave nature of electrons and their strong interaction with matter. They provide the chance to analysis a surface in two ways: low kinetic energy electrons (typically 20 eV – 500 eV), and high energy electrons (> 1 keV). The first corresponds to the low energy electron diffraction (LEED) technique with a mean free path (or average distance between two inelastic scatterings) lower than 1 nm, and the second is reflection high energy electron diffraction (RHEED) with the higher value of the mean free path. However, this higher value of the mean free path requires that RHEED should work in grazing incidence to have only access to the structure of the surface atomic planes.

2.3.1 Reflective high energy electron diffraction

RHEED is a surface sensitive technique which allows us to monitor epitaxial growth of thin films in real time and qualitatively measure properties of the surface of a sample during the growth process. In RHEED, the incident electron beam strikes the

crystalline surface under bombardment with high energy electrons near grazing incidence typically $< \sim 3^\circ$) and is reflected onto a phosphorescent screen. The diffraction pattern provides very surface sensitive information (1nm depth) on the atomic arrangement of the top layers of a solid.

The grazing incidence angle ensures surface specificity despite the high energy of the incident electrons. The intensity of the reflected beam is proportional to the surface roughness [Figure 2.4]. If a surface is atomically flat, a high reflected intensity and sharp RHEED patterns are seen. However, rough surfaces do not reflect well and the intensity is lower. In this case, the RHEED pattern is more diffuse. This behavior can be applied for monitoring method of the thin film growth, so called “RHEED oscillation”, during thin film deposition. In Figure 2.5, the origin of the RHEED intensity oscillations is explained while the layer-by-layer growth mode proceeds [70]. If the initial surface is perfectly flat, the specular spot has relatively high intensity of reflectivity. When deposition starts to evaporate materials onto a surface, the incident electron beam becomes partially scattered by the island steps of the forming monolayer, thus reducing the reflected intensity of the specular spot. Minimum intensity of reflectivity is observed at half ML coverage, which indicates that scattering of beams becomes maximized. With keeping the growth procedure, the new monolayer completes and the surface flattens again by coalescence of the islands, and the reflected intensity recovers its maximum value. Note that time interval of one RHEED oscillation is almost constant except for one of the first oscillation.

In the case of layer-by-layer growth mode, the films thickness (ML) can be easily estimated by measuring the period (T) of RHEED oscillation and total growth time

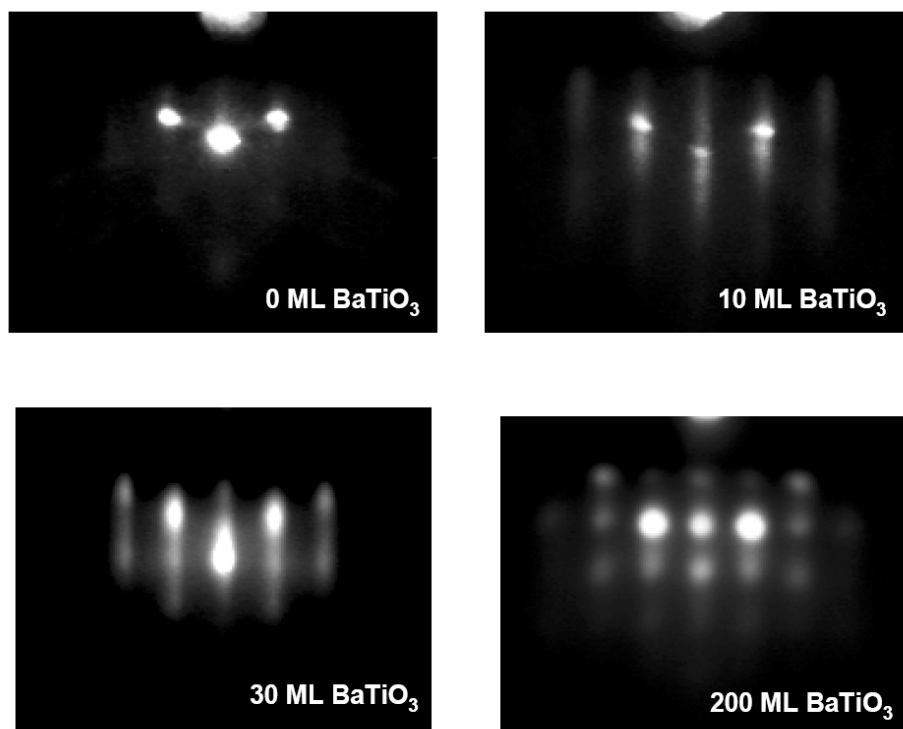


Figure 2.4: RHEED patterns dependent on the surface roughness of BaTiO₃ films. The films were grown by laser MBE.

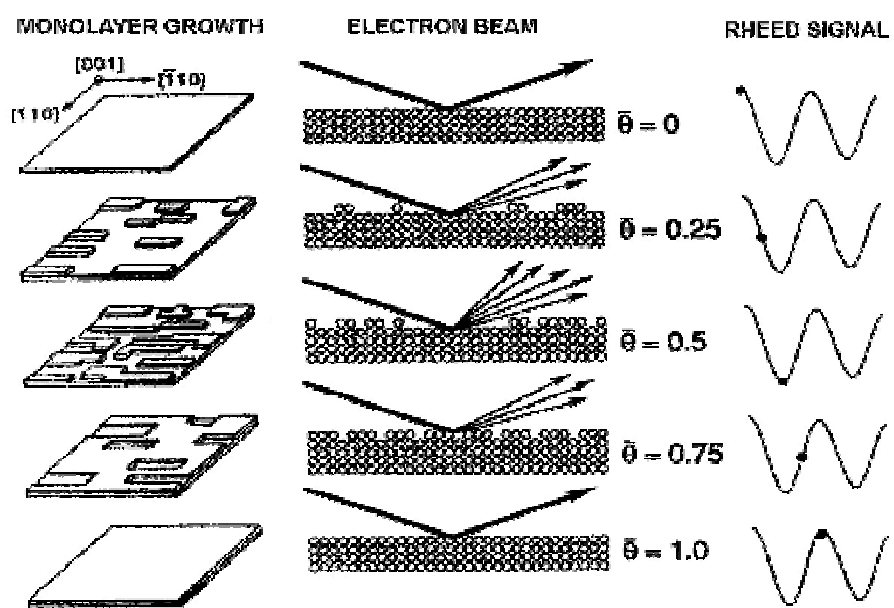


Figure 2.5: Mechanisms of RHEED oscillations during growth of a monolayer. Figures adapted from [70].

(t) and given as

$$d(ML) = \frac{t}{T} . \quad (2.2)$$

However, this RHEED oscillation is observed in the case of only layer-by-layer growth mode. This RHEED oscillation cannot appear in the other growth modes such as step flow growth or 3D island growth. In this case, the thickness of films can be measured by other kind of techniques (XRD, transmission electron microscopy *et al.*).

High-pressure RHEED

In the thin film growth of metallic or semiconducting materials under UHV conditions, normal RHEED procedures apply. However, the high oxygen pressure required for oxide growth prevents the use of normal RHEED systems due to the small mean free path (a few cm) of electrons in the 10-200 mTorr regime commonly used. For this reason, a modified RHEED system is required for high-pressure growth. Usually, the electron gun filament in a RHEED system must be operated in high vacuum (1.5×10^{-5} Torr) in order to increase its lifetime. The use of a double differential pumping system makes it possible to minimize the path electrons travel through the high pressure deposition chamber, while still keeping the electron gun under high vacuum. Our current high-pressure RHEED system allows the deposition pressure up to 500 mTorr.

2.3.2 Low energy electron diffraction

Low energy electron diffraction (LEED) is the oldest and the most successful surface science technique and is used to study the structure of crystalline surfaces. From the first LEED experiment by Davison and Germer in 1927 [71,72] to now, many different techniques and extremely sophisticated applications have been developed. In these days, LEED I-V analysis has been developed with an accuracy of less than a few hundreds Å for the structure analysis of atomic positions in the surface unit cell. Note that there are two reasons why LEED is surface sensitive technique as follows:

- 1) The mean free path for low energy electrons in solids is short.
- 2) The electron de Broglie wavelength fits very well the typical distances in crystals.

2.3.2.1 Diffraction pattern formation

To understand how a LEED pattern is formed we can start with the overview of the construction (or destruction) interference of the scattered waves emanating from the crystal surface [73]. In X-ray diffraction, the diffraction conditions for a three dimensional lattice are given by the “Laue condition”

$$\Delta \vec{k} = h\vec{g}_1 + k\vec{g}_2 + l\vec{g}_3 = \vec{g}, \quad \vec{g}_i = 2\pi \frac{\vec{a}_j \times \vec{a}_k}{\vec{a}_i \cdot (\vec{a}_j \times \vec{a}_k)} \quad (2.3)$$

where \vec{g} is a reciprocal lattice vector, \vec{g}_i ($i = 1,2,3$) are primitive vectors in reciprocal

lattice, and \vec{a}_i are primitive vectors of the crystal lattice [Figure 2.6(a)]. This condition can be visualized by a simple geometric construction (Ewald sphere) using the fact that intensities can appear only in directions given by $\Delta\vec{k} = \vec{k}' - \vec{k} = \vec{g}$ [Figure 2.6(b)]. However, ideal two-dimensionality has only a single atomic layer, which means that the real-space periodicity along the plane normal is infinite, i.e.,

$$\vec{a}_3 \rightarrow \infty \quad \Rightarrow \quad \vec{g}_3 = 2\pi \frac{\vec{a}_2 \times \vec{a}_1}{\vec{a}_3 \cdot (\vec{a}_2 \times \vec{a}_1)} \rightarrow 0. \quad (2.4)$$

This gives 2-D rectangular real space lattice corresponding to the reciprocal lattice rods with two reciprocal lattice vectors [Figure 2.6(c)]:

$$\vec{g}_1 = \frac{2\pi}{\vec{a}_1} \vec{e}_1, \quad \vec{g}_2 = \frac{2\pi}{\vec{a}_2} \vec{e}_2. \quad (2.5)$$

The diffraction conditions for this two dimensional reciprocal lattice are given by the following Laue condition associated with the momentum transfer parallel to the surface:

$$\Delta\vec{k}_{\parallel} = h\vec{g}_1 + k\vec{g}_2 = \vec{g}_{\parallel}. \quad (2.6)$$

This momentum (\vec{k}_{\parallel}) is conserved and satisfied with planar symmetries existing along the surface. Therefore, the reciprocal lattice cuts the surface of the Ewald sphere perpendicular to the rods, which forms a circle, and the wave vectors can be projected on to it [Figure 2.6(d)]. This shows how to form LEED pattern.

When considering the diffraction from the real surface, the semi-three dimensional nature should be taken into account instead of a perfect 2D lattice in which the integral intensity of spots is not modified but the intensity distribution is influenced in reciprocal space. Since the incident electron beam penetrates into the crystal even though only within a few atomic layer and feel the third Laue condition, our reciprocal

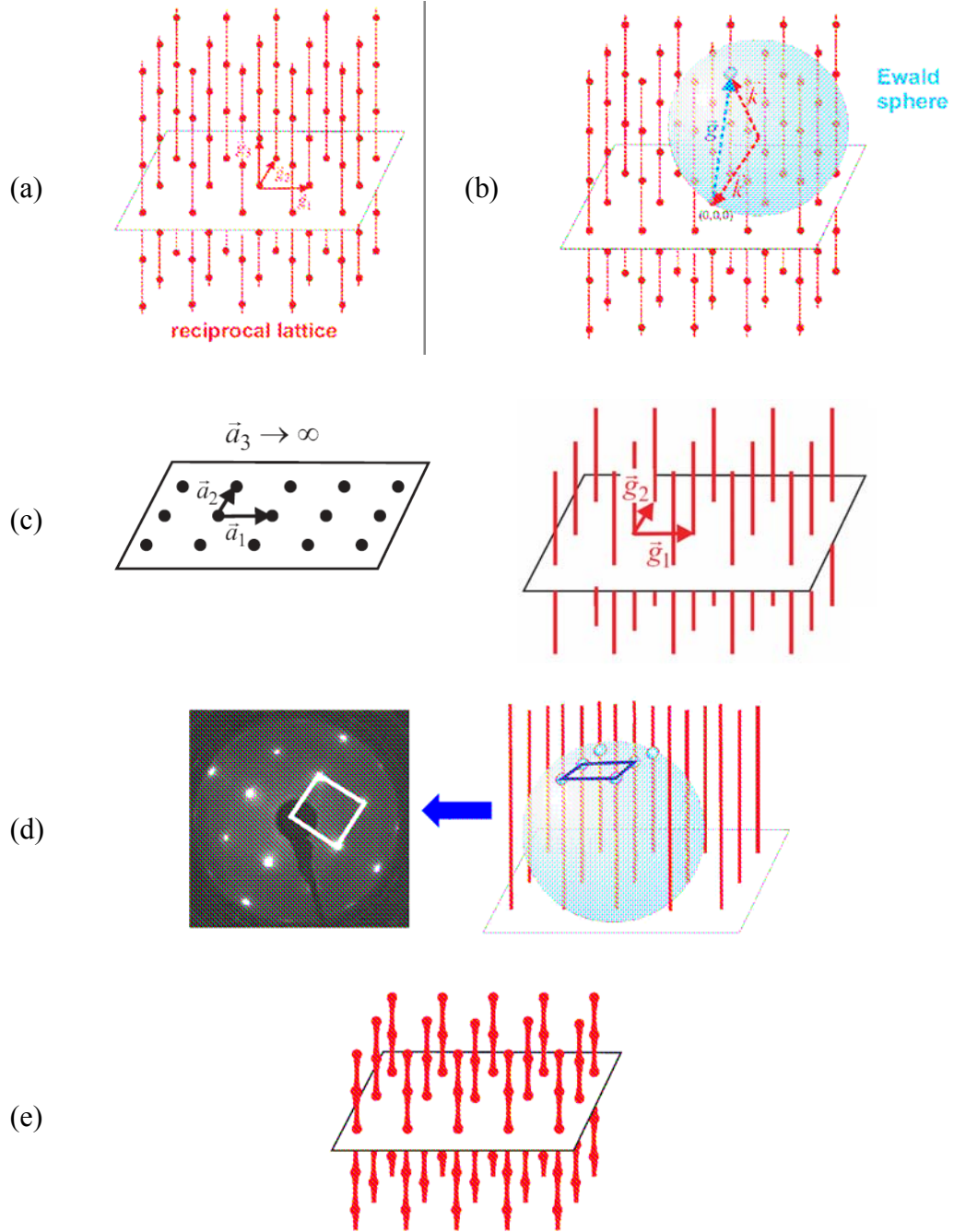


Figure 2.6: Principles of 2 dimensional diffraction pattern formations. (a) 3-D reciprocal lattice. (b) 3-D Ewald construction through Bragg spots. (c) 2-D reciprocal space. (d) 3-D Ewald construction through Bragg rods and 2-D projection of Ewald sphere parallel to Bragg rods. (e) Modified reciprocal lattice by surface reality. Figures adapted from [73].

lattice rods are not infinite continuously. Instead of infinite rods, reciprocal lattice “seen” by LEED is a mixture between continuous rods and discrete points [Figure 2.6(e)]. This leads to very strong intensity variations in the LEED spots as a function of energy by measurement of intensity vs. accelerating voltage of the electrons. By the measurement and analysis of intensities, we can probe crystallographic information regarding the geometrical atomic structure near the surface region of the crystal, which will be discussed in Section 2.3.2.2 in detail.

Now, let's apply these concepts to the real LEED experiment [74]. A typical experimental set-up is shown in Figure 2.7(a). The LEED experiment uses a beam of electrons of a well-defined low energy (typically in the range 20 - 500 eV) incident normally on the surface of the sample. The sample itself must be a single crystal with a well-ordered surface structure in order to generate a back-scattered electron diffraction pattern. Equation 2.6 for the high intensities of the patterns requires the relation between the magnitude $|\vec{k}'|$ of the outgoing electrons and the emission angle θ_{hk} such as

$$\theta_{hk} = \sin^{-1} \frac{|\vec{k}'_{\parallel}|}{|\vec{k}'|} \quad \text{and} \quad \vec{k}'_{\parallel} - \vec{k}_{\parallel} = \vec{k}'_{\parallel} = h\vec{g}_1 + k\vec{g}_2 \quad (2.7)$$

where $\vec{k}_{\parallel} = 0$ due to the normal incident beam. Therefore, shown as Figure 2.7(b), the position of the intensity maxima on the screen in LEED apparatus is given by

$$d_{hk} = R \sin \theta_{hk} = \frac{R}{|\vec{k}'|} |h\vec{g}_1 + k\vec{g}_2| = R \sqrt{\frac{\hbar^2}{2mE}} |h\vec{g}_1 + k\vec{g}_2|. \quad (2.8)$$

From Equation 2.7, we can see that the spots move closer to the center of the screen (reduce d_{hk}) by increasing the energy E. New spots also move in on the sides of the

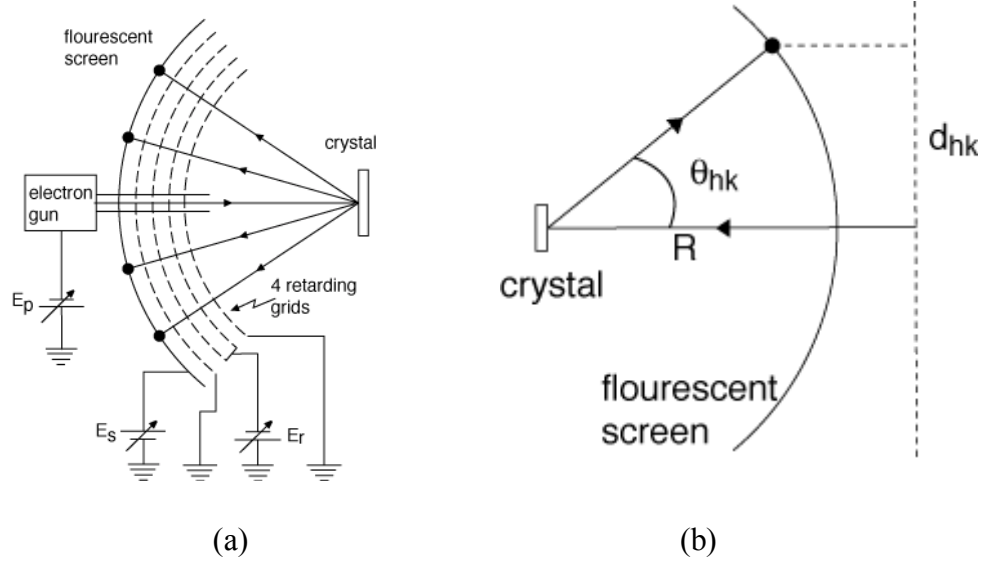


Figure 2.7: Schematic of LEED set-up. (a) LEED system and (b) linear imaging of the reciprocal lattice by LEED. Figures adapted from [74].

screen which have not been visible before. Note that the different d_{hk} values are given from the different set of (h,k) , which corresponds to each spots on LEED screen. Especially, if a reconstruction or an overlayer with double periodicity is present, then we will see such a $(1/2,0)$ spot and so on in the real measurement, which will be discuss in the next.

2.3.2.2 Surface Structure determination by LEED

Based on the Schrödinger equation for the scattering of electrons by a surface, the scattering amplitude after the kinematic approximation (1st Born approximation by single scattering approach) can be described as a sum of electron wave function scattered by all surface atoms with potential $V = \sum_i \sum_j \delta[r - (\vec{R}_j + \vec{r}_i)] \cdot V_i$ at position $\vec{r}_{i,j} = \vec{R}_j + \vec{r}_i$

shown in Figure 2.8,

$$f(\vec{k}) = -\frac{1}{2\pi} \sum_j e^{i\Delta\vec{k} \cdot \vec{R}_j} \sum_i V_i e^{i\Delta\vec{k} \cdot \vec{r}_i} . \quad (2.9)$$

If we define $G \equiv \sum_j e^{i\Delta\vec{k} \cdot \vec{R}_j}$ and $F \equiv \sum_i V_i e^{i\Delta\vec{k} \cdot \vec{r}_i}$, then the intensity splits up

$$\frac{I}{I_0} \sim |G|^2 \cdot |F|^2 \quad (2.10)$$

into the lattice factor $|G|^2$, which influences the only intensity distribution in reciprocal space and the structure factor $|F|^2$, which includes the information of in-depth attenuation and multiple scattering [75]. The lattice factor $|G|^2$ provides the Laue condition $\Delta\vec{k} = \vec{g}$ with strong maxima for

$$\Delta\vec{k} \cdot \vec{R}_j = 2\pi n . \quad (2.11)$$

This lattice factor is determined by the lattice periodicity and arrangement of spots instead of providing the information of atomic position, which is already described in the previous section.

While traveling within a solid a charged electron undergoes inelastic scattering process, which suggests the electron beam should be attenuated and yielding a fairly

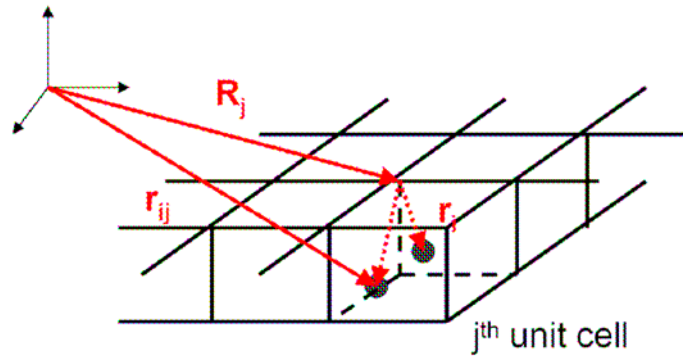


Figure 2.8: The position vector of atoms in j^{th} unit cell.

short mean free path (typically 10-20Å). The structure factor $|F|^2$ provides the information of penetration depth by introducing the imaginary part of the inner potential, which is alter the electron energy and its momentum k , the so called “optical potential”

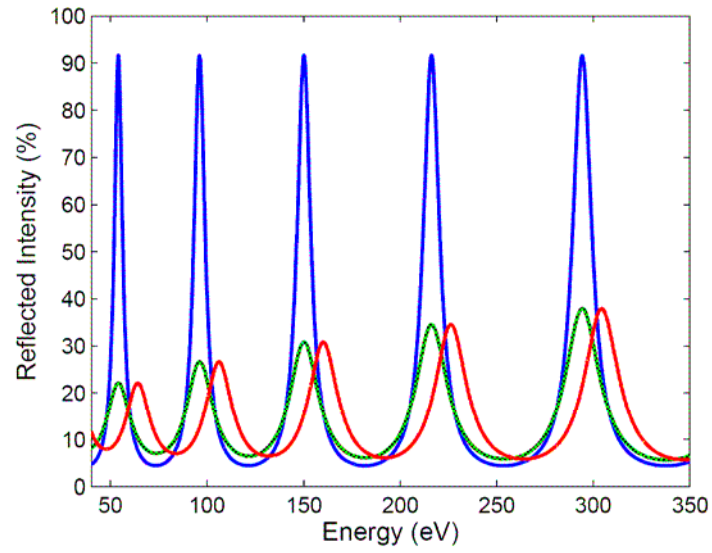
$$V_0 = V_{0r} + iV_{0i} . \quad (2.12)$$

Then, the penetration depth λ_p can be written as

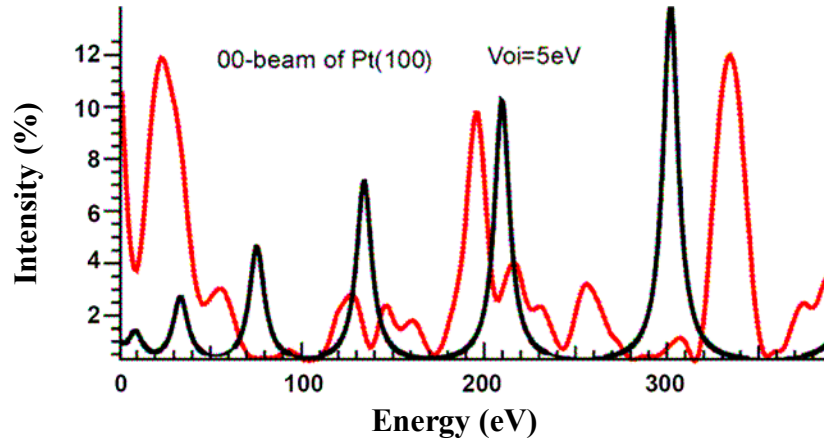
$$\lambda_p = \frac{\sqrt{2(E - V_{0r})}}{|V_{0i}|} \propto E^{1/2} . \quad (2.13)$$

Figure 2.9(a) exhibits the intensity as a function of energy with the different choices of constant real and imaginary parts of the inner potential [76], which shows the effects of the attenuation and shift of the peak intensities with respect to the different choices of V_{0r} and V_{0i} . This also shows the peak intensities are reduced as the beam energy decreases due to the penetration depth proportional to $E^{1/2}$. However, this kinematic approximation is totally different from experimental spectrum as shown in Figure 2.9(b), which suggests that we need to consider other factors such multiple scattering and diffraction (dynamic approximation).

Instead of direct solving the Schrödinger equation by considering the higher order scattering term in Born approximation, we can make use of scattering hierarchy (single atomic scattering, layer diffraction, and full surface diffraction) with multiple scattering as displayed in Figure 2.10 [75] and the corresponding approximation procedure known as Renormalized Forward Scattering (RFS) [77,78,79]. The single atom scattering in Figure 2.10(left) is based on the assumptions of spherically symmetric scattering potential mainly due to inner shells and nucleus. If wave functions overlap at the muffin-tin radius they are folded back to the inner of the atomic sphere. By solving



(a)



(b)

Figure 2.9: Kinetic approximation. (a) Intensity vs. energy with the different choices of constant real and imaginary parts of the inner potential [$V_{or} = V_{oi} = 0$ (Blue); $V_{or} = 0$, $V_{oi} = -5$ eV (Green); and $V_{or} = 10$ eV, $V_{oi} = -5$ eV (Red). Figures adapted from [76]. (b) Comparison of experimental spectrum (Red) and kinematic approximation (Black). Figures adapted from [73].

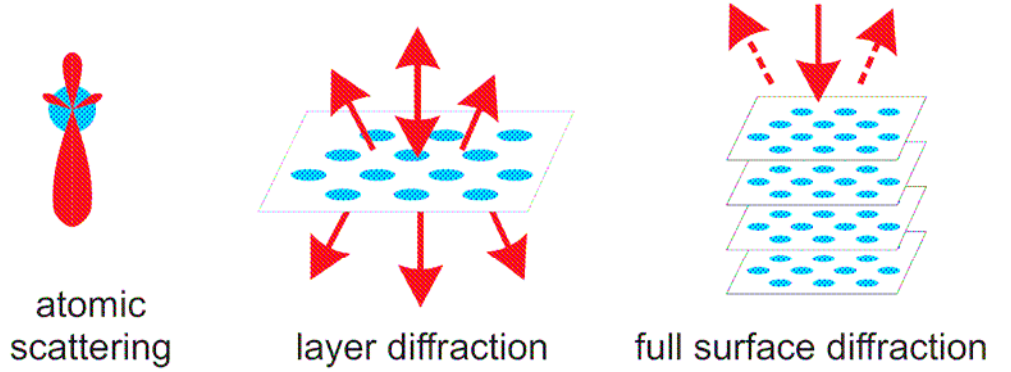


Figure 2.10: Hierarchy of dynamic (multiple scattering) LEED intensity evaluation. Figures adapted from [75].

the Schrödinger equation with ansatz

$$\Psi_l(r) \xrightarrow{r \rightarrow \infty} \alpha_l \frac{e^{ikr}}{2\pi r} + \beta_l \frac{e^{-ikr}}{2\pi r}, \quad (2.14)$$

the phase shift δ_l fully describe the multiple scattering inside the muffin-tin spheres. This phase shift can be obtained using the flux conservation outgoing and incoming wave must have the same modulus

$$\beta_l \equiv \alpha_l e^{2i\delta_l} \quad (2.15)$$

where phase shift δ_l has l cut off at a certain maximum value of the angular momentum. The layer diffraction in Figure 2.11(a) is considered by assembling atoms to layers and calculating the 2D diffraction, which consists of backward scattering and forward scattering, using the matrix inversion method [80]. Note that, even if only a single layer exists, multiple scattering should be taken into account because the total wave field impinging on the atom consists of the wave coming from outside plus that from the neighbors and even more, there is a contribution which depends on the scattering of the very atom itself [Figure 2.11(a)]. The full surface diffraction in Figure 2.11(b) is

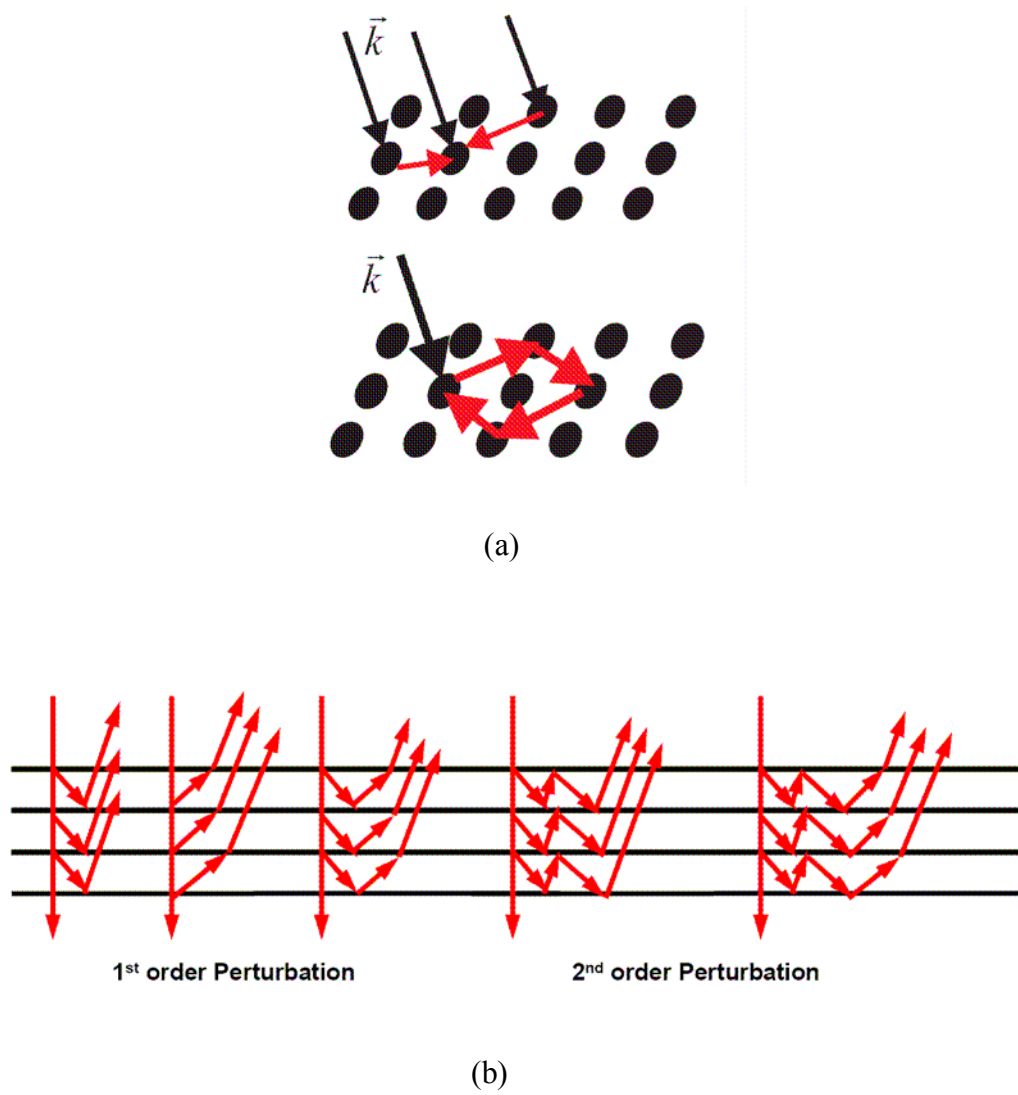


Figure 2.11: Multiple scattering. (a) Single layer only. (b) Multiple interlayer scattering in full surface diffraction. Figures adapted from [73].

considered by stacking the layers to build the surface and compute its diffraction. In this case, interlayer multiple diffraction between layers becomes important because the backscattering at moderate electron energies is significant and therefore multiple scattering events are probable instead of the kinematic approximation (weak backscattering). The preferred method for calculating interlayer multiple scattering is the RFS method as shown in [Figure 2.11\(b\)](#), which exhibits 1st or 2nd approximation procedure [\[77,78,79,81\]](#).

A dynamic spectrum due to multiple scattering or interlayer multiple scattering has much more peaks than a kinematic spectrum as shown in [Figure 2.12](#), which suggests that it has higher precision to an experimental spectrum and has more structure information. Correlation between the theoretical spectrum and experimental spectrum can be evaluated with the use of a reliability factor. Then, we need an optimization process where differently generated trial structure models are calculated and compared with experimental data. The trial structure which has the best correlation with experimental data is accepted as the true real space configuration of the atoms near the crystal surface. This dynamic approximation in LEED theory is necessary to describe the dependence between the geometrical atomic structure near the surface region of the crystal and the intensities of the diffraction spots as a function of incident beam energy, the so called “LEED I-V” spectra [\[82\]](#).

Reliability factor

In order to find the correct structure, the experimental spectra should be reproduced by model calculations which need a quantitative measurement to compare the

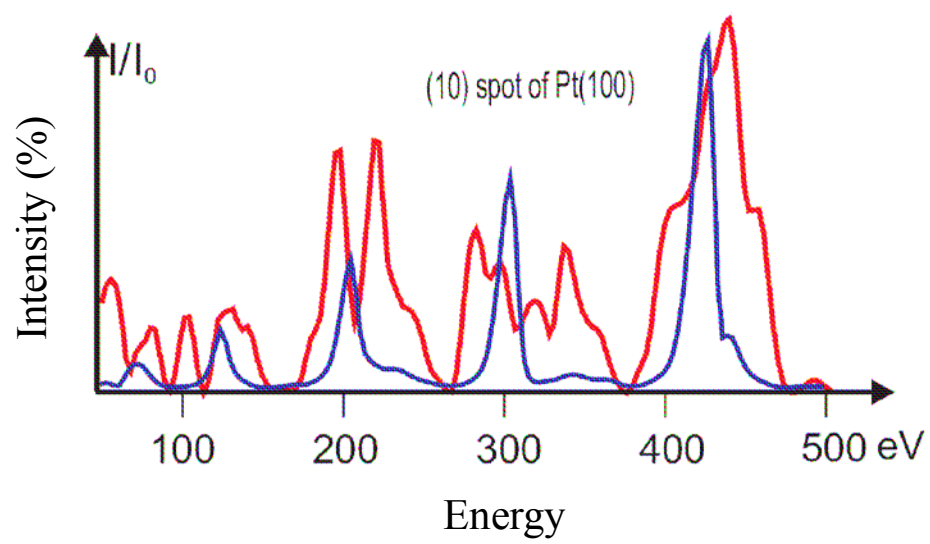


Figure 2.12: Comparison of kinematic spectrum (Blue) and dynamical spectrum (Red). Figures adapted from [73].

experimental spectra. For this reason, the reliability factors (R -factors) are widely used to evaluate the goodness of fit between the theoretical and experimental LEED I-V spectra. Due to the complex structure of the spectra, there are several R -factors [78] developed for LEED using different concepts for the construction. However, the mostly used R -factors in these days are the relative mean square deviations of intensities (R_2) or the Pendry R -factor (R_p) [83], which is more sophisticated than R_2 and will be used to evaluate our data. The advantage of R_p is the emphasis on the positions of maxima and minima than on the absolute height of intensities, which means all maxima are equally important even though weak and small peaks. This is true because their positions mirror constructive or destructive interference and reflect the structure in the IV spectra, which is a direct consequence of the geometrical configuration of atoms on the surface. Therefore, instead of the intensities, R_p is based on logarithmic derivatives with respect to energy

$$L(E) = \frac{1}{I(E)} \frac{dI(E)}{dE} . \quad (2.16)$$

When the IV curve is near a minima with $I(E) \approx 0$, a singularity occurs in the logarithmic derivative. To avoid singularities, a Y function

$$Y(E) = \frac{L(E)}{1 + (V_{0i} L)^2} \quad (2.17)$$

is used instead of $L(E)$. The Pendry R -factor then simply results as the mean square deviations of Y functions rather than of the intensities as in the case of R_2 :

$$R_p = \frac{\int (Y_{\text{exp}} - Y_{\text{th}})^2 dE}{\int (Y_{\text{exp}}^2 + Y_{\text{th}}^2) dE} \quad (2.18)$$

where Y_{exp} and Y_{th} are the Y functions for the experimental and theoretical beams

respectively. Perfect agreement corresponds to $R_p = 0$ (i.e. $Y_{\text{exp}} = Y_{\text{th}}$), uncorrelated spectra yield $R_p = 1$ (i.e. $Y_{\text{exp}} \cdot Y_{\text{th}} = 0$), and anti-correlated curves produce $R_p = 2$ (i.e. $Y_{\text{exp}} = -Y_{\text{th}}$). In general, the LEED community accepts a R_p below ~ 0.3 as a reliable solution for system containing a few atoms per unit cell. The variance of the R_p

$$\text{var}(R_p) = R_{p,\min} \sqrt{\frac{8V_{0i}}{\Delta E}} \quad (2.19)$$

where ΔE is the total energy range of the experimental data set. This variance of the Pendry R -factor allows estimation of the error limits for the model parameters determined [83].

2.4 Scanning Probe Microscopy

The development of scanning probe microscopy (SPM) allows us to study the surface science in range of phenomena from the micrometer down to the subnanometer scale. The family of SPM techniques is very diverse, with different methods specializing in different surface phenomena, such as surface topography, electronic properties, film growth, friction, dielectric and magnetic properties, contact charging, and many other phenomena. Here, we are focused on the two most commonly used techniques – scanning tunneling microscopy (STM) and atomic force microscopy (AFM). Both techniques have sharp tips interacting with the surface and a topographic surface image is produced by scanning. However, the control parameter of operation in STM is the tunneling current, whereas the control parameter in AFM is the atomic force between tip and sample.

2.4.1 Scanning tunneling microscopy and spectroscopy

The Scanning Tunneling Microscope (STM) was introduced by G. Binnig and W. Rohrer in 1981 which was honored by the Nobel Prize in 1986. It has become widely used as an important instrument for real space analysis in surface science. Scanning-tunneling microscopy (STM) can image surfaces of conducting materials with atomic-scale resolution. With its ultimate resolution, this remarkable instrument forms the basis of an enormous development within physics. Within one year of its invention, the STM helped to solve one of the most intriguing problems in surface science: the structure of the Si (111) surface [Figure 2.13]. A large number of metals and semiconductors have been investigated on the atomic scale and marvelous images of the world of atoms were created within the few years after the inception of the STM.

The basic idea is to bring an atomically-sharp metallic tip in close proximity (a few Å) to a conductive sample [Figure 2.14]. By applying a voltage between the tip and the sample a small electric current can flow from the sample to the tip or reverse, although the tip is not in physical contact with the sample. This phenomenon is called electron tunneling and its current can be measured. The magnitude of tunneling current depends on the distance between the tip and the surface. As the tip is moved laterally across the surface, a feedback mechanism moves the tip up and down to maintain a constant tunneling current. Restoring the tip across the surface therefore produces a topographic map of the surface. The extreme sensitivity of the tunneling current with respect to the tip-sample distance is the basis of vertical resolution in STM. By scanning the tip across the surface and detecting the current a map of the surface can be generated

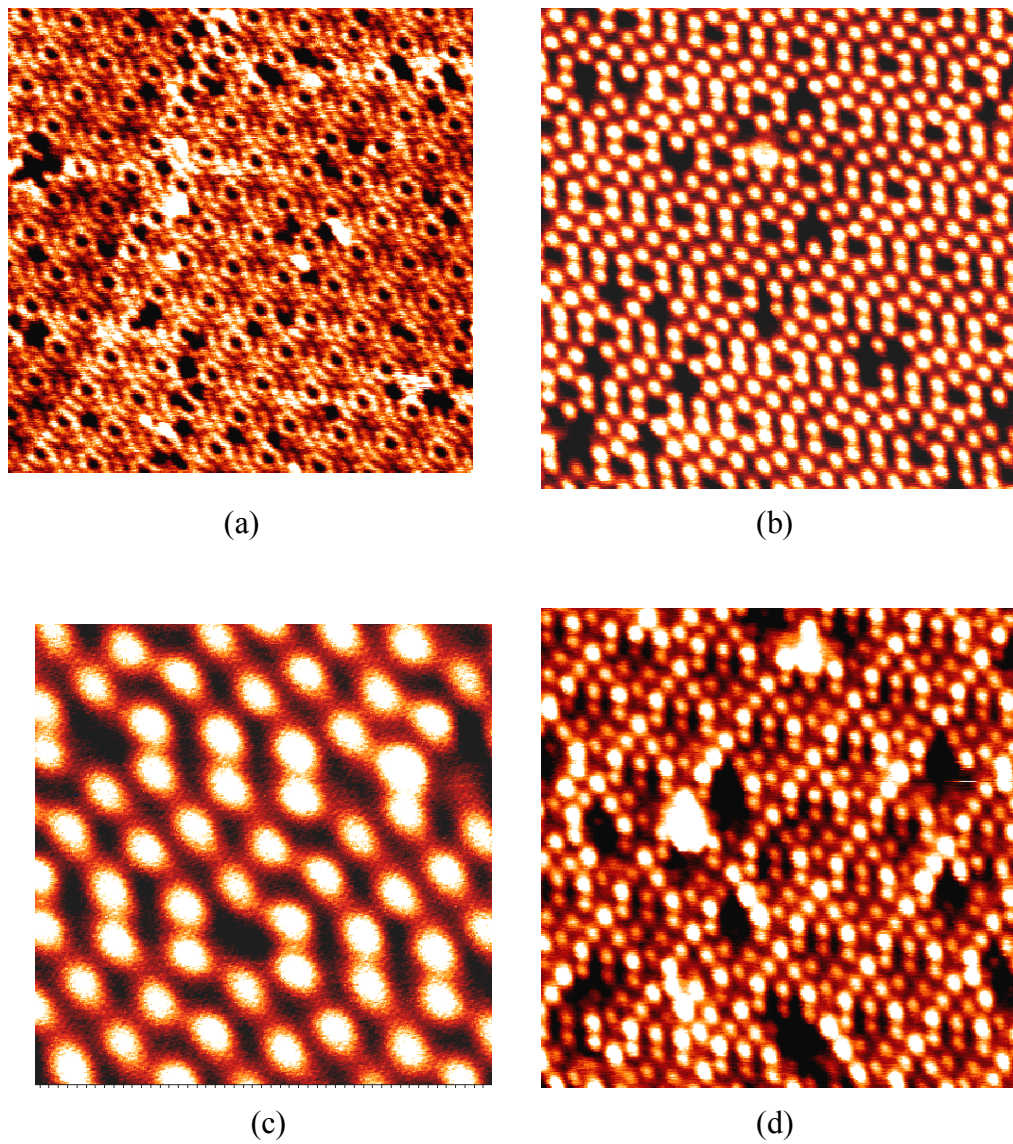


Figure 2.13: Atomically resolved STM images of Si (111) surface at RT: (a) 25 nm², +2.0V_{gap}, (b) 15 nm², +1.0V_{gap}, (c) 5 nm², +1.5V_{gap} and (d) 15 nm², -1.0V_{gap}

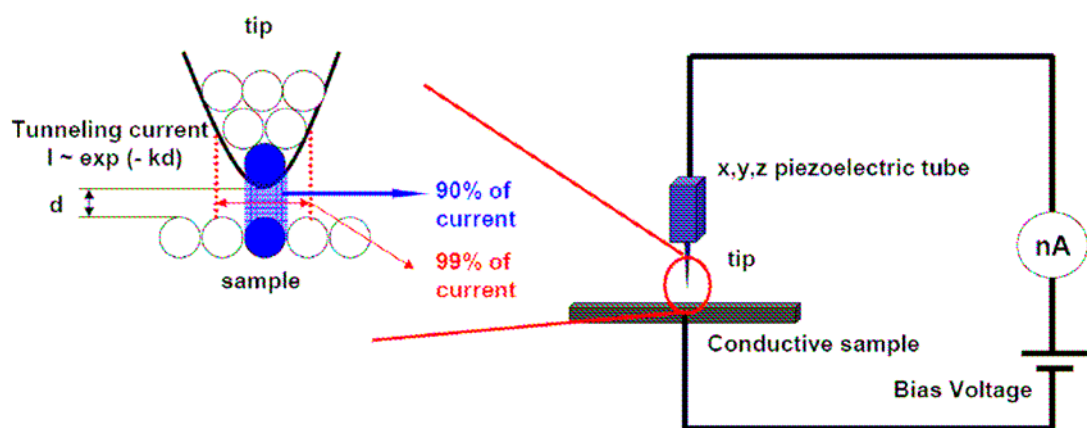


Figure 2.14: The principle of scanning tunneling microscopy.

with a resolution in the order of atomic distances. In reality a STM image is much more complex and rich with information. Note that the image cannot just be interpreted as a topographic map because the tunneling current is also influenced by the lateral and vertical variation of the electronic state density at the surface. The lateral resolution is about 1\AA whereas a vertical resolution up to 0.01\AA can be achieved.

Scanning tunneling spectroscopy (STS) performed with a STM is a technique which provides information about the local density of electronic states on surfaces at atomic scale. The tunneling current (I) is measured as a function of the bias voltage (V) between the tip and the surface at the measurement point. From this technique, the current-voltage (I - V) curve can be observed at every point in a data set, providing a three-dimensional map of electronic structure. With a lock-in amplifier, the differential conductance–voltage (dI/dV)- V curve can be collected directly. The tunneling current is proportional to the local electronic state, which is approximately estimated to

$$I \propto \int_0^{eV} \rho_s(E) \rho_t(-eV + E) dE, \quad (2.20)$$

where E is the electron energy based on the Fermi state of the sample, ρ_s is the density of the electronic state of the sample, and ρ_t is the density of the electronic state of the tip.

Differentiation yields the density of states

$$dI / dV \propto \rho_s(E_F - eV). \quad (2.21)$$

Actual spectroscopic images corresponding to the spatial variation of dI/dV contain topographic and electronic structure information.

2.4.2 Atomic force microscopy

Despite the phenomenal success of the STM, it has a serious limitation to conductive surface because of its control parameter - the tunneling current which flows between a biased tip and a sample. However, AFM, invented by Bininig, Quate, and Gerber in 1986 [84], does not require that the sample be an electrically conducting material. As shown in [Figure 2.15](#), the AFM consists of a microscale cantilever with a sharp tip (probe) at its end that is used to scan the specimen surface [85]. The AFM uses an atomically-sharp tip that is brought very close to the surface similar to STM while, as a control parameter, the tip of AFM feels atomic forces which lead to move up or down on its supporting cantilever. The key to the sensitivity of AFM is in monitoring the movement of the tip or the cantilever. The deflection is measured using a laser beam spot reflected from the top of the cantilever into an array of photodiodes. A feedback loop keeps the deflection constant by adjusting the vertical position of the cantilever while scanning along a surface. The feedback signal provides the topographical profile of the surface.

In principle, an AFM can operate in three primary modes, i.e., contact mode, non-contact mode, and tapping (intermittent contact) mode. In the contact mode, the tip senses the short-range repulsive forces exerted by the surface while in non-contact mode the tip senses the long-range attractive forces approaching of the sample surface [\[Figure 2.16\]](#) [86]. The forces act on the tip after approaching it to the surface causing a deflection of the cantilever. The tip altitude in the contact mode is adjusted to follow the surface height using the deflection signal. In this case, the force between the tip and the

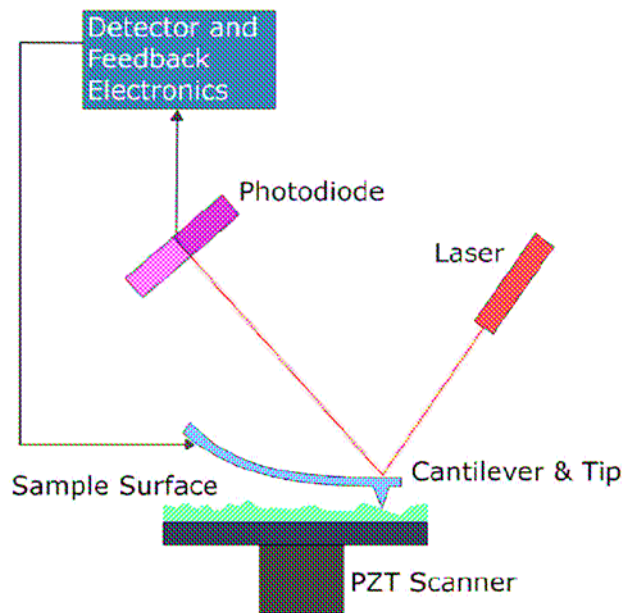


Figure 2.15: The principle of atomic force microscopy. Figures adapted from [85].

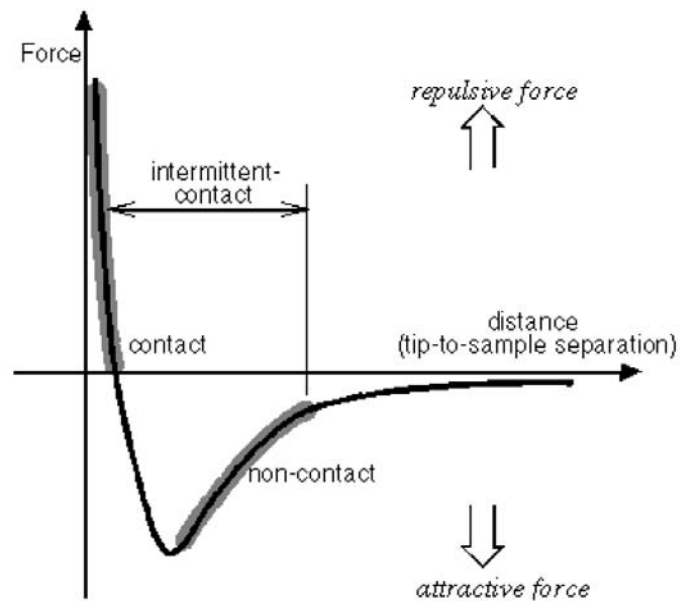


Figure 2.16: Distance dependence of atomic forces. The typical tip-surface separations expressed in the contact mode, non-contact mode, and intermittent contact mode. Figures adapted from [86].

surface is kept constant during scanning by maintaining a constant deflection. However, operation in the contact mode, which provides high quality of lateral resolution, typically implies relatively large shear forces that can damage the tip and the surface, limiting the range of samples that can be imaged. In the non-contact mode, the cantilever is externally oscillated at or close to its resonance frequency modified by tip-sample interaction forces in the attractive region. In this case, the tip does not contact the surface at all. Especially ambient conditions allow most samples to develop a liquid meniscus layer. Because of this layer, it is difficult to keep the probe tip close enough to the sample for contact mode to become detectable while preventing the tip from sticking to the surface. The tapping (intermittent contact) mode was developed to bypass this problem [87]. In the tapping mode, periodic tip-surface interactions provide the dominant contribution to the dynamic (oscillated) behavior of the cantilever.

In addition to morphology of the surface, progress in SPM is associated with the emergence of a large number of electrical, electromechanical, or magnetic characterization techniques enabled by several tip-surface interaction regimes (contact, non-contact, and intermittent contact). Especially, SPM based techniques have been successfully employed for the characterization of ferroelectric surfaces on the micron and nanometer level [88,89].

Chapter 3

Epitaxial thin film growth

3.1 SrTiO_3 substrate preparation

As one of the ABO_3 perovskite type, insulating strontium titanate (SrTiO_3) single crystal in [Figure 3.1](#) is an excellent substrate material for epitaxial growth of many oxide-based thin films. It provides a good lattice match to many materials with perovskite structure. At room temperature it exists in the cubic form with a lattice constant $a_c = 3.905 \text{ \AA}$ [\[90\]](#), but transforms into the tetragonal structure at temperature less than 105 K. The crystal structure of SrTiO_3 perovskite consists of an alternating stack of the two atomic planes (SrO and TiO_2), which provides two possible terminations of a perovskite (100) surface.

The surface structure of the substrate produces an important effect on the early stages of film growth. A single terminated surface is a prerequisite for reproducible thin film growth and fundamental growth studies. If the terminating layer is not uniquely decided, the mixture of two terminations coexists and degrades interfacial properties due to chemical and electronic uncertainty on a unit-cell scale. An ideal surface should have only one of the two terminations with a regular step structure. However, a surface obtained by polishing after cleaving or cutting results in an equal amount of two terminated domains separated by half unit cell steps with several kind of defects on the surface [\[91\]](#). Even if there were many methods to improve the surface quality and a

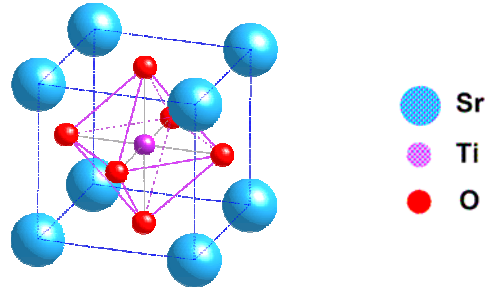


Figure 3.1: Schematic diagram of SrTiO_3 crystal structure in cubic unit cell at RT.

preferential termination for reproducible growth, these could not guarantee a single terminated surface before the first step by Kawasaki *et al.* [92].

Chemical treatment

In 1994, a near-perfect TiO_2 -terminated SrTiO_3 substrate with single-stepped surface was obtained by treating the crystal surface with a $p\text{H}$ -controlled NH_4F -HF (BHF) solution as described in Ref. [92]. Figure 3.2 shows the detailed procedure based on the selective etching of the more basic oxide SrO rather than acidic oxide TiO_2 by controlling the $p\text{H}$ value of the solution [93]. That is to say, the BHF etching removes Sr more efficiently than Ti, which suggests the etchant mostly attacks the Sr at the step edges, dissolving it and then removing Ti by lift-off. Following this etching, we can obtain very reproducible practically perfect TiO_2 -terminated surfaces on SrTiO_3 substrates. However, the $p\text{H}$ value of the BHF solution or the etching time is actually crucial for surface status. Under-etching results in non-perfect TiO_2 -termination with single-stepped surface, while over-etching causes unit cell deep holes in the terraces and

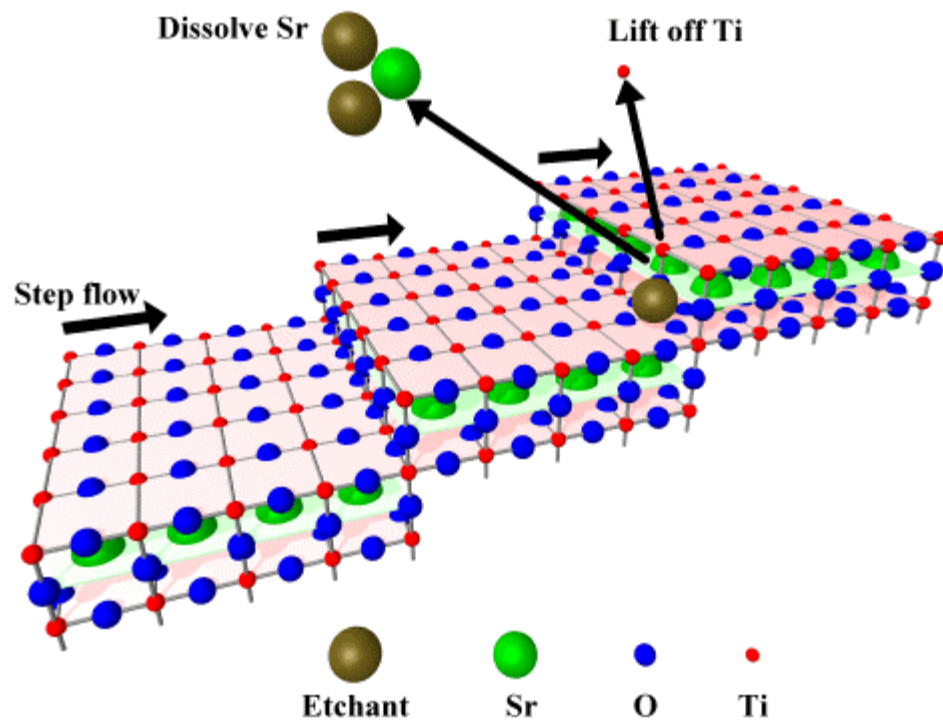


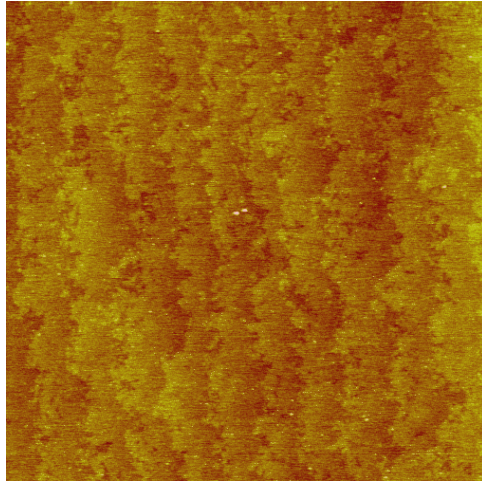
Figure 3.2: Chemical etching treatment. The procedure based on the selective etching of the more basic oxide SrO rather than acidic oxide TiO_2 . Figures adapted from [93].

deep etch pits, which hamper thin film growth. After Kawasaki *et al.*'s work, many literatures report the development of etching techniques, which provide us almost perfect etching conditions to get uniform TiO_2 terminated SrTiO_3 substrates with atomically flat surface [52,54,94,95].

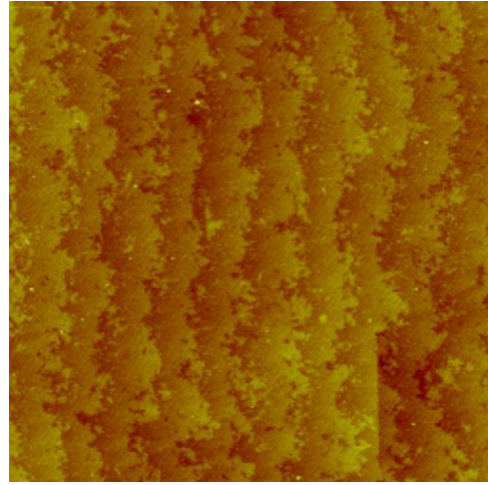
In our preparation prior to film growth [54,96], as-received (100) SrTiO_3 substrate (miscut tolerance $< 0.1^\circ$), purchased from CrysTec, Inc., is immersed for 30 s in a buffered oxide etch ($\text{BOE}:\text{H}_2\text{O} = 1:10$) with a pH equal to 4.5, then rinsed with distilled water, followed by thermal annealing which will be discussed next. The line profiles from AFM images for substrates before and after etching show terraces with typical height differences of half ($\sim 2 \text{ \AA}$) and single ($\sim 4 \text{ \AA}$) for before etching while single unit cell height of most terraces for after etching.

Thermal treatment

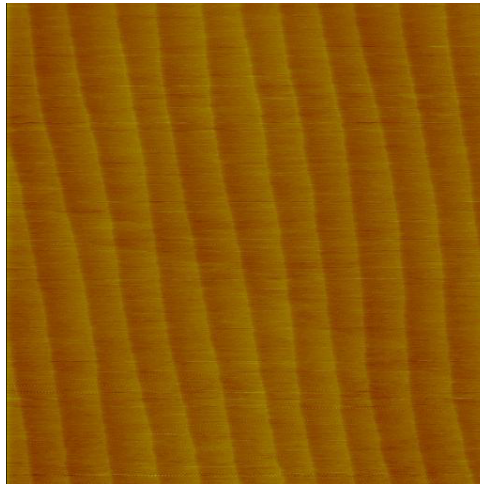
Even though the chemical etching contributes to form atomically flat surfaces of the substrate, a near-perfect single stepped surface of SrTiO_3 substrate requires additional thermal treatment in order to remove the remnants of the etching treatment and facilitate re-crystallization. AFM images of the etched SrTiO_3 (100) substrate surface before and after annealing in atmosphere are shown in Figure 3.3(b and c). The surface morphology of the substrate before annealing exhibits disordered step edges on the terraces which are broken into meandering islands. Despite the breakup of the surface edges, most of steps and small islands have a single unit cell height ($\sim 4 \text{ \AA}$). As annealing temperature increases, the small islands start to combine and form fairly broken terraces, and then wavy step edges become clearly visible (not shown). The thermal annealing at $\sim 1200^\circ\text{C}$



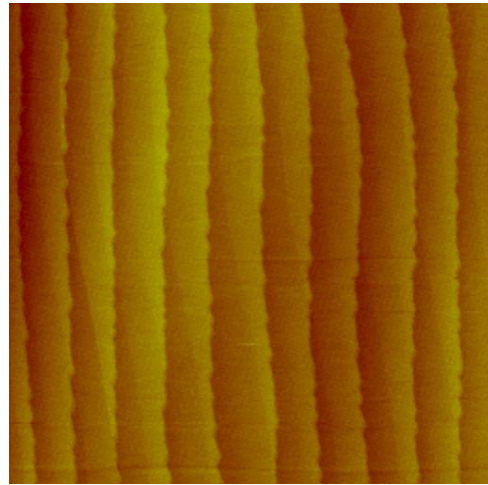
(a)



(b)



(c)



(d)

Figure 3.3: *Ex-situ* AFM topographic images of (100) SrTiO_3 substrates: (a) as-received, (b) after etching before anneal, (c) after etching and anneal at 1200 °C for 1 hour, and (d) after etching and anneal at 1350 °C for 1 hour. All image size is $5 \times 5 \mu\text{m}^2$.

for 1 hour in atmosphere provides perfectly straight step edges with fairly good terrace width, which can be partly controlled by annealing temperature and time [Figure 3.3(c)]. However, as shown in Figure 3.3(d), over-annealing causes jagged edges instead of straight terrace edges.

3.2 Epitaxial SrRuO₃ thin films

Strontium ruthenates have recently attracted significant attention due to their outstanding electrical transport properties [56,97]. The perovskite SrRuO₃ is broadly used as a conductive electrode for oxide electronics due to good conductivity and relatively small lattice mismatch to insulating SrTiO₃ substrate and many perovskite ferroelectrics. Especially, as shown in Figure 3.4, SrRuO₃ has a small lattice mismatch with SrTiO₃ (0.64%), which makes it possible to grow fully strained high quality 2D epitaxial films [52,94,98,99]. As an electrode, these high quality and fully strained SrRuO₃ films greatly affect getting the next growth components with high quality heteroepitaxial structure.

After confirming the high quality of TiO₂ terminated annealed SrTiO₃ substrate by AFM and XRD (FWHM < 0.03°), epitaxial SrRuO₃ thin films were grown by laser MBE using a KrF excimer laser ($\lambda = 248$ nm) at the substrate temperature 700 °C in 100 mTorr O₂. The average growth rate (deposition flux) was chosen as 0.059 ML/s controlled by the laser aperture size (8 x 23 mm²) and the repetition rate (5 Hz). During growth, high pressure RHEED was executed to monitor epitaxial growth of thin films in real time, which is shown in Figure 3.5(a). Ambient AFM images of 15 nm thick SrRuO₃

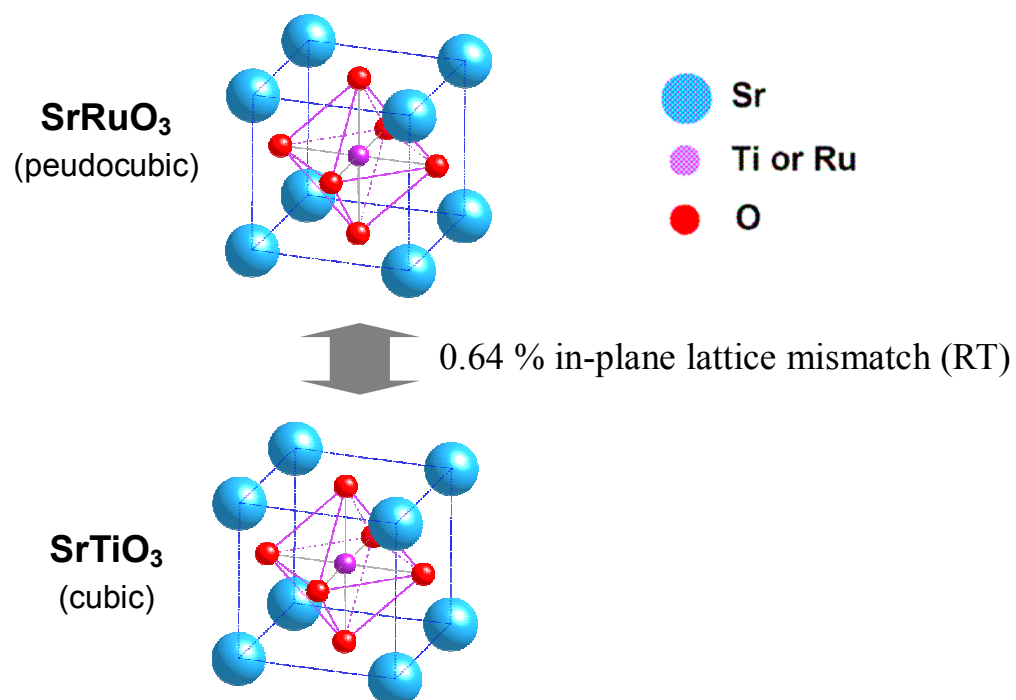


Figure 3.4: In-plane lattice mismatch between pseudocubic SrRuO₃ and cubic SrTiO₃ at RT.

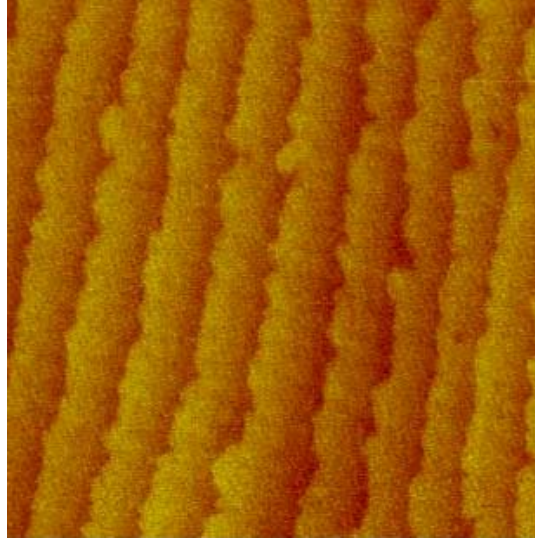
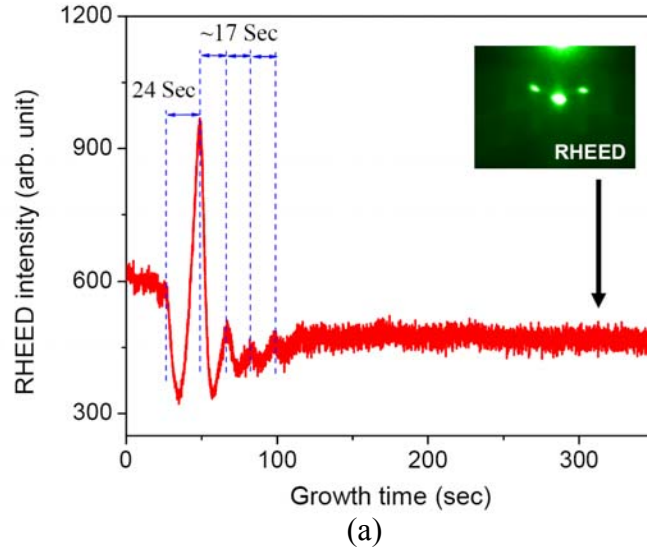


Figure 3.5: SrRuO_3 films growth. (a) RHEED oscillation and pattern during the growth of SrRuO_3 films on SrTiO_3 substrate. (b) *Ex-situ* AFM topography of 15 nm thick SrRuO_3 films after deposition (image size: $5 \times 5 \mu\text{m}^2$).

films after deposition [Figure 3.5(b)] illustrate a stepped topography – similar to that of the TiO_2 -terminated SrTiO_3 substrate prior to deposition – with a low step density and flat terraces. The crystalline quality of these films was also confirmed by measuring the rocking curve ($\text{FWHM} < 0.05^\circ$) for a (002) oriented SrRuO_3 thin films.

Figure 3.5(a) shows overall RHEED intensity variations of the specular spot during the growth of SrRuO_3 films, in which two regimes with different growth modes are distinguishable. The oscillation in the first regime indicates 2D layer-by-layer growth, whereas a steady RHEED signal in the second regime indicates 2D step flow growth, which is consistent with the previous reports [52]. The intermediate regime, in which the oscillations fade away, corresponds to the transition in growth mode from 2D layer-by-layer to step flow. The detailed study of the growth mode transition is discussed in Ref. [52].

During layer-by-layer growth, the periods of the first and second oscillations have different values (24 sec and 17 sec, respectively) while the oscillation periods are equal in time (17 sec) after the second oscillation [Figure 3.5(a)]. The different initial growth periods result from the change of perovskite stacking and stoichiometric deposition compared to TiO_2 -terminated SrTiO_3 substrate. While the first layer deposits, SrRuO_3 decomposes to stable SrO and highly volatile Ru_xO_y and this decomposition stops after the terminating layer is completely converted to SrO , which leads to take a little longer than deposition of other homoepitaxial layers. After that, perovskite stacking and stoichiometric deposition are preserved and the SrO -termination of SrRuO_3 films is observed in thin films. A detailed study of the termination of SrRuO_3 thin films is discussed in Ref. [99], which is consistent with our results.

3.3 Epitaxial BaTiO₃/SrTiO₃ thin films

Heteroepitaxial growth of perovskite thin films has been widely investigated since physical properties, such as dielectric, pyroelectric, piezoelectric or ferroelectric properties, can differ significantly from those of bulk crystals [37,38,39,40], allowing tunability of ferroelectric, conductive, and magnetic properties by strain and thickness effects. To grow a high-quality epitaxial film, a layer-by-layer (Frank-van der Merwe) growth mode is a prerequisite. Layer-by-layer growth is necessary for fully strained film deposition by the substrate without relaxation, which typically requires a small lattice mismatch between the film and substrate. For relatively large lattice mismatched materials, 3D island (Volmer-Weber) or layer-then-3D island (Stranski-Krastanov) are the energetically favored growth modes [Figure 1.6] [30].

Control over growth conditions can open pathways to self-assembly of nanophase materials with novel functional properties. Well-known examples include classical semiconductors such as Ge/Si, where nanodots with controlled geometry and unusual electrooptical and electronic properties can be formed. In oxide materials, the control over self-assembly is a much more challenging task, due to the limitations inherent in multi-component systems. These include propensity for oxygen and cationic non-stoichiometries, thermodynamic instabilities, and stringent conditions on lattice mismatch with substrate, resulting in a more restricted parameter space for growth processes. To date, successful examples of oxide self-assembly include successive growth of oxide nanodots as pinning centers in semiconductors [100] and self-assembled multiferroic structures [101]. In all these examples, self-assembly is primarily driven by

the interplay between macroscopic phase separation and strain energy between dissimilar phases.

In this Section, we report an experimental study of highly strained BaTiO₃ thin films on SrTiO₃ and demonstrate control over thermodynamic and kinetic parameters of deposition process to yield (a) layer-by-layer growth of excellent structural quality, highly oxidized, and highly strained epitaxial thin films and (b) pseudo-2D growth resulting in highly-ordered arrays of nanoscale islands of several unit steps high. The crossover between these mechanisms is controlled by growth temperature and deposition rate, which together determine the surface diffusion length [26,102]. This development opens the pathway for fabrication of high-quality films for applications such as ferroelectric tunneling barriers [33,65] and data storage and non-volatile memories [103,104], and produces novel materials in which long-range order and high uniformity of self-assembled nanoislands are combined with electric-field tunability of optical properties and switchable polarization to yield new classes of photonic nanostructures.

Bulk BaTiO₃ is a well-known ferroelectric with tetragonal lattice parameters at room temperature ($a = b = 0.3992$ nm and $c = 0.4036$ nm) [105]. Compared to cubic SrTiO₃ with a lattice parameter $a_c = 0.3905$ nm [105], the lattice mismatch, defined as $(a_{\text{films}} - a_{\text{substrate}})/a_{\text{substrate}}$, is a relatively large 2.23% [Figure 3.6], which suggests that layer-by-layer growth of BaTiO₃ films on SrTiO₃ will only occur in equilibrium conditions below a small critical thickness, above which lattice relaxation occurs and misfit dislocations are introduced [106,107,108,109,110,111]. Epitaxial growth can be obtained by changing the film stoichiometry, for example by introducing oxygen vacancies by growth at low oxygen pressures [112,113], but with associated degradation

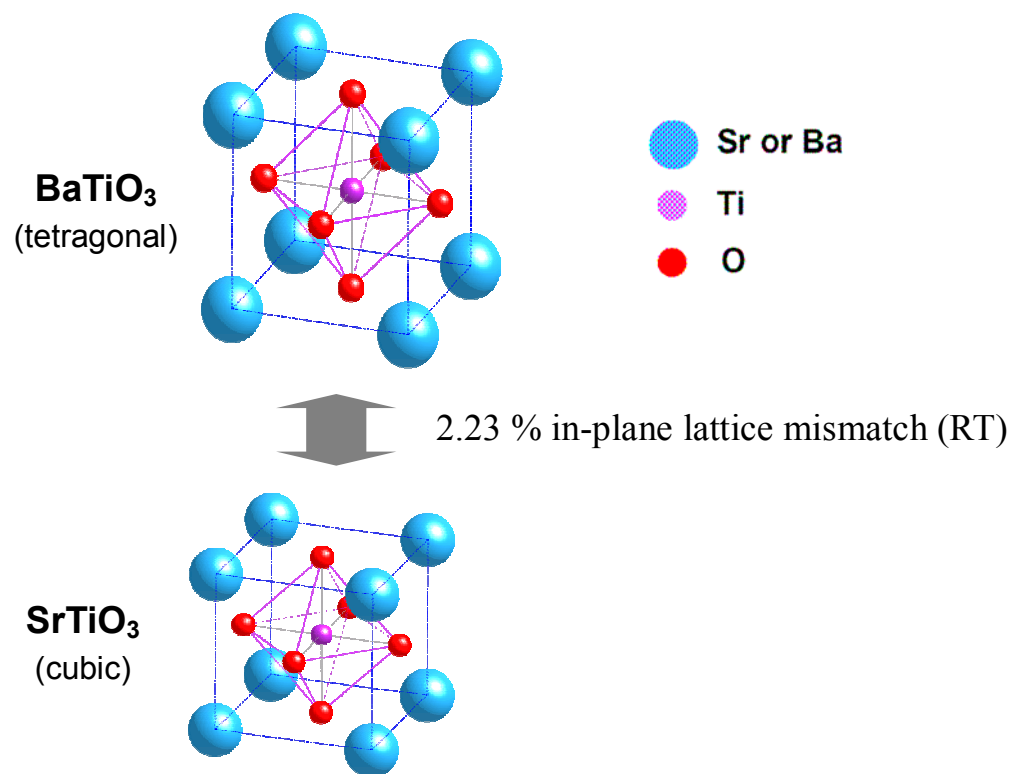


Figure 3.6: In-plane lattice mismatch between tetragonal BaTiO₃ and cubic SrTiO₃ at RT.

of electronic properties of the film. For oxygen pressures above ~ 1 mTorr equilibrium film growth produces island or layer-then-island growth modes due to lattice relaxation and dislocations [108,109,111]. Recently, the growth mode of epitaxial BaTiO₃ films on SrTiO₃ substrates fabricated by pulsed laser deposition (PLD) has been reported as layer-then-3D island growth with a ~ 5 nm critical thickness [111].

In this work, BaTiO₃ thin films were grown on (001) SrTiO₃ substrates by laser molecular beam epitaxy (laser MBE) using a KrF excimer laser ($\lambda = 248$ nm) incident on a high-density BaTiO₃ ceramic target at a repetition rate of 3 Hz. During deposition, two growth rates were chosen as 0.08 ML/s and 0.2 ML/s, the latter considerably higher than in previous publications. Growth parameters of substrate temperature and oxygen pressure were varied from 650 to 825 °C and 10 to 100 mTorr, respectively. TiO₂-terminated surfaces of (001) SrTiO₃ substrates were prepared with single unit-cell terrace steps and ~ 500 nm terrace widths by immersing oriented SrTiO₃ (miscut tolerance $< 0.1^\circ$) for 30 s in a buffered oxide etch with a *pH* equal to 4.5, then rinsing with distilled water, followed by thermal annealing at 1150 °C for 1 h in air [92,95]. RHEED patterns and intensities were recorded during the growth to monitor film quality and growth modes. The films were characterized by AFM, XRD, high pressure RHEED, and transmission electron microscopy (TEM).

For relatively low growth rates (0.08 ML/s, ~ 40 laser pulses per unit cell), only layer-then-3D island growth was observed throughout the ranges of substrate temperature (650 – 825 °C) and oxygen pressure (10 – 100 mTorr), consistent with previous reports [111]. To promote non-equilibrium growth, kinetic limitations were used to reduce the surface diffusion length, $l_d = \sqrt{D(T)\tau}$ where $D(T)$ is the temperature

dependent surface diffusion coefficient and τ is the mean residence time of atoms at the surface [26,102]. Both the substrate temperature and deposition rate were varied to affect surface diffusion length.

Kinetic limitations employed here have allowed highly strained epitaxial BaTiO₃ films to be grown on SrTiO₃ even at high oxygen pressures. Figure 3.7(a) shows a topographical image of a 125 nm thick BaTiO₃ film grown at a rate of 0.2 ML/s, ~15 laser pulses per unit cell, temperature of 650 °C, and oxygen pressure of 10 mTorr. The topography shows large atomically flat terraces, over 500 nm wide, separated by single unit cell steps of 0.4 nm, similar to that of the SrTiO₃ substrate prior to deposition. The Fourier transform of the surface topography [Figure 3.7(a) right] shows only a linear set of intense spots related to the step spacing. The associated RHEED pattern [inset Figure 3.7(a) left] obtained in-situ under growth conditions, exhibits a bright specular spot and diffraction pattern consistent with a smooth surface. During growth, RHEED intensities oscillate as shown in Figure 3.8(a, line I) with the formation of each layer. These oscillations are observed throughout the entire film growth and confirm that these flat 2D films are grown by a layer-by-layer mode.

The parameter window for this epitaxial growth was found to be quite narrow. Maintaining a high growth rate (0.2 ML/s) but increasing the oxygen pressure and temperature (P = 100 mTorr, T = 750 °C) leads to layer-then-3D island growth [Figure 3.7(b)] similar to that found with a relatively low growth rate. Only a few RHEED oscillations were observed under these conditions [Figure 3.8(a, line II)], consistent with layer-then island growth. The topographical image of a deposited 125 nm film [Figure 3.7(b) left] exhibits large irregular grains without distinct step edges and a high RMS

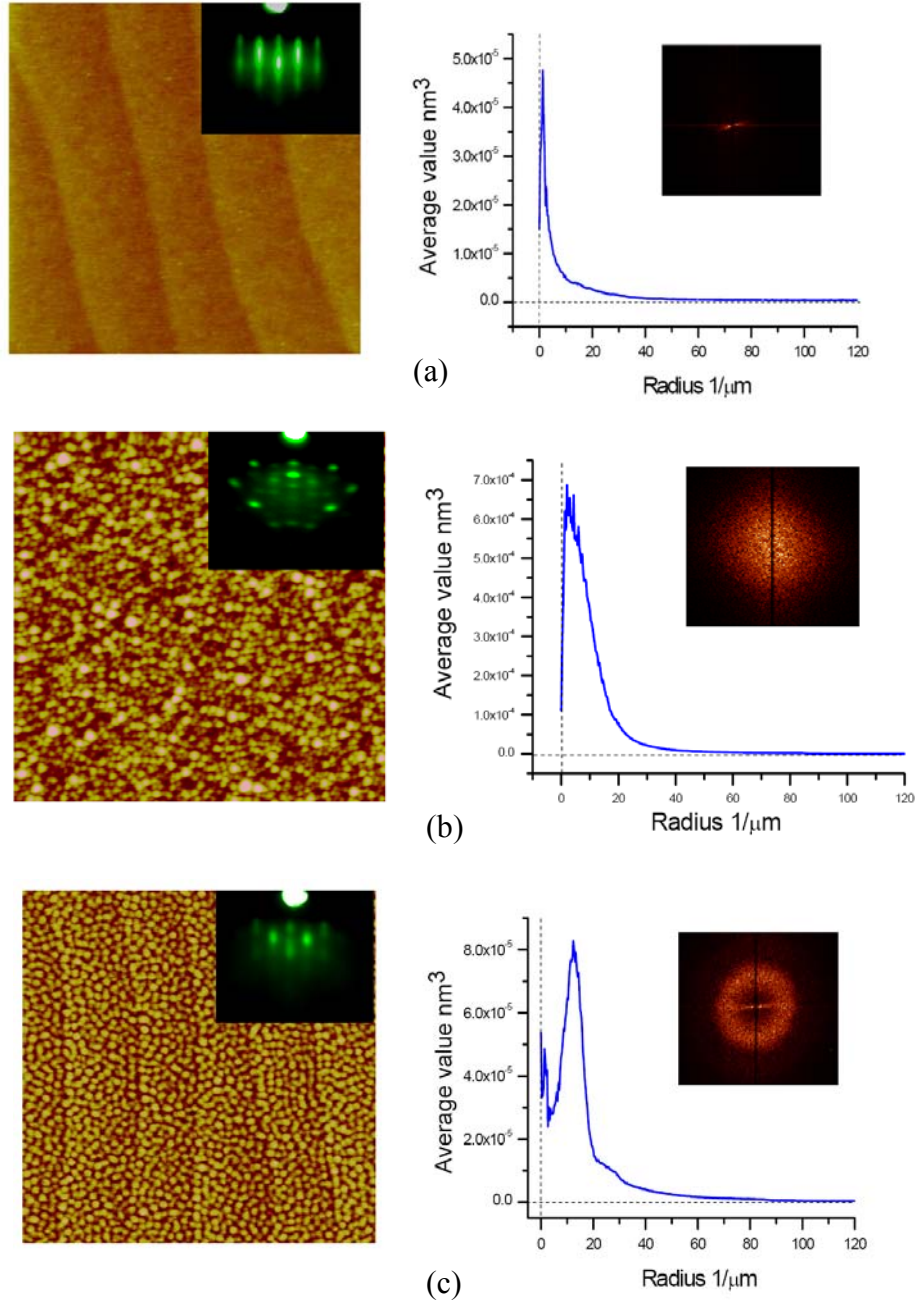
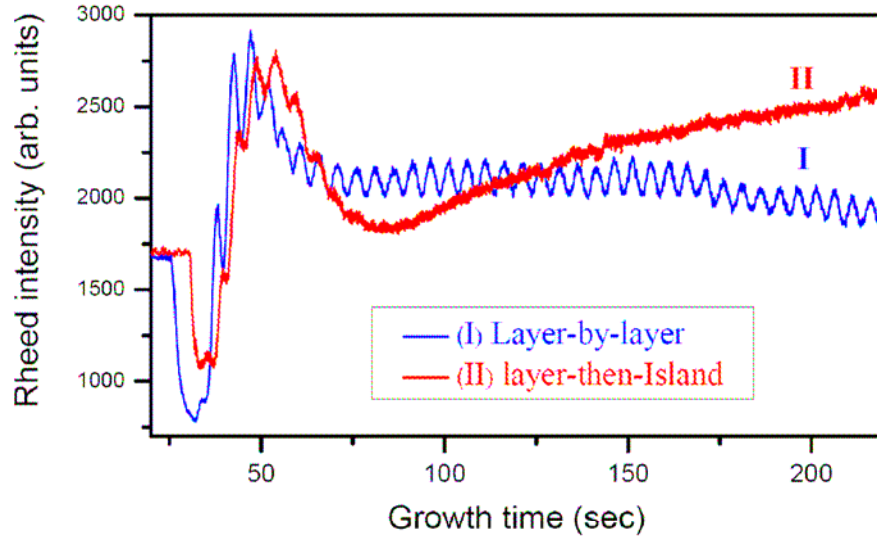
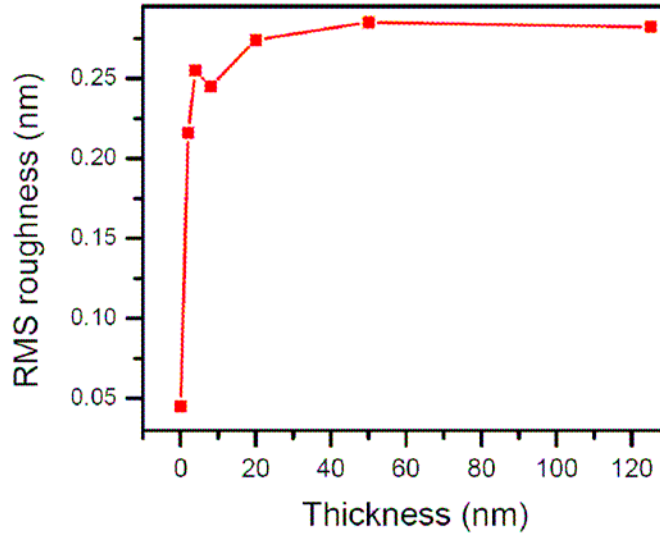


Figure 3.7: The surface of BaTiO_3 films after growth. AFM images ($3 \times 3 \mu\text{m}^2$ area) (left) and RHEED patterns (left inset) and Fourier transformed images with averaged radial profiles (right) of 125 nm thick BaTiO_3 films on SrTiO_3 substrates with growth modes of (a) layer-by-layer (650 °C and 10 mTorr), (b) layer-then-3D (750 °C and 100 mTorr), and (c) “pseudo-2D” (825 °C and 10 mTorr), respectively. All films are grown at 0.2 ML/s.



(a)



(b)

Figure 3.8: RHEED oscillation and roughness of BaTiO₃ film. (a) RHEED intensity oscillations observed during the epitaxial growth of 125 nm thick BaTiO₃ films grown layer-by-layer (650 °C and 10 mTorr)(line I) and pseudo-2D (750 °C and 100 mTorr) (line II). (b) Dependence of the roughness of BaTiO₃ films on the film thickness for pseudo-2D growth (P = 10 mTorr and T = 825 °C with 0.2 ML/s growth).

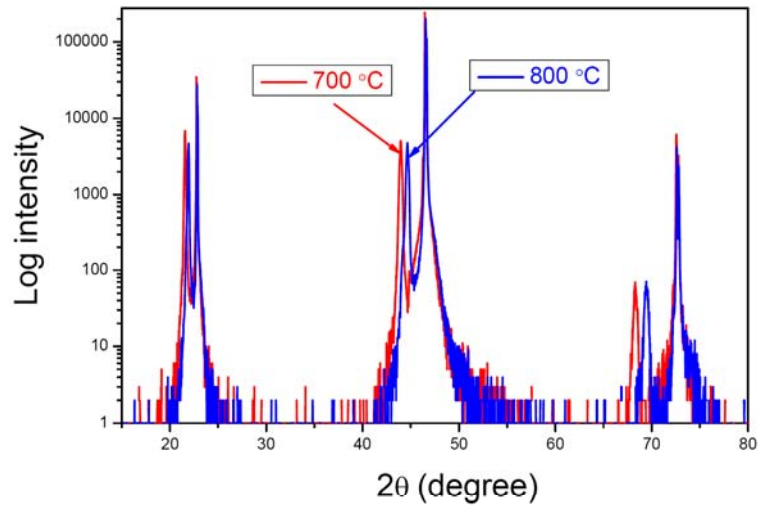
roughness of ~ 4.45 nm. The roughness increases monotonically with the film thickness [111]. Contrary to SrRuO_3 films on SrTiO_3 [114], BaTiO_3 films grown in high pressure exhibit more coarsened morphology in Figure 3.7 even if less intense bombardment and reduced surface diffusion occur during the growth [108,111,112]. This suggests that higher oxygen pressures lead to decreased compressive stress and reduced strain, resulting in lattice relaxation and dislocations in the films. This difference may be due to the larger lattice mismatch for BaTiO_3 than SrRuO_3 film on SrTiO_3 .

In contrast, increasing the growth temperature to 825 °C but maintaining the optimal oxygen pressure of 10 mTorr and growth rate of 0.2 ML/s produces an novel island growth mode [Figure 3.7(c)], which is different both from epitaxial two dimensional island [98] and lattice relaxed three dimensional island modes [Figure 3.7(b)]. We have labeled this new mode the “pseudo-2D” growth mode, since the average island size and effective roughness do not increase with film thickness. The height of the pseudo-2D islands is 2-4 several unit cells does not increase with film thickness. Furthermore, the islands coexist with step edges of terraces with single unit cell height even after 125 nm (i.e. > 300 unit cells) of film growth [Figure 3.7(c)]. Remarkably, the Fourier transform of surface topography shows pronounced short-range ordering (a ring in the FT image). The RHEED pattern [Figure 3.7(c), left inset] shows discontinuous spots with weak specular and diffraction spots, due to the islands. Similar to conventional layer-then 3D island growth, only a few RHEED intensity oscillations were observed. In Figure 3.8(b), the rms roughness of BaTiO_3 films grown by the layer-then pseudo 2D island mode is shown as a function of film thickness. Note that psedo-2D islands are nearly steady-state; once formed (above 5~ 10 nm), the film roughness does not increase

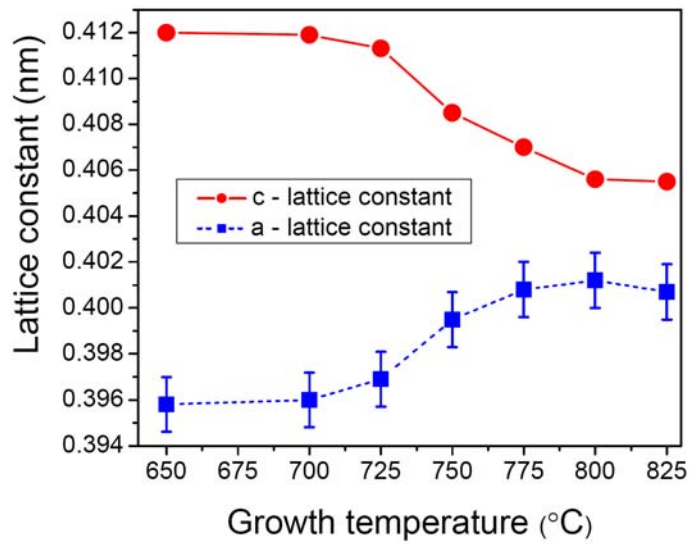
with thickness as it does for 3D islands [111], and the island size and density remains fixed, with evidence of island-island repulsion.

To investigate the crystallographic orientation and quality of these BaTiO₃ thin films, XRD θ -2 θ and ω scans were performed. Only SrTiO₃ (00n) and BaTiO₃ (00n) peaks for 125 nm thick BaTiO₃ films were observed [Figure 3.9(a)], indicative of high-quality and uniform orientation of deposited BaTiO₃ thin films. The peak shifts dependent on temperature are related to the change of the *c*- lattice constant. The full width at half-maximum (FWHM) of rocking curves of the BaTiO₃ 002 peak for all films studied including 3D island growth ranged from 0.045° to 0.096° confirming the high degree of crystallinity. Conversely, growth at <550 °C resulted in broadened rocking curves (~0.592°). This transition illustrates there is a minimum thermal energy for adatoms on the top of an island to diffuse to the edge of the island.

The measured *c* and *a*-values of the lattice constant for 125 nm BaTiO₃ thin films are shown in Figure 3.9(b) as a function of growth temperature (10 mTorr, 0.2 ML/s). Note the rapid cross-over from the values corresponding to layer-by-layer to layer-then pseudo 2D island growth at ~750 °C, indicating the transition from highly strained to fully relaxed films by pseudo-2D island formation (instead of 3D island) above this temperature. The onset of structural relaxation at high temperature arises from the increasing surface diffusion length [26,102] and a larger lattice mismatch due to different thermal expansion. Using bulk thermal expansion data for single-crystal BaTiO₃ and SrTiO₃ [115], the temperature dependence of the lattice mismatch between BaTiO₃ and SrTiO₃ becomes ~ 2.39% and ~2.47% at growth temperatures 650 °C and 800 °C respectively, values which are even larger than the ~2.23% lattice mismatch at 20°C.



(a)



(b)

Figure 3.9: XRD measurements. (a) θ -2 θ scans of BaTiO₃ films reveal a dependence on growth temperature. (b) The dependence of the out-of plane (Red) and in-plane (Blue) lattice constant of 125 nm thick BaTiO₃ films with growth temperatures. The transition corresponds to the shift from layer-by-layer to pseudo-2D growth.

Consequently the lattice mismatch for pseudo-2D island growth is greater than that for layer by layer growth, increasing the possibility of island formation and structure relaxation at higher temperature. From the XRD data, the average in-plane strain in BaTiO₃ films grown by the layer-by-layer mode can be approximately estimated at -1%¹, which is comparatively large enough to enhance ferroelectricity [39], while the average in-plane strain in BaTiO₃ films grown by the layer-then pseudo-2D island mode indicates that it is nearly fully relaxed. This suggests that two different growth modes have different density and possibly type of dislocations.

A comparison of cross-sectional TEM images² of the layer-by-layer and the layer-then pseudo-2D island growth modes clarifies the growth mechanism as related to dislocation networks. The bright field TEM images in Figure 3.10(a) and (b) of films grown by each growth mode respectively demonstrate features indicative of nearly straight threading dislocation lines propagating throughout the films. These dislocation lines are anchored by misfit dislocations at the substrate-film interface (inset on Figure 3.10(a)). The average density of dislocations³ in fully relaxed films grown by the layer-then pseudo-2D island mode can be estimated at ~5000 dislocations/ μm^2 , which is much larger than that of dislocations (~1000 dislocations/ μm^2) in highly strained films by layer-by-layer growth mode.

A correlation between the length scales in AFM images of the pseudo-2D islands

¹ This misfit strain is calculated using $s = a/a_0 - 1$, where a is the measured in-plane lattice parameter of strained films and a_0 is the in-plane lattice parameter of bulk BaTiO₃ at RT. The negative value of misfit strain means compressive strain in the films.

² The TEM images were obtained by A.Y. Borisevich.

³ The density of dislocations per area is given by $(1/a_s - 1/a)^2$, where a is the in-plane lattice parameter of BaTiO₃ films and a_s is the lattice parameter of cubic SrTiO₃ substrate.

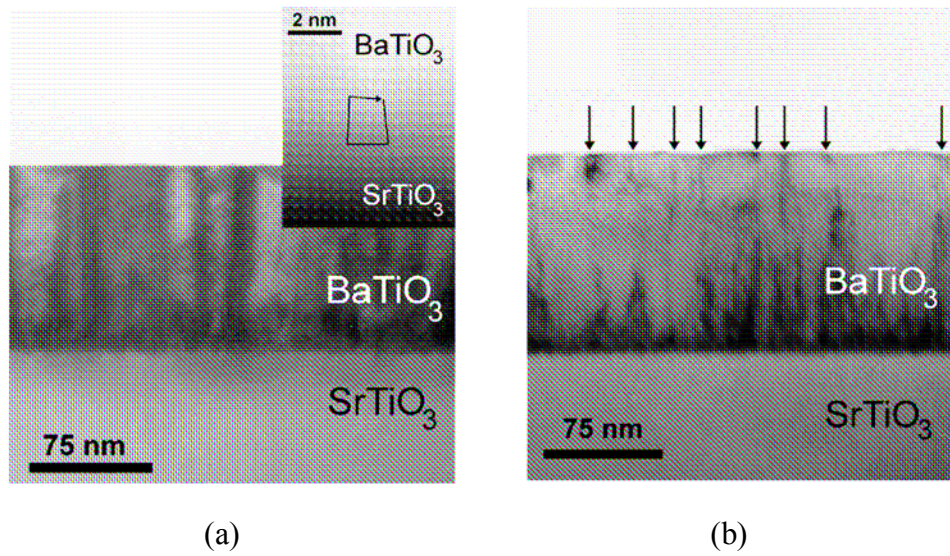


Figure 3.10: Cross-sectional TEM studies of BaTiO₃ thin films. (a) Bright field TEM image of a layer-by-layer (650 °C, 10 mTorr, 0.2 ML/s) film. Inset is a HAADF STEM image of a misfit dislocation at the interface. (b) Bright field TEM image of a pseudo-2D (825 °C, 10 mTorr, 0.2 ML/s) film. The arrows show linear features extending to the surface, indicative of threading dislocations.

Figure 3.7(c)] and in TEM images of the threading dislocations [Figure 3.10(b)] suggests a connection. The Fourier transformation of the topographic image in Figure 3.7(c, right) indicates that the layer-then pseudo-2D island growth has roughly periodic island formation on the surface quite different from the diffuse islands of layer-then 3D island growth. This Fourier image reveals that the islands in pseudo-2D growth are moderately uniform in size and tend to form a hexagonal array with an average distance between islands of ~ 65 nm (based on a maximum radial average of $\sim 15 \mu\text{m}^{-1}$). This distance roughly corresponds to the distance 20 – 80 nm observed between the threading dislocations in TEM image [Figure 3.10(b)]. This correlation suggests that the pseudo-2D island growth mode is related to the lattice of the threading dislocations, perhaps formed at the termination of screw dislocations at the surface, which are also expected to form a hexagonal array due to mutual repulsion.

To summarize, kinetic control achieved using high growth rates in a narrow window of high oxygen pressure and substrate temperatures enables unusual layer-by-layer and pseudo-2D island growth modes of BaTiO_3 on SrTiO_3 . Highly strained epitaxial films were grown despite a large lattice mismatch, as indicated by RHEED oscillations observed up to 125 nm during growth, atomically flat terraces with single unit cell steps. Higher O_2 pressures result in layer-then-3D island growth with only a few RHEED oscillations and rough surfaces. Higher temperatures lead to an unusual “pseudo-2D” growth, characterized by little surface roughness and islands with nearly uniform heights of a few unit cells and spacing of ~ 65 nm. This pseudo-2D island growth has not been previously reported and shows the unusual behavior of constant roughness independent of film thickness (above the first few unit cells) despite the

presence of islands with thickness greater than a single unit cell. TEM micrographs suggest that the islands are related to threading dislocations which extend through the films, although the exact relationship has not been established. The crossover between these three growth modes is strongly affected by kinetic limitation of adatoms and lattice mismatch between film and substrate.

These studies open a pathway for both better understanding of oxide thin film growth and control of the final morphology after deposition. The pseudo-2D growth reported here could lead to creation of arrays of ferroelectric nanoclusters with short-range order, opening routes to electrooptical photonic crystals and information storage applications. We have employed these growth conditions to produce high quality ultra-thin layers of BaTiO₃ on SrRuO₃/SrTiO₃ and have experimentally addressed polar ordering and polarization switching by *in-situ* low energy electron diffraction and scanning tunneling spectroscopy in [Chapter 5 and 6](#).

3.4 Epitaxial BaTiO₃/SrRuO₃/SrTiO₃ multilayers

In the previous section, we discussed the growth behavior for high quality films of ferroelectric BaTiO₃ on non-conducting SrTiO₃ substrate. However, the *in-situ* measurement of the physical properties using electron diffraction and scanning tunneling spectroscopy requires a conducting bottom electrode growth before deposition of BaTiO₃ films. Here, we discuss the growth of epitaxial thin BaTiO₃ films on SrO-terminated SrRuO₃/SrTiO₃, especially ultra-thin BaTiO₃ films (thickness ≤ 10 unit cells) with application of the growth conditions in the previous section. In [Chapter 5 and 6](#),

ferroelectric properties of these ultra-thin BaTiO₃ films on SrRuO₃/SrTiO₃ will be discussed by studying the structure and transport of ultra-thin films using LEED, STM, and STS.

Before the growth of ultra-thin BaTiO₃ films, ~ 15 nm thick SrRuO₃ films were grown with the same conditions shown in [Section 3.2](#) as a bottom electrode. To grow the high quality of ultra-thin BaTiO₃ films on SrRuO₃/SrTiO₃, we can apply the best conditions shown in [Section 3.3](#). Note that ultra-thin BaTiO₃ films still have ~2.23 % [\[Figure 3.11\]](#) lattice mismatch compared to the SrRuO₃ bottom electrode, which was fully strained to match the SrTiO₃ substrate. This suggests that the growth mechanism of BaTiO₃ films on SrRuO₃/SrTiO₃ might be similar to that of BaTiO₃ films on SrTiO₃. Without cooling after growing SrRuO₃ films on SrTiO₃, epitaxial ultra-thin BaTiO₃ films with thickness (10 ML, 4 ML, and 1~2 ML) were grown on SrO-terminated SrRuO₃/SrTiO₃ at the growth temperature 700 °C in 10 mTorr O₂. The average growth rate was chosen as 0.2 ML/s controlled by the laser aperture size (7 x 15 mm²) and the repetition rate (3 Hz).

High pressure RHEED was executed to monitor epitaxial growth of thin films in real time. During growth, RHEED oscillations of the specular spot were observed as show in [Figure 3.12\(a\)](#), which confirms that these flat 2D films are grown by a layer-by-layer mode. In this particular example, RHEED intensities oscillate 10 times, which corresponds to the formation of 10 layers of unit cell. The associated RHEED pattern [\[inset Figure 3.12\(a\)\]](#) obtained in-situ under growth conditions, exhibits a bright specular spot and diffraction pattern consistent with a smooth surface. After growth, BaO termination of BaTiO₃ films is expected because the RHEED oscillation periods are

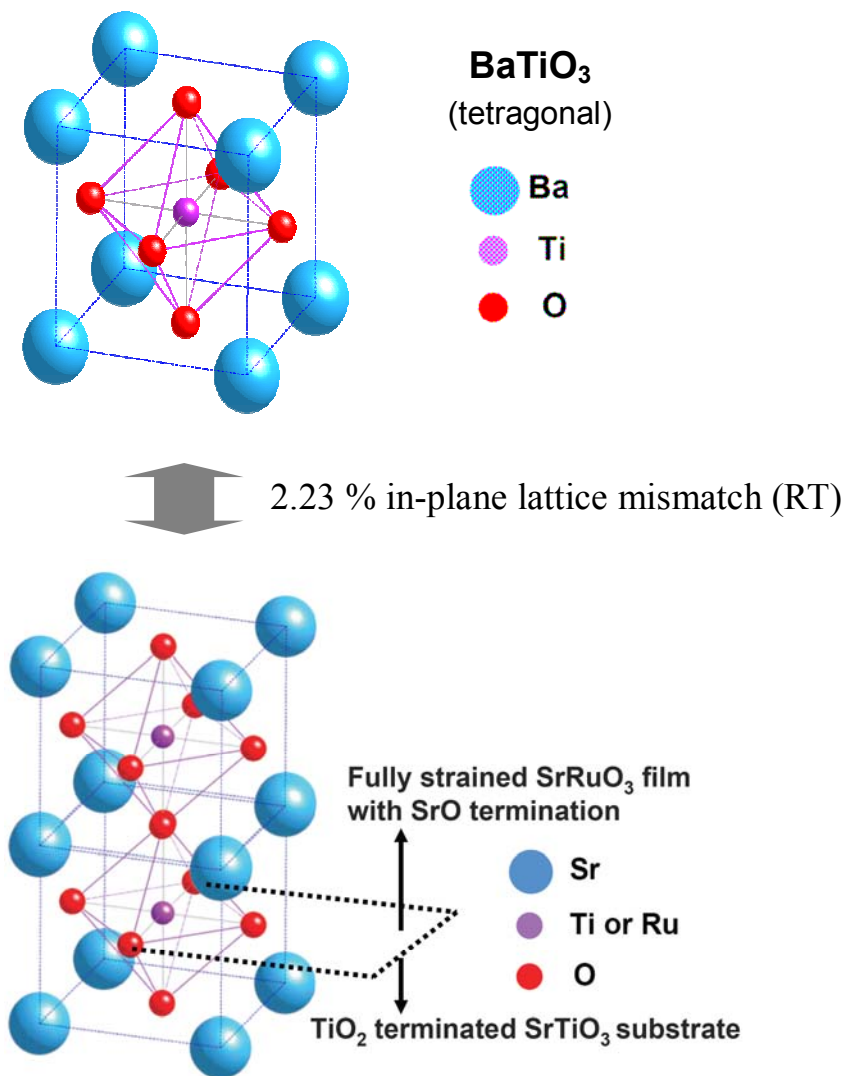


Figure 3.11: In-plane lattice mismatch between tetragonal BaTiO₃ and fully strained SrRuO₃ films grown on SrTiO₃ at RT.



93

equal in time, especially the first and second periods. This indicates no change of perovskite stacking and stoichiometric deposition compared to SrO-terminated SrRuO₃ electrode. This will be confirmed by LEED IV analysis in [Chapter 5](#). Ambient AFM images of 10 ML thick BaTiO₃ films after deposition [[Figure 3.12\(b\)](#)] illustrate a stepped topography – similar to that of the SrO-terminated SrRuO₃ films in Figure x prior to BaTiO₃ deposition – with a low step density and flat terraces. These RHEED and AFM results indicate that ultra-thin BaTiO₃ films have a very flat surface, suggesting that our films are highly strained by the bottom electrode SrRuO₃.

Chapter 4

Surface stability of epitaxial SrRuO₃ films: the need for *in-situ* analysis⁴

4.1 Introduction

Perovskite-type SrRuO₃ films have attracted significant attention in materials science and technology due to their outstanding electrical and magnetic properties. SrRuO₃ is also a promising electrode material for oxide electronic devices such as ferroelectric heterostructures and non-volatile ferroelectric random access memories (FeRAM), due to its high conductivity and low lattice misfit with many functional perovskite transition metal oxides [117,118,119]. Crucial for integrability of SrRuO₃ into the device fabrication process is surface stability with respect to reduction, contamination, or loss of volatile ruthenium oxides under high-vacuum conditions corresponding to PLD or MBE of the second component. Minute deviation in the stoichiometry of SrRuO₃ surfaces prior to the second component deposition could result in the formation of weakly conductive dead-layers that degrade device performance, including retention loss, fatigue, and reduced device capacitance.

Here, we investigate surface properties and thermal stability of epitaxial SrRuO₃ film surfaces and bulk under a range of carefully controlled conditions ranging from

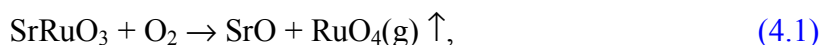
⁴ This chapter is based on the papers published in Ref. [54] and [116].

vacuum to an oxygen/ozone mixture. Films were studied using an array of surface probes including STM, x-ray photoemission and high resolution electron energy loss spectroscopies (XPS and HREELS), thermal desorption spectroscopy (TDS), and LEED and RHEED.

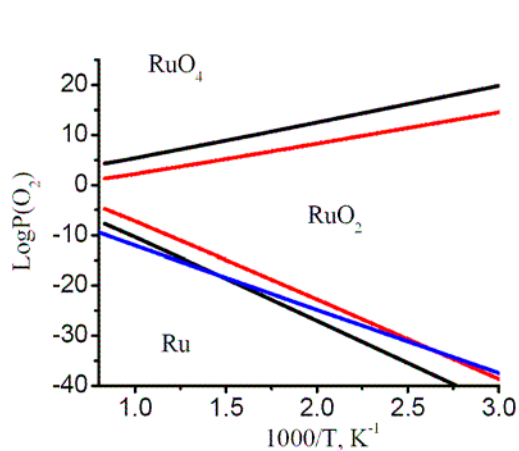
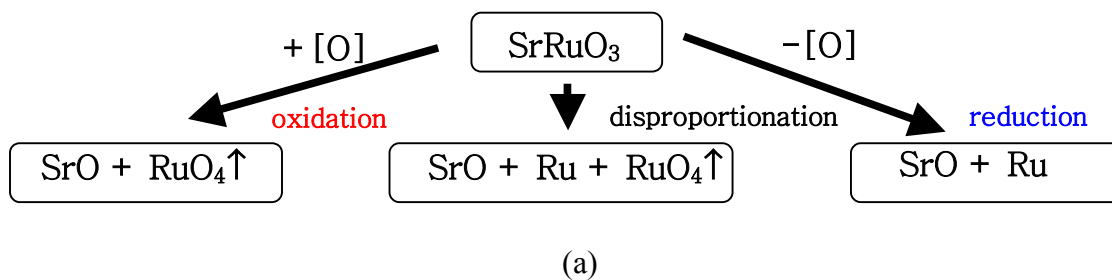
Results reveal that exposure to atmosphere, even for short times, leads to hydrocarbon contamination of the SrRuO₃ surface. This contamination reduces the stability of the surface, leading to decomposition and desorption at relatively low temperatures in vacuum. Removal of the hydrocarbons by preannealing in oxidizing conditions produces a surface stable above 600 °C in vacuum, comparable to the bulk SrRuO₃ stability, and compatible with conditions needed for deposition of additional oxide materials.

4.2 Thermodynamic analysis

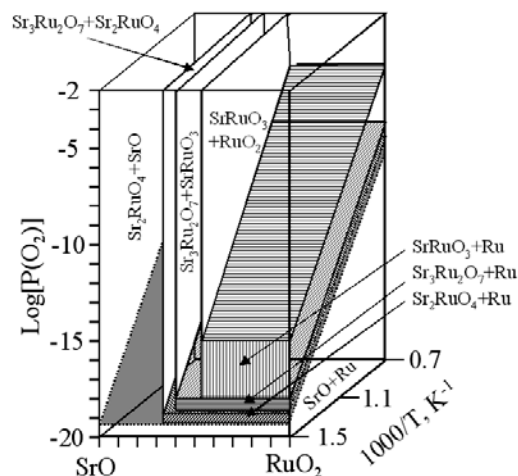
Functional properties of SrRuO₃-based thin films and devices are governed both by the bulk stability of strontium ruthenate and the surface behavior of the films. Bulk stability can be addressed using simple thermodynamic theory. In an oxygen-rich environment, a possible decomposition route for SrRuO₃ is oxidation (average oxidation state of ruthenium increases) with formation of volatile Ru oxides and ruthenium loss [Figure 4.1(a)]:



An alternative route for the decomposition of SrRuO₃ is disproportionation (where the average oxidation state of ruthenium remains constant) which is insensitive to the partial



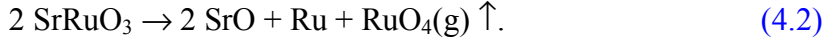
(b)



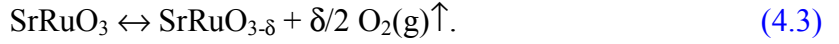
(c)

Figure 4.1: Thermodynamic analysis. (a) Possible decomposition routes for SrRuO_3 . (b) Ellingham diagram for RuO_2 and SrRuO_3 . Red lines delineate the stability region of RuO_2 (the decomposition pressure of $\text{RuO}_4(\text{g})$ is taken as 10^{-10} atm); Black lines delineate the stability region of SrRuO_3 . Blue line depicts the calculated partial oxygen pressure for $\text{pH}_2:\text{pH}_2\text{O} = 100$ (high vacuum conditions). (c) Approximate phase diagram for the $\text{SrO}-\text{RuO}_2$ system.

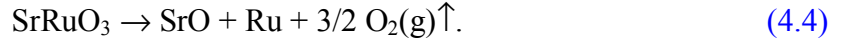
pressure of oxygen:



Under weakly reducing conditions, partial reduction with the formation of an oxygen deficient phase becomes likely:



Under strongly reducing conditions, SrRuO_3 reduces with formation of metallic ruthenium and SrO [Figure 4.1(a)] with possible formation of intermediate $\text{Sr}_{n+1}\text{Ru}_n\text{O}_{3n+1}$ phases:



In cases of Reactions 4.1, 4.2, and 4.4, the reaction is complicated by the fact that SrRuO_3 and SrO will not coexist in equilibrium and the decomposition process is likely to involve formation of the intermediate SrO -rich layered $\text{Sr}_3\text{Ru}_2\text{O}_7$ and Sr_2RuO_4 phases. Decomposition under oxidizing conditions by Reactions 4.1 and 4.2 involves the irreversible loss of ruthenium from the film. Partial reduction by Reaction 4.3 is expected to be reversible and will not result in the destruction of the film. Such behavior was previously reported by Bensch *et al.* [120] for bulk CaRuO_3 . Reduction under strongly reducing conditions by Reaction 4.4 involves the loss of oxygen and formation of SrO and metallic ruthenium and was reported to be the case for bulk SrRuO_3 in Ref. [120]. In this case, the SrRuO_3 phase can be restored by oxidative treatment, but the morphology of the film will be altered.

To estimate the thermodynamic stability of SrRuO_3 thin films for different temperatures and oxygen pressures, thermodynamic data for strontium ruthenates is required. The free energy of formation, ΔG_f , for SrRuO_3 , $\text{Sr}_3\text{Ru}_2\text{O}_7$, and Sr_2RuO_4 were

measured by Mallika and Sreedharan using a solid state electrochemical cell for SrO-Sr₂RuO₄-Ru, Sr₂RuO₄-Sr₃Ru₂O₇-Ru, and Sr₃Ru₂O₇-SrRuO₃-Ru mixtures with an O₂ reference electrode in the temperature range ~950-1200 K [121]. These measurements allow direct mapping of the P-T stability diagram (Ellingham diagram) for the SrO-RuO₂ system in this temperature range. Large uncertainties in the experimental measurements and lack of the heat capacity data limit these results to the temperature range of study. Nevertheless, this allows the stabilization energy of Sr-rich ruthenates compared to the SrRuO₃ to be estimated. At 1000 K, the Sr₂RuO₄ phase is stabilized by 5.2 kJ/mol compared to Sr₃Ru₂O₇ phase and by 11.2 kJ/mol compared to the SrRuO₃ phase, corresponding to the difference in the decomposition oxygen pressure of $\log P(\text{O}_2) = 0.27$ and 0.58 correspondingly. The thermochemical properties of corresponding calcium ruthenates were studied by Jacob *et al.* [122] using the potentiometric method with a RuO₂-Ru reference electrode. Corresponding stabilization energies of the Ca₂RuO₄ phase compared to Ca₃Ru₂O₇ and CaRuO₃ phases are 1.4 kJ/mol and 5.6 kJ/mol correspondingly. For both Ca- and Sr- ruthenates, the excess stabilization energies for the layered ruthenates are relatively small and do not exceed ~10 kJ/mol, corresponding in the relatively small variation in the decomposition pressure. Thermochemical properties of SrRuO₃ were also measured by Banerjee *et al.* [123] using a combination of microcalorimetry and fluoride electrochemical cell potentiometry. The free energy of formation for SrRuO₃ determined in Ref. [123] is smaller by ~50 kJ/mol compared to results in Ref. [121]. Here, we use the free energy of formation of SrRuO₃ as determined by Banerjee *et al.*, while the relative stabilization energies of Sr-rich phases are estimated from data in Ref. [121].

To estimate the stability of SrRuO_3 with respect to oxidation and reduction by [Reactions 4.1](#) and [4.4](#), an Ellingham diagram for $\text{RuO}_2\text{-O}_2$ and $\text{SrO-RuO}_2\text{-O}_2$ system was constructed as shown in [Figure 4.1\(b\)](#). The thermodynamic data for ruthenium oxides RuO_2 , RuO_3 , and RuO_4 was taken from [Ref. \[124\]](#) and free energies of formation, ΔG_f , for SrRuO_3 , $\text{Sr}_3\text{Ru}_2\text{O}_7$, and Sr_2RuO_4 are taken from electrochemical cell measurements by Mallika and Sreedharan [\[121\]](#). Large uncertainties in the experimental measurements and lack of heat capacity data from these references restrict application of these values but allow stabilization energies to be estimated. Note that thin film strain does not contribute significantly to chemical stability. Ruthenium trioxide RuO_3 is unstable with respect to disproportionation to RuO_2 and RuO_4 and is thus excluded from consideration. Since RuO_4 is volatile, the onset of decomposition by [Reaction 4.1](#) depends sensitively on the partial pressure of RuO_4 and the corresponding critical pressure was selected to be $P(\text{RuO}_4) \approx 10^{-10}$ atm. This pressure can be calculated from the Langmuir equation,

$$N = \frac{pA}{\sqrt{2\pi mkT}} \quad (4.5)$$

where p is the equilibrium vapor pressure, A is the area, and N is the evaporation rate which is given by 1 ML per hour. The reduction by [Reaction 4.4](#) does not include any gaseous products other than O_2 and corresponding decomposition pressures for RuO_2 and SrRuO_3 can be established unambiguously as shown in [Figure 4.1\(b\)](#). Also shown in comparison is the expected partial oxygen pressure expressed as the molar ratio of hydrogen to oxygen, $\alpha = p(\text{H}_2)/p(\text{O}_2)$, of order of $\alpha \sim 10\text{-}100$, as determined from mass-spectroscopic analysis of the gaseous mixture under typical high vacuum conditions.

A full P - T - x phase diagram for $\text{RuO}_2\text{-SrO}$ system calculated from data in [Ref.](#)

[121] is shown in Figure 4.1(c). SrO and SrRuO₃ do not coexist under equilibrium conditions; hence, the equilibrium reaction pathway for the decomposition of SrRuO₃ in all cases must include formation of intermediate Sr-rich phases such as Sr₃Ru₂O₇ and Sr₂RuO₄.

4.3 Experiment and results

4.3.1 Surface stability

As shown in Section 3.2, heteroepitaxial SrRuO₃ thin films (thickness 4–10 nm) were grown on TiO₂-terminated SrTiO₃ (001) substrates by laser MBE at 700 °C in 100 mTorr O₂ using a stoichiometric target. After growth, the high quality of films was confirmed by ambient AFM and XRD. The SrO-terminated SrRuO₃ films were also confirmed by Z-contrast scanning transmission electron microscopy (Z-STEM) and by RHEED as described in Section 3.2. After reinsertion into high vacuum ($\sim 10^{-9}$ Torr), a LEED pattern [SPECS ErLEED 1000] has been observed at room temperature as illustrated in Figure 4.2, confirming a well-ordered surface structure even after extended (> 1 day) exposure to air. This behavior is relatively unusual for transition metal oxides; few metallic materials, with Au the noted exception, exhibit a LEED pattern after exposure to air.

Interestingly, LEED patterns irreversibly disappear after annealing for 10 minutes in high vacuum ($\sim 10^{-8}$ Torr) at temperatures as low as ~ 100 – 200 °C, indicating

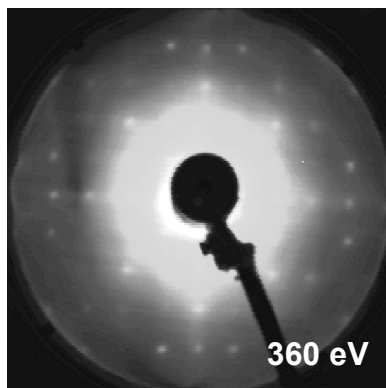


Figure 4.2: *Ex-situ* LEED pattern of SrRuO₃ films at RT. The sample was exposed to air for 1 day.

surface disordering (not shown). To quantitatively investigate the thermal behavior of the surface and determine the stability regions for strontium ruthenate, SrRuO₃ thin films have been annealed in high vacuum by steps of 100 °C up to 800 °C and studied by STM, electron spectroscopies including HREELS and XPS. The chemistry of decomposition products was examined by TDS and the evolution of surface crystallographic structure determined by RHEED.

4.3.2 STM analysis

Evolution of the surface morphology due to annealing was studied by STM (Omicron STM-1, PtIr tips) in high vacuum ($\sim 1 \times 10^{-8}$ Torr). The surface of air-exposed SrRuO₃ exhibits unit cell steps; at the same time, large number of irregularly shaped white particles can be observed on the terraces [Figure 4.3(a)]. Based on the HREELS data [Section 4.3.4], the particles can be identified as hydrocarbon contaminates. After

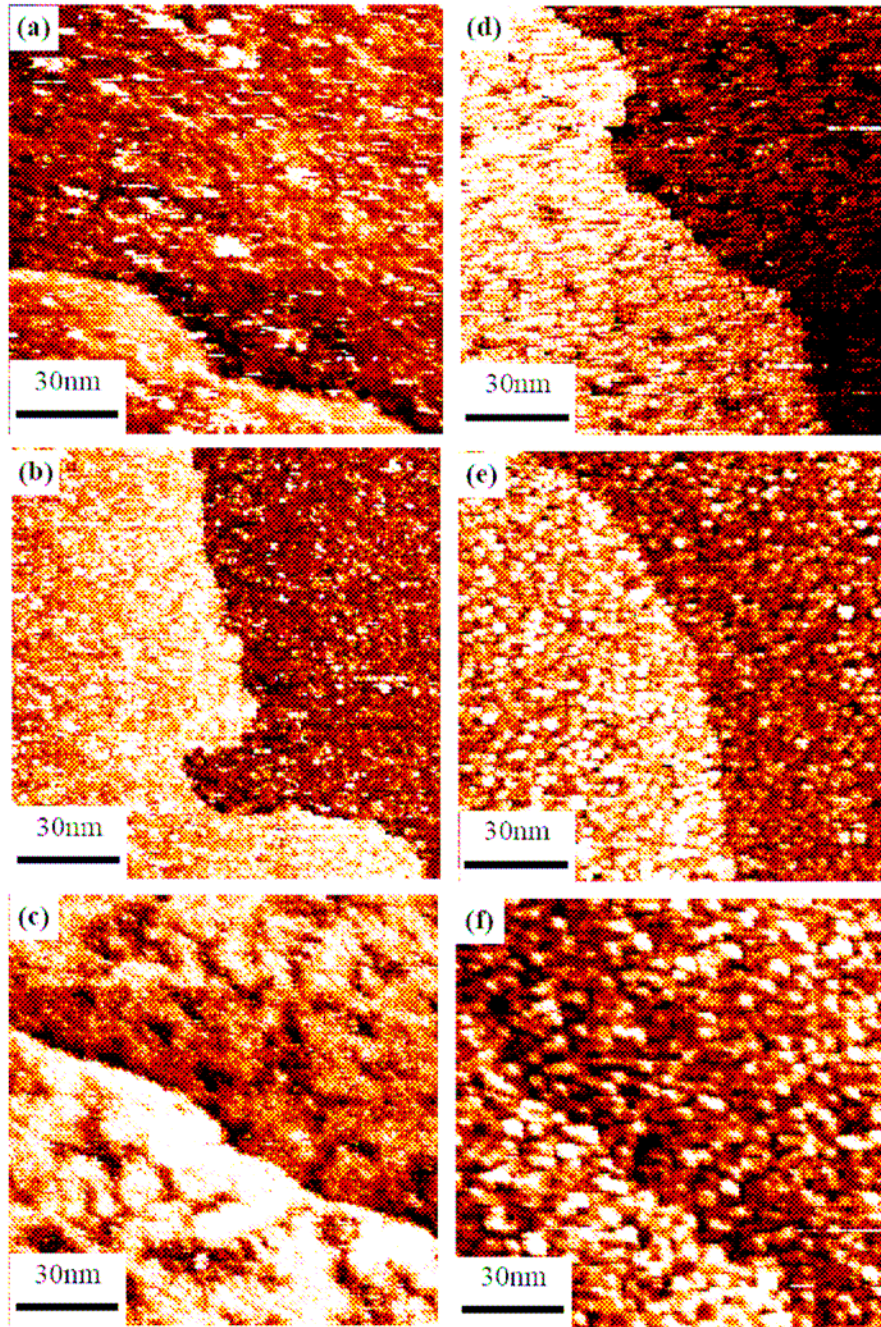
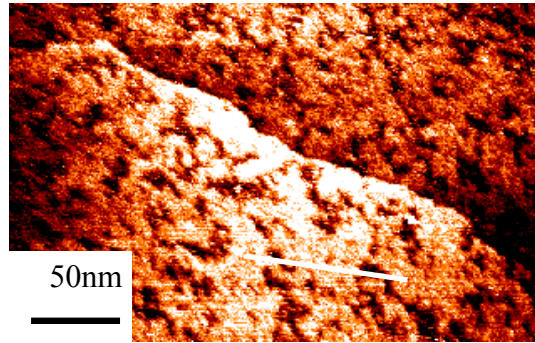


Figure 4.3: STM images of SrRuO_3 film dependent on temperature. (a) As-grown, air-exposed SrRuO_3 thin film and films annealed at (b) 200 °C, (c) 300 °C, (d) 400 °C, (e) 500 °C, and (f) 700 °C in high vacuum ($\sim 1 \times 10^{-8}$ Torr).

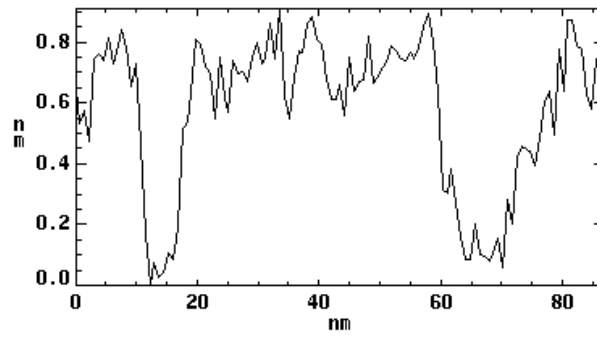
annealing to 200 °C and cooling to 30 °C, the number of particles decreases and their distribution becomes more uniform [Figure 4.3(b)]. By 300 °C, surface contaminants disappear and a number of irregular pits become apparent [Figure 4.3(c)]. Figure 4.4 shows the dimension of these pits is 10–20 nm wide and 1–2 unit cell depth [the pseudo-cubic lattice parameter of SrRuO₃ is 0.393 nm at room temperature] [125]. The appearance of pits can be correlated with TDS data [Section 4.3.3], where loss of SrO and metallic Ru is observed in this temperature range. Pit widths become smaller after annealing to 400 °C [Figure 4.3(d)]. After annealing above ~ 500 °C, spherical particles develop from the unstable layer(s) and increase in size with annealing temperature [Figure 4.3(e) and (f)]. After annealing as high as ~ 700 °C, atomic steps can still be observed, which provides evidence that only a few layers of SrRuO₃ have decomposed and contribute to the spherical particles, while the bulk of the material is stable. Ambient AFM images of the film after vacuum annealing to 1200 °C indicate complete decomposition of the SrRuO₃ film and formation of large (~100-200 nm) particles (not shown).

4.3.3 Thermal Desorption Spectroscopy

To establish the decomposition pathway for SrRuO₃ films in high vacuum conditions (below 10⁻⁷ Torr), volatile products desorbing from the surface were identified using TDS in the temperature range 30–1200 °C with results shown in Figure 4.5. The film was heated by electron bombardment, and the desorption rates of possible volatile components were determined as a function of temperature using a quadrupole mass



(a)



(b)

Figure 4.4: Depth of Pits on the surface of SrRuO₃ films. (a) STM image of an air-exposed SrRuO₃ thin film annealed at 300 °C and (b) the cross section along the line shown in (a).

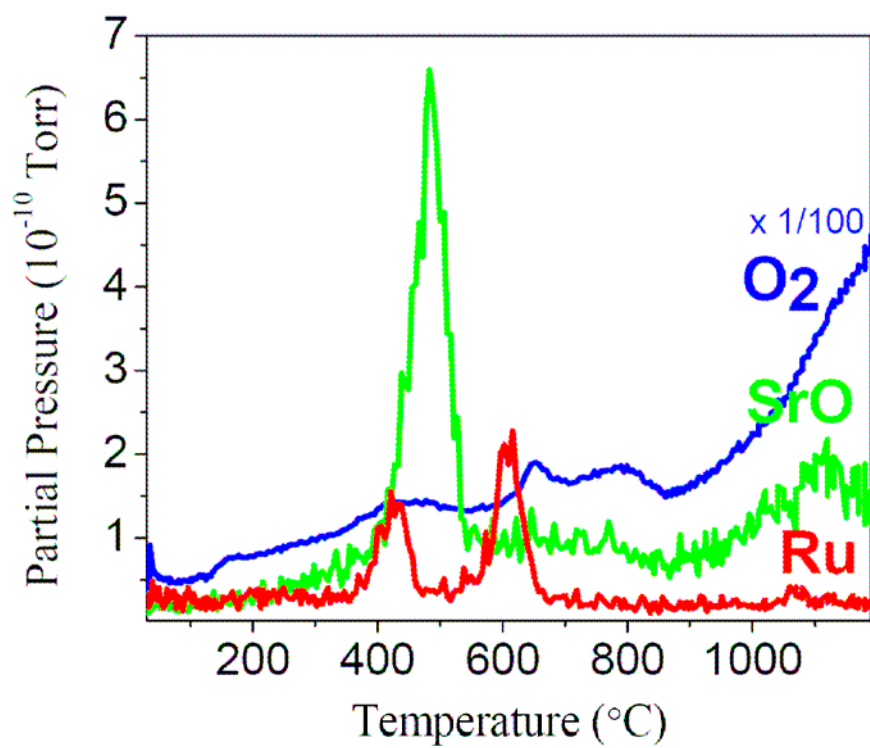


Figure 4.5: TDS from SrRuO₃ film in high vacuum as a function of temperature.

spectrometer [RGA 200, Stanford Research Instruments]. The only volatile forms of Sr and Ru desorbing from the surface were SrO and metallic Ru; no metallic Sr or ruthenium oxides RuO_n , $n = 1, 2, 3, 4$, were detected, in agreement with thermodynamic calculations. The desorption of SrO and Ru starts at $\sim 350^\circ\text{C}$; the amount of desorbed material is relatively small, indicating the decomposition of surface layers, and not complete bulk decomposition. Interestingly, a second peak corresponding to metallic Ru is observed at $\sim 600^\circ\text{C}$. The bulk decomposition of SrRuO_3 starts at $\sim 900^\circ\text{C}$ as indicated by continually increasing oxygen desorption from the surface; no volatile metal-containing products are detected at this temperature. Finally, annealing at very high temperatures ($\sim 1200\text{--}1400^\circ\text{C}$) results in massive loss of Ru, Sr and Ti containing species from the surface, indicative of complete decomposition of the films.

4.3.4 Electron Spectroscopies of Surface Chemistry of SrRuO_3

To identify adsorbates on the SrRuO_3 surface, the sample was studied by HREELS⁵ [LK2000 HREELS] in high vacuum (below 10^{-7} Torr). The corresponding spectrum after ~ 3 day exposure to air is shown in [Figure 4.6](#). On the large tail of the elastic peak, the experimental spectrum shows energy loss peaks at 29 and 50 meV that can be attributed to phonon modes, similar to phonons in layered Sr_2RuO_4 [126]. No energy loss peaks corresponding to O-H (stretching mode between 400-450 meV) were observed, indicative of chemical stability of the surface with respect to hydroxylation. At the same time, the HREELS spectrum contains multiple peaks at 130-175 and 369 meV

⁵ The HREELS data were obtained by R.G. Moore.

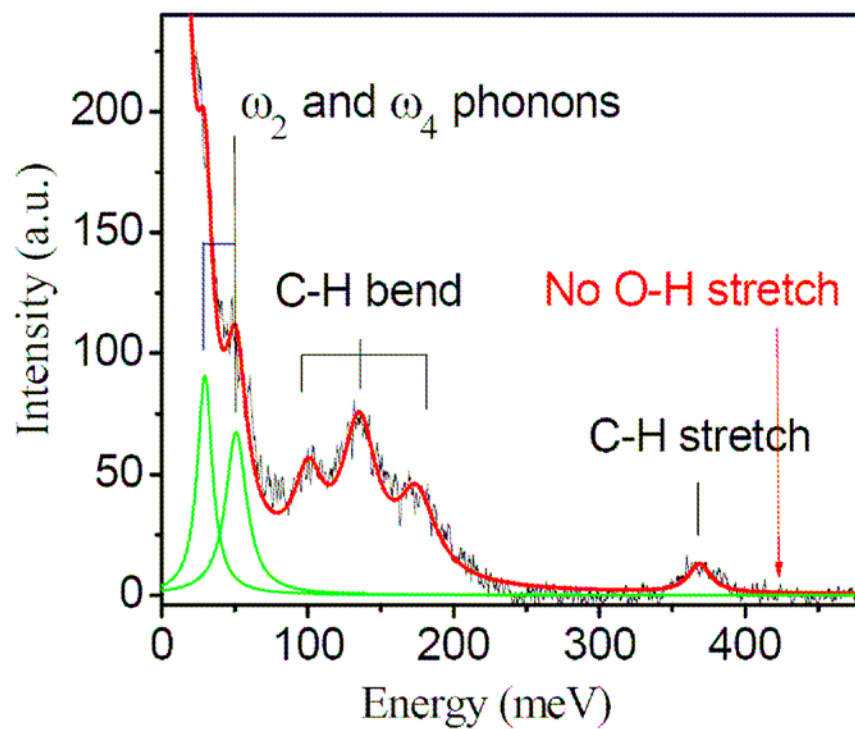


Figure 4.6: HREELS experiment. Spectrum of an air-exposed SrRuO_3 thin film reveals hydrocarbon contamination.

attributable to C-H bending and stretching modes correspondingly. Hence, energy loss data points to the presence of hydrocarbon contaminants on the surface. However, simultaneous observation of phonon modes suggests that, in agreement with LEED data, the contamination density is fairly low (< 1 ML) and does not significantly disorder the surface.

The evolution of the chemical composition of the films and oxidation state of ruthenium and strontium during annealing were determined using XPS and Auger electron spectroscopy (AES) [Mg- $K\alpha$ source, pass energy 25 eV, double pass cylindrical mirror analyzer (CMA), Physical Electronics]. The system was calibrated to the 4f excitation at 84.1 eV of a Au standard. XPS spectra were acquired from the as-inserted sample and after each annealing to verify the chemical composition of the film. No titanium peaks are observed in XPS for annealing temperatures as high as 900 °C, indicating that the film is continuous and the substrate not exposed even at high temperatures. XPS spectra at room temperature were acquired in the energy ranges 524–540 eV, corresponding to the O 1s peak, at 454–474 eV corresponding to the Ru 3p_{3/2} peak, at 128–138 eV corresponding to the Sr 3d_{3/2} and 3d_{5/2} peaks, and 260–296 eV, which includes the Ru 3d_{3/2} and 3d_{5/2}, Sr 3p_{3/2} and 3p_{1/2}, and C 1s peaks.

The evolution of oxygen 1s core level with annealing temperatures is illustrated in [Figure 4.7\(a\)](#). For samples annealed at low temperatures, the peak is comprised of two well-separated components. In the intermediate temperatures range, 400–700 °C, the second component becomes less pronounced. However, for samples annealed at highest temperatures 800–900 °C the second component is again visible. O 1s peaks were corrected using Shirley background subtraction [\[127\]](#) and fitted using two Gaussian

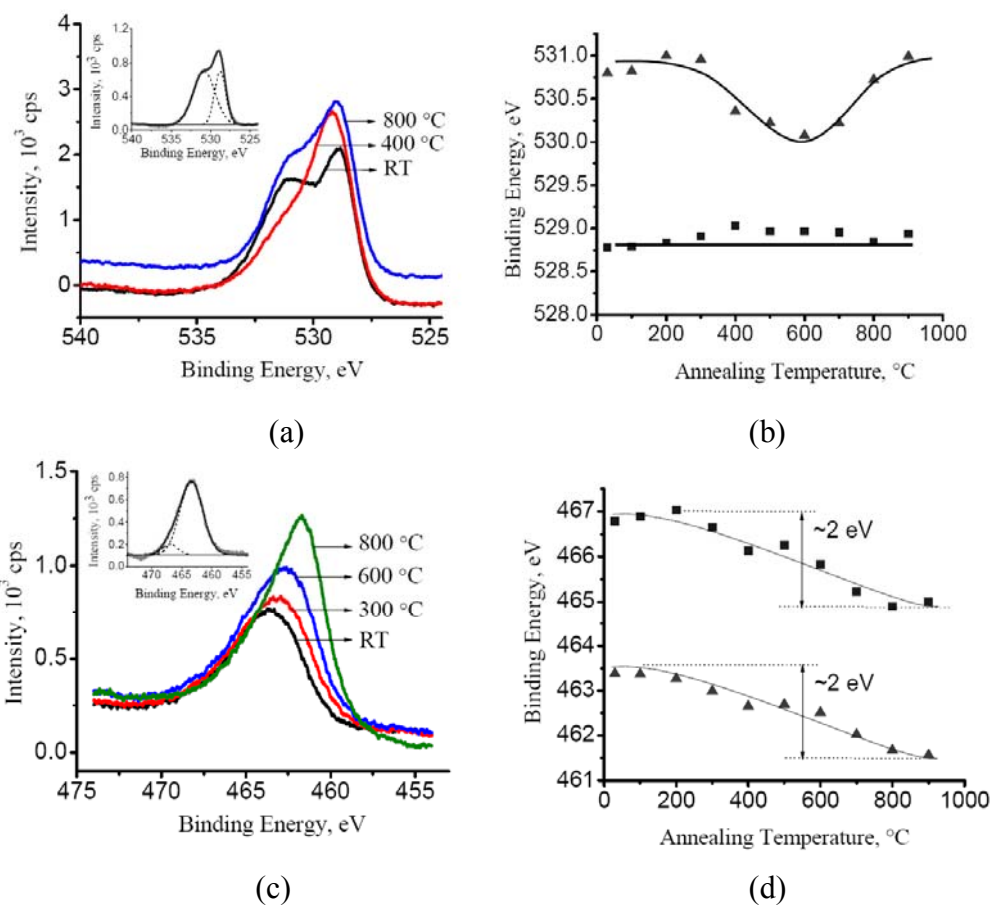


Figure 4.7: XPS analysis for O and Ru spectra. (a) O 1s XPS spectra from a SrRuO₃ film at RT (Black line) and annealed at 400 °C (Red line) and 800 °C (Blue line). (b) The temperature dependence for the O 1s centroid. (c) Ruthenium 3 $p_{3/2}$ XPS spectra for different annealing temperatures: RT (Black line), 300 °C (Red line), 600 °C (Blue line), and 800 °C (Green line). (d) The temperature dependence for the Ru 3 $p_{3/2}$ centroid.

components of characteristic width 1.5 and 3.2 eV correspondingly with the resulting fit illustrated in the inset of [Figure 4.7\(a\)](#). The widths of the Gaussian components do not change appreciably during the heating. The position of the first peak at 528.7 eV is also independent of annealing temperature. At the same time, the second peak shifts from 531 eV at RT to a value of 530 eV at 400–700 °C, and shifts back to 531 eV for temperatures 800 °C and higher. The dependence of annealing temperature for the O 1s centroid is illustrated in [Figure 4.7\(b\)](#). Noteworthy is that the temperature dependence of the peak position is non-monotonic and two distinct regions can be clearly seen.

Thermal behavior of ruthenium $3p_{3/2}$ core levels for different annealing temperatures is illustrated in [Figure 4.7\(c\)](#). The peaks are asymmetric, indicating the presence of chemically non-equivalent Ru atoms or, alternatively, shake-up lines or multiplet splitting in metallic SrRuO₃ [128]. After the Shirley background subtraction, the peaks were fitted by two Gaussians. Fitting using a Doniach-Sunjic line shape, expected for materials with broad electron-hole life time distributions, was unsuccessful. Binding energies for two Gaussian components as a function of temperature are shown in the inset of [Figure 4.7\(c\)](#). Note that the separation between individual components is virtually temperature independent, thus suggesting that the satellite should be attributed to a shake-up line or multiplet splitting. The latter explanation is consistent with a ferromagnetic material; SrRuO₃ is ferromagnetic with an ordering temperature $T_c = 160$ K. Even in the paramagnetic state, above T_c , short range ferromagnetic correlations lead to core level splitting. The temperature dependence of the Ru $3p_{3/2}$ centroid is shown in [Figure 4.7\(d\)](#). Here the average binding energy changes monotonically with temperature, with the binding energy decrease of ~2 eV between RT and 800 °C. The binding energy

for the Ru $3p_{3/2}$ after high temperature annealing, 461.5 eV, is close to that of metallic Ru, 462 eV [129]. The decrease of the binding energy can be interpreted as a complete or almost complete reduction of Ru oxide to Ru metal. Strontium $3d_{3/2}$ and $3d_{5/2}$ core levels after annealing are illustrated in Figure 4.8(a). The splitting between the components of the $3d$ peak is small ($\Delta = 1.79$ eV) and is comparable to the instrumental resolution and intrinsic peak width, thus precluding reliable separation of the two components. After the Shirley background subtraction, the peaks were fitted using Gaussian or Doniach-Sunjic line shapes. Fits using a single pair of Gaussians or two pairs of Gaussians with the imposed center difference and area ratio constraints were unsuccessful. Instead, we will analyze the centroid of the Sr $3d$ peaks, as shown in Figure 4.8(b). At room temperature, the centroid value of 133.4 eV is comparable to the Sr $3d_{5/2}$ binding energies in ternary oxides with similar transition metals (~ 133 eV in SrRh_2O_4 and ~ 133.5 eV in SrMoO_4) [129]. The chemical environment of Sr starts to change significantly above 300 °C and the centroid binding energies for Sr increase from 133.4 eV at RT to 133.7 eV at 900 °C. The observed chemical shift for Sr of 0.3 eV in the reduction process is much smaller than expected for the formation of SrO , which would require a ~ 2 eV chemical shift to 135.3 eV [129]. Instead, this behavior is indicative of formation of Sr-rich ruthenates at 300–500 °C. This is consistent with thermal desorption spectroscopy, which shows that SrO species are volatile and leave the surface. Due to the volatile property of SrO at 300–500 °C, Sr-rich ruthenates are remained on the surface instead of SrO species.

The thermal evolution of XPS spectra in the 260–296 eV range for different annealing temperatures is illustrated in Figure 4.8(c). The characteristic doublets corresponding to Ru $3d_{3/2}$ and $3d_{5/2}$ transitions (281.4 and 285.5 eV) and Sr $3p_{1/2}$ and

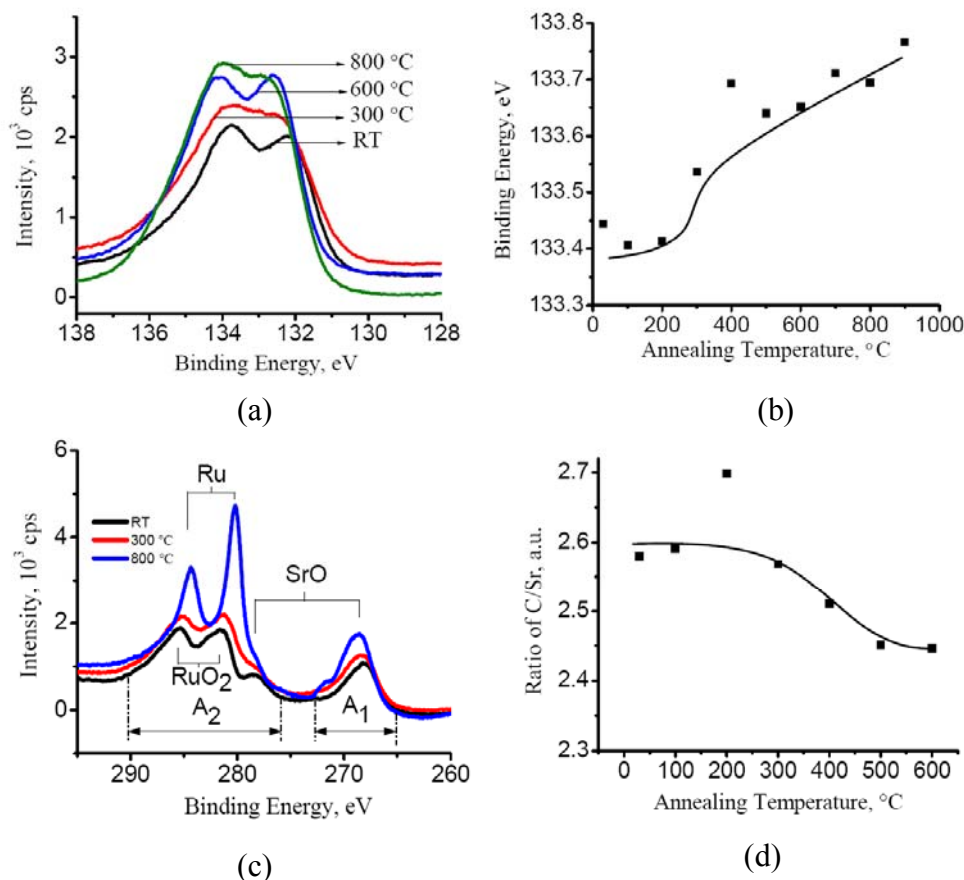


Figure 4.8: XPS analysis for Sr. (a) Strontium $3d_{3/2}$ and $3d_{5/2}$ XPS spectra for different annealing temperatures: RT (Black line), 300 °C (Red line), 600 °C (Blue line), and 800 °C (Green line). (b) The temperature dependence for the Sr 3d centroid. (c) XPS spectra in the 260-296 eV range for different annealing temperatures: RT (Black line), 300 °C (Red line), and 800 °C (Blue line). A₁ is amount of the area of Sr $3p_{1/2}$ peak and A₂ is amount of the area of Sr $3p_{3/2}$, Ru $3d_{3/2}$ and $3d_{5/2}$ and C 1s peaks. (d) The approximate ratio of C/Sr as a function of annealing temperature.

$3p_{3/2}$ (268.1 and 278.4 eV) are clearly seen. Overlapping these is the carbon $1s$ peak (284.5 eV), making detection of carbon-containing species difficult; a similar overlap exists in AES as well (not shown). Due to the presence of multiple peaks and non-Gaussian peak shapes (compare Sr $3d_{3/2}$ and $3d_{5/2}$ and Ru $3p_{3/2}$), quantitative analysis of the XPS data in this energy interval is difficult; however, qualitatively thermal evolution of the spectrum is consistent with other core levels shown in [Figures 4.7 and 4.8](#). The Sr peaks shift towards larger binding energies by $\sim 0.3\text{--}0.6$ eV, whereas Ru peaks shift smaller binding energies by 2 eV.

The change of the surface chemical composition during annealing was also determined from the relative intensities of the Sr $3d$ /O $1s$, Ru $3p_{3/2}$ /O $1s$, and Sr $3d$ /Ru $3p_{3/2}$ XPS peaks. The Sr/O ratio was calculated from the integrated intensities of Sr $3d$ and O $1s$, the Ru/O ratio from Ru $3p_{3/2}$ and O $1s$ and the Sr/Ru ratio estimated from Sr $3d$ and Ru $3p_{3/2}$. The temperature dependence of intensity ratios is shown in [Figure 4.9](#). Noteworthy is that the Sr/Ru ratio is virtually independent of annealing temperature, so that although both SrO and Ru species are observed in TDS data [[Figure 4.5](#)], the total desorbed is small and the remaining ratio constant. At the same time, Sr/O and Ru/O ratios increase with temperature by a factor of 1.5. The dependences of annealing temperature for these two ratios are virtually identical, consistent with a constant value of the Sr/Ru ratio. For the initial stoichiometry of SrRuO $_3$, these ratios correspond to a final chemical composition of Sr:Ru:O = 1:1:2. This is consistent with the formation of a mixture of metallic Ru and a strontium-rich ruthenate with a stoichiometry of Sr $_2$ RuO $_4$. Formation of Sr $_2$ RuO $_4$ after reduction is in accord with thermodynamic arguments developed in [Section 4.2](#) and with the small binding energy shifts for Sr. Moreover, the

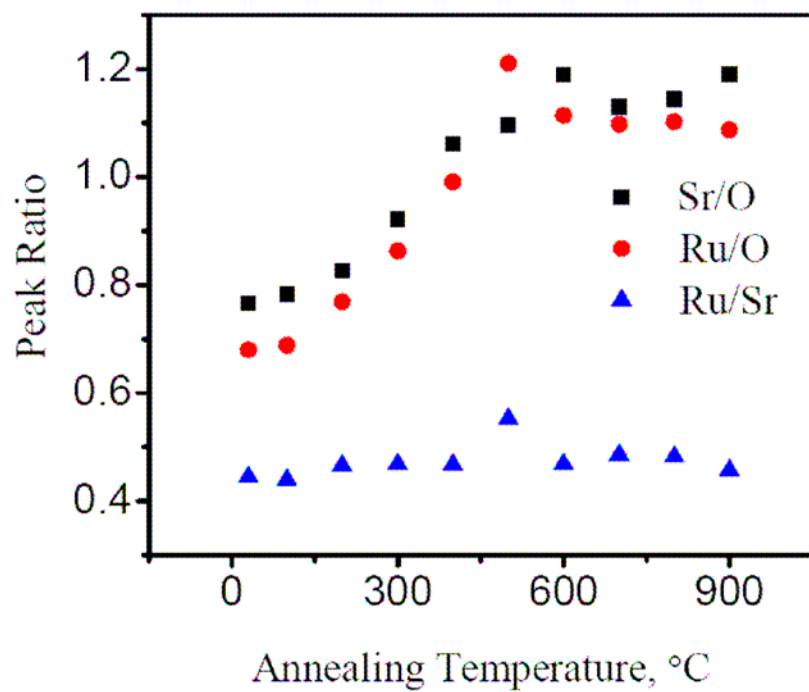


Figure 4.9: Intensity ratios from XPS as a function of annealing temperature. This indicates oxygen loss consistent with formation of metallic Ru and Sr_2RuO_4 particles.

STM images suggest that the particles forming on the surface are conductive, which will not be the case for the formation of wide band gap SrO.

To estimate the evolution of the carbon containing species, the XPS spectra in the range 260–296 eV were fitted by 6 Gaussian peaks [Figure 4.8(c)]. One of the peaks corresponding to Sr $3p_{1/2}$ at 268 eV (area A_1) can be clearly distinguished from the broad peak that comprises contributions from Sr $3p_{3/2}$, Ru $3d_{3/2}$ and $3d_{5/2}$ and C $1s$ (area A_2). From the spin-orbital splitting rules, the areas of Sr $3p_{1/2}$ and $3p_{3/2}$ peaks correspond as 1:2. Since the Sr/Ru ratio is constant, the C/Sr ratio can be estimated as $(A_2 - A_1/2)/A_1$, where $A_2 - A_1/2$ corresponds to total amount of the areas of [C $1s$ + Ru $3d_{3/2}$ + Ru $3d_{5/2}$] peaks and A_1 corresponds to amount of the area of Sr peak. Note that the amount of carbon thus determined is almost constant below 300 °C, decreases between 300 °C and 500 °C and saturates at ~ 500 °C [Figure 4.8(d)]. At higher temperatures, due to significant changes in the Sr peak shape, the scatter of the data increases. Despite the large uncertainties related to the background subtraction and non-Gaussian peak shape, these results suggest that hydrocarbons are present on the surface at temperatures up to 300 °C and desorb in the interval 300-500 °C, in agreement with STM, HREELS, and XPS data.

4.3.5 RHEED patterns before and after cleaning SrRuO₃ films

Electron diffraction was employed to survey the surface crystallinity of SrRuO₃ thin films during annealing and to explore potential methods to remove hydrocarbon contaminants. While LEED primarily explores the first surface layer, RHEED can

penetrate to several cells due to a greater mean free path. RHEED [high-pressure RHEED, double differential pumping, Staib Instruments, Inc.] patterns were recorded during annealing for 10 minutes in 100 °C intervals up to 700 °C. RHEED patterns were recorded for three environments: (1) in high vacuum ($\sim 1 \times 10^{-7}$ Torr) after air exposure, (2) in high oxygen/ozone pressure (~ 10 mTorr, $\sim 7\%$ ozone), and (3) in high vacuum ($\sim 1 \times 10^{-7}$ Torr) after an oxygen/ozone exposure. The thermal evolution of air-exposed SrRuO₃ surface in high vacuum is shown in Figure 4.10(a) from RT to 700 °C. The RHEED pattern at RT shown in Figure 4.10(a) shows a bright specular spot, well-defined diffraction spots, and well-developed Kikuchi lines, confirming a very flat crystalline surface structure. Additional diffraction spots become visible after annealing to 300 °C, consistent with the onset of surface decomposition seen with other techniques. Above 600 °C, the RHEED pattern clearly exhibits new well-defined diffraction spots that become more pronounced with temperature 700 °C. The appearance of new diffuse diffraction pattern can be correlated with the formation of spherical particles observed by STM for the high-vacuum annealing of air-exposed SrRuO₃.

To attempt to counteract decomposition due to hydrocarbon contaminants on the film surface, a second air-exposed sample was annealed to 700 °C in a high pressure oxygen/ozone environment (~ 10 mTorr, $\sim 7\%$ ozone). The RHEED patterns were recorded during annealing from RT to 700 °C at every 100 °C [Figure 4.10(b)]. Note the difference between RHEED patterns at 300 °C in high vacuum and oxygen/ozone and the absence of new diffraction spots on the latter. The RHEED pattern at RT after annealing is similar to the pattern before annealing [*RT* pattern and *RT after 700 °C* pattern in Figure 4.10(b)] and still shows bright specular and diffraction spots. Compared

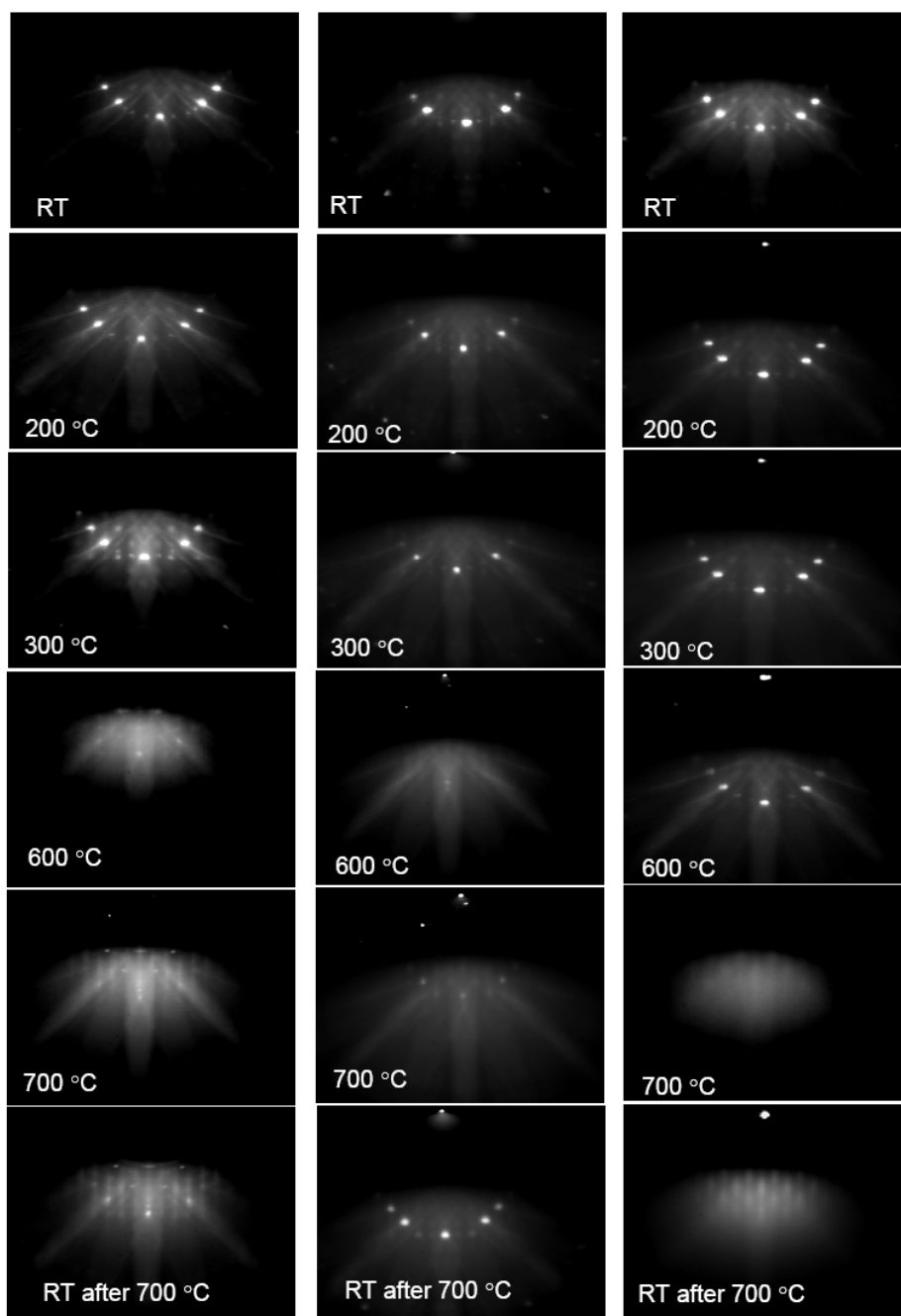


Figure 4.10: RHEED patterns of air-exposed SrRuO₃ films at different temperatures. Images were taken (a) in high vacuum ($\sim 1 \times 10^{-7}$ Torr), (b) in high O₂/O₃ pressure (~ 10 mTorr, $\sim 7\%$ ozone), and (c) in high vacuum ($\sim 1 \times 10^{-7}$ Torr) after annealing in O₂/O₃.

to the RHEED pattern (*RT after 700 °C*) in [Figure 4.10\(a\)](#), the surface crystallinity of SrRuO₃ films was not compromised during the presence of high pressure oxygen/ozone.

We suggest that heating in either oxygen or oxygen/ozone removes the effect of surface hydrocarbons, producing a more stable surface even in vacuum. To verify this, the surface stability of a SrRuO₃ sample in high vacuum was studied with RHEED after the oxygen/ozone treatment. After annealing to 700 °C and cooling to 30 °C in high pressure oxygen/ozone (10 mTorr, ~7% ozone), the sample was again annealed, this time in high vacuum ($\sim 1 \times 10^{-7}$ Torr) without intermediate exposure to atmospheric air. As a result, shown in [Figure 4.10\(c\)](#), the bright specular spots and diffraction spots were observed up to 600 °C without change of pattern in the medium temperature range (300–600 °C). This is significantly different from the behavior observed for the air-exposed sample in [Figure 4.10\(a\)](#). The lack of decomposition for the oxygen cleaned surface of SrRuO₃ provides additional evidence that hydrocarbon contaminants are the primary cause of surface instability at moderate temperatures. At the highest temperatures, around 700 °C, discontinuous spots appeared after 10 minutes annealing, but the specular intensity disappeared at the same time [*700 °C* pattern and *RT after 700 °C* pattern in [Figure 4.10\(c\)](#)]. This is different from the diffuse sample patterns [*700 °C* pattern and *RT after 700 °C* pattern in [Figure 4.10\(a\)](#)] and indicates that at least several layers (not top 1–2 layers) were destroyed, indicative of the onset of bulk decomposition.

4.4 Discussion

A consistent picture of the stability and thermal behavior of epitaxial SrRuO_3 thin films emerges from an array of surface probes including STM, HREELS, TDS, XPS, and RHEED. Figure 4.11 schematically shows models of the SrRuO_3 surface evolution after exposure to air then annealed in high vacuum [Figure 4.11(a)], in oxygen/ozone [Figure 4.11(b)], and in high vacuum after oxygen/ozone cleaning [Figure 4.11(c)].

As illustrated in Figure 4.11(a) hydrocarbon contaminants are present on the air-exposed surface of SrO-terminated SrRuO_3 films at room temperature, as confirmed by HREELS. The contamination density is fairly low (< 1 ML) and the surface is very flat and highly crystalline, [AFM and LEED]. After annealing to moderate temperatures (300–500 °C), the hydrocarbon contaminants induce local reduction of the SrRuO_3 surface and lead to formation of irregular pits, as observed in STM images. This process is associated with desorption of small amounts of SrO, Ru, CO_2 , and O_2 [TDS]. The RHEED patterns indicate the onset of a new phase at this temperature. Analysis of XPS data suggests that carbon contaminants are completely oxidized above this temperature. Due to the low density of contaminants, the surface decomposition results in a formation of a high defect density top layer [300–500 °C in Figure 4.11(a)], which can further decompose at higher temperatures. At higher temperatures [600–700 °C in Figure 4.11(a)] this stage is associated with the formation of new phases seen in RHEED patterns and by somewhat spherical particles in STM images which by XPS can be identified as Ru^0 and Sr_2RuO_4 [see also Section 4.2]. This surface decomposition process is limited to the high defect density top layer, as evidenced by the clearly seen step edges

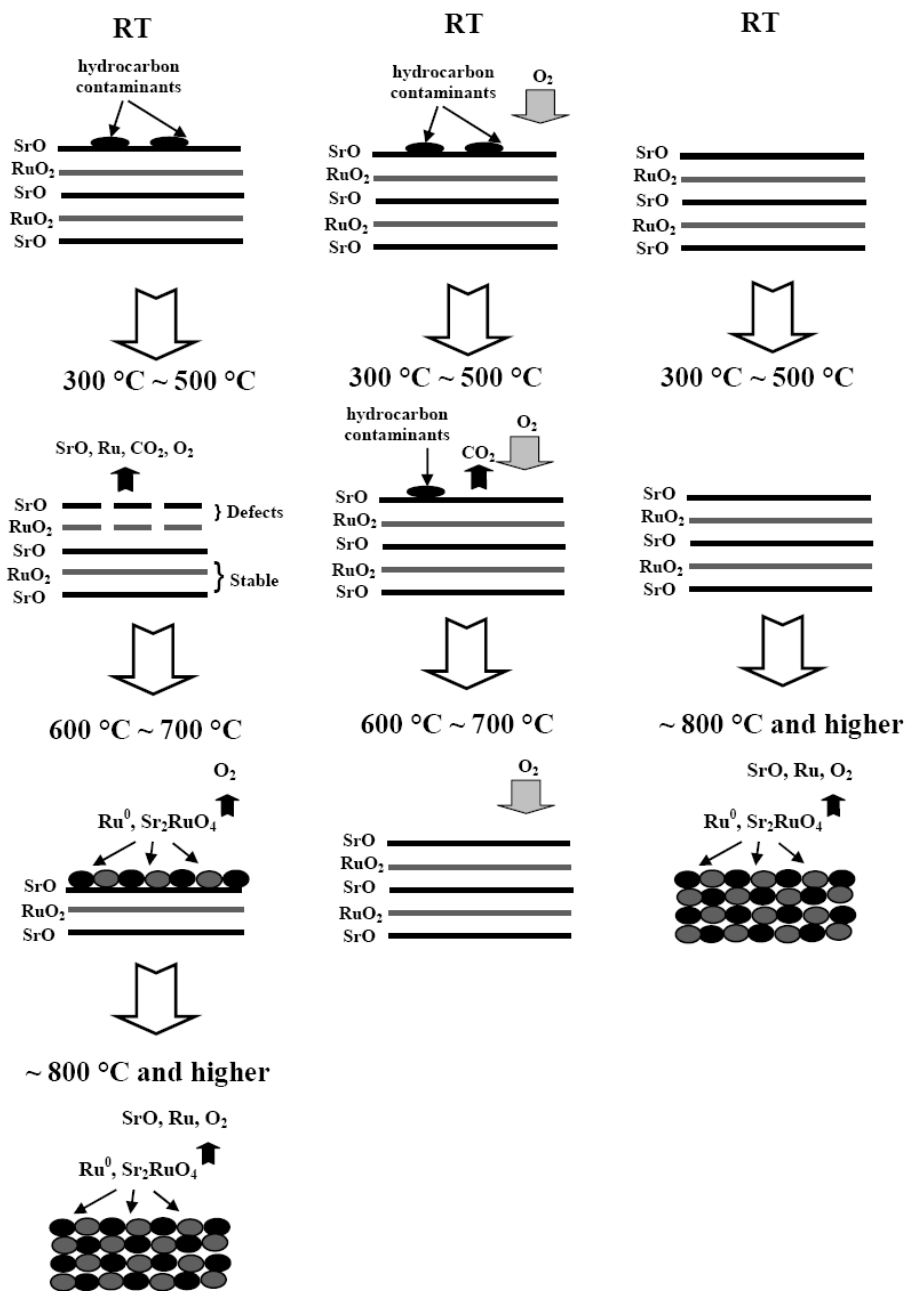


Figure 4.11: Schematics of possible surface configurations. These correspond at room temperature and after annealing to 300–500 °C and 600–700 °C for air-exposed SrRuO₃ films (a) in high vacuum (below 10⁻⁷ Torr), (b) in high O₂/O₃ pressure (~10 mTorr, ~7% ozone), and (c) in high vacuum (below 10⁻⁷ Torr) after annealing in O₂/O₃.

in the STM image and by lack of a Ti substrate signal in the XPS spectra; the relative size of the decomposition product particles increases with the annealing temperature, as can be seen in STM images and sharpening of the RHEED spots in [Figure 4.10\(a\)](#). Finally, annealing at even higher temperatures for several minutes corresponds to the bulk decomposition of the SrRuO_3 film, as evidenced by formation of large particles and appearance of Ti in XPS.

High pressure oxygen/ozone annealing results in qualitatively different evolution of surface structure and chemistry. Shown schematically in [Figure 4.11\(b\)](#) (RT) are the conditions of the surface before annealing. During annealing up to 300 °C, hydrocarbon contaminants were removed without destroying the surface [300–500 °C in [Figure 4.11\(b\)](#)], as confirmed by RHEED. RHEED patterns at RT after annealing to 700 °C in [Figure 4.10\(b\)](#) suggest the surface of films is cleaned and without decomposition [600–700 °C in [Figure 4.11\(b\)](#)].

Finally, the schematic in [Figure 4.11\(c\)](#) illustrates the thermal evolution of an oxygen-cleaned surface during annealing in high vacuum. Annealing in oxygen removes hydrocarbon contaminants and no decomposition is observed in medium temperatures [RHEED]. The onset of bulk decomposition is dependent on annealing temperature and times and occurs quickly above ~800 °C, or above ~700 °C for extended times.

4.5 Conclusions

The surface stability of epitaxial SrRuO_3 thin films has been shown as a function of temperature at different phases (air-exposed and cleaned phases), which is markedly

different from the bulk. Air-exposed samples are shown to have a partial layer of hydrocarbon contamination. These hydrocarbons are a destabilizing force, reducing the surface at relatively low temperatures ~ 300 °C in vacuum. This leads to a decomposition of the surface layer accompanied by desorption of SrO and metallic Ru and the formation of one or two layer deep pits. At higher temperatures, above 500 °C, the remaining surface material forms nanoparticles of Sr-rich ruthenates and metallic Ru. The onset of bulk decomposition occurs at much higher temperatures, above ~ 700 °C, in agreement with results of thermodynamic analysis.

Hydrocarbons can be oxidized and removed by annealing the SrRuO₃ film in 10 mTorr of oxygen/ozone. Subsequently, films annealed in vacuum are stable to much higher temperatures than those without treatment, surviving to ~ 600 °C. Above this temperature, the entire film begins to decompose. The films are further stabilized by an oxidizing atmosphere. In 10 mTorr of oxygen/ozone, no structural decomposition is observed below ~ 700 °C.

We conclude that SrRuO₃ films grown on SrTiO₃ by PLD can remain very flat and highly crystalline after exposure to air. However, contamination leads to surface decomposition at elevated temperature unless first removed. Clean SrRuO₃ surfaces are more thermodynamically stable, but can still be reduced in vacuum. This behavior highlights the need for careful, in-situ, growth and characterization even of oxide surfaces which appear to be chemically stable.

Chapter 5

Crystal structure of thin films: *in-situ* analysis

In this chapter, our attention is focused on the study of the surface structure of epitaxial oxide thin films. As shown in the previous chapter, air-exposed samples are shown to have a partial layer of contamination on the surface, which leads to a change in the physical properties of the surface. Under ambient conditions, we have also shown that the transport measurements are strongly affected by mobile surface charges due to humidity on the nanostructure [130]. For this reason, we explore atomic surface structure and electronic properties of *in-situ* grown films with STM and LEED in a UHV environment. First, the surface structure of SrRuO₃ thin films, served as an electrode, is investigated to understand the interface between conductive SrRuO₃ and ferroelectric BaTiO₃ films, which leads to a reconstruction in ultra-thin BaTiO₃ films. Next, the surface structure of ferroelectric BaTiO₃ films grown on SrRuO₃ films is studied to understand the ferroelectric properties in the surface layers of the strained film. Finally, we show the structure changes due to adsorbates by comparing *in-situ* LEED IV spectra of BaTiO₃ films with and without exposure in H₂O.

5.1 Epitaxial SrRuO₃ thin films: atomic structure and electronic properties

Conductive SrRuO₃ exhibits a variety of interesting physical phenomena due to the closeness of structural phase transition from cubic to orthorhombic phases, which in similar layered compounds triggers metal-insulator and magnetic phase transitions. Understanding the interface structure and properties of oxide heterostructures requires the knowledge of the atomic structure of SrRuO₃ prior to deposition of a second component. However, the perovskite structure of SrRuO₃ precludes surface preparation through cleaving, which produces atomically flat surfaces for layered ruthenates such as Sr₂RuO₄. We explored the previously unknown atomic surface structure and electronic properties of epitaxial SrRuO₃ thin films on (100) SrTiO₃ substrate grown by *in situ* STM and LEED.

The *ex-situ* AFM image in [Figure 3.5\(b\)](#) indicates high quality SrRuO₃ thin film with 15 nm thickness, which has atomically flat surface exhibiting only single unit-cell terrace steps. To study the atomic surface structure and electronic properties of this film, samples which were kept *in-situ* were annealed at 450 °C for 90 min in 1 Torr O₂ after growth and then cooled down to room temperature. After this treatment, the samples were transferred to the Omicron Variable temperature STM chamber without exposure in air. All STM images were acquired at room temperature with chemically etched W-tips in a UHV environment ($P = \sim 1 \times 10^{-10}$ Torr). As shown in [Figure 2.14](#), a bias voltage is applied to the tip and the sample is grounded through the clips and sample plate. Atomic

resolution *in-situ* STM images of SrRuO₃ films in [Figure 5.1\(a\)](#) demonstrate the atomic features with short range ordered atomic rows in (11) direction and large atomic defect density. Other STM images in [Figure 5.1\(b\)](#) were taken after annealing at higher temperature (650 °C) but maintaining annealing time and pressure. As shown in [Figure 5.1](#), after higher annealing temperatures, more ordering of atomic rows was observed, which suggests the film surface has high mobility. Surprisingly, despite of the mobility in the film surface, [Figure 5.2](#) shows a clear p(2x2) LEED pattern, indicating that the surface of films is still well-ordered and several possible crystal domain orientations of orthorhombic SrRuO₃ with (2x1) structure on cubic SrTiO₃ coexist in one thin film. This is consistent with the STM image in [Figure 5.1](#), which exhibits different crystal domain orientations (shown with arrows) of the films as described in [Section 1.2.3](#).

Due to SrO termination of SrRuO₃ films as discussed in [Section 3.2](#), it is most likely the Sr atoms that are imaged in our STM images. A high density of defects imaged as depressions (black) are also visible. As shown in [Figure 5.3](#), the depth of defects on the row is half unit-cell height (~0.15 nm), which suggests missing or removing the top layer atoms (Sr or SrO vacancies) on the surface. One unit-cell height (~0.36 nm) of defects on the surface is also observed randomly with relatively large size. Surprisingly, similar defects are also observed in cleaved Sr₂RuO₄ and Sr₃Ru₂O₇ crystal surfaces shown in [Figure 5.4](#). Using first-principles density functional theory (DFT)⁶, the observed atomic defects in Sr₂RuO₄ crystal were calculated to establish a structural model based on SrO, O and Sr vacancies of ruthenium oxides, which indicates that SrO vacancy can explain the defects observed in the STM image. The surface defects in

⁶ The DFT calculation was done by V. Meunier.

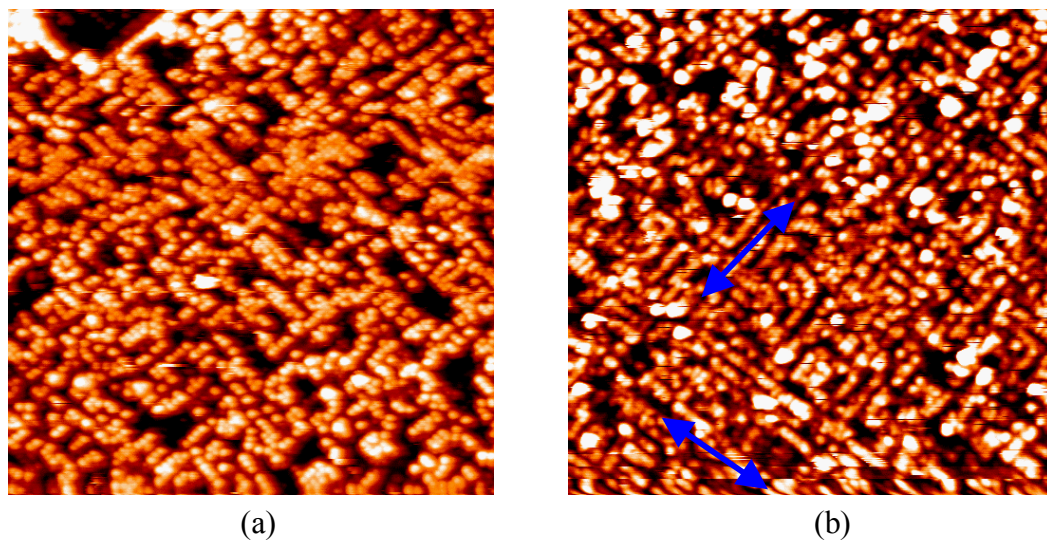


Figure 5.1: Atomically resolved STM images of SrRuO₃ films. The films were annealed at (a) 450 °C and (b) 650 °C in 1 torr O₂ for 90 min after growth (image size - 50x50 nm², -1.5 V_{gap}). All images were taken at RT.

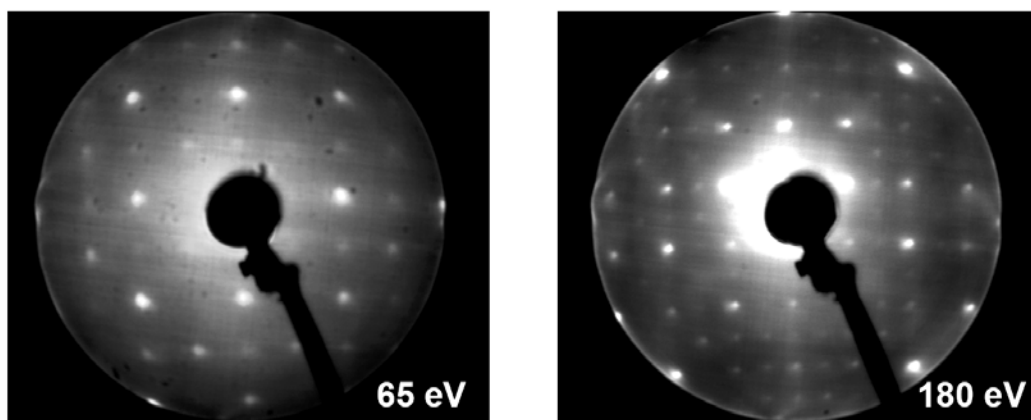


Figure 5.2: *In-situ* p(2x2) LEED images of SrRuO₃ films taken at RT.

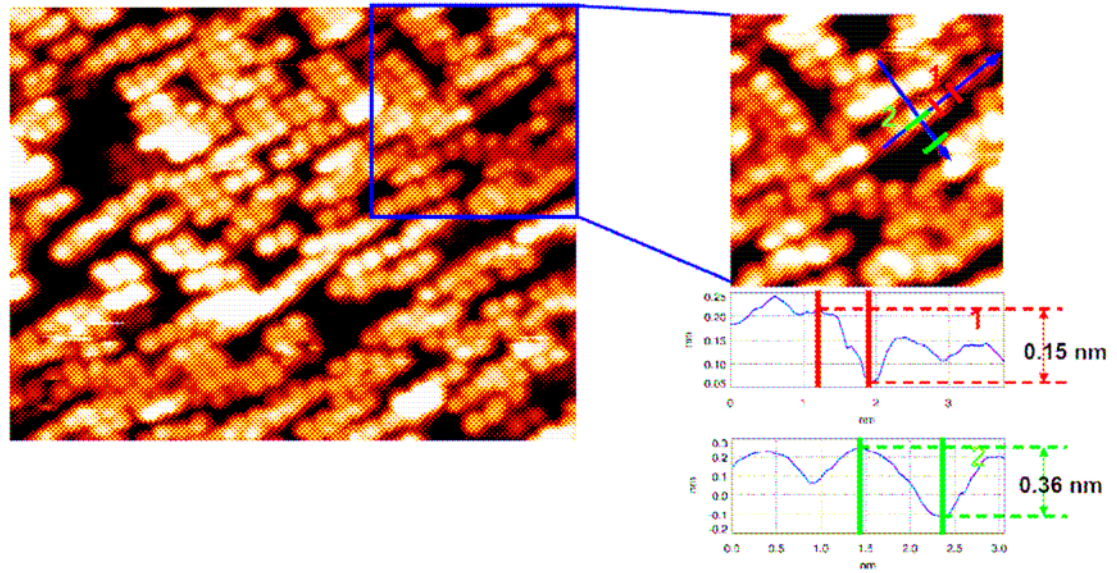


Figure 5.3: Line profile of surface defect on SrRuO₃ films. The sizes of left and right images are 25x20 nm² and 10 nm², respectively.

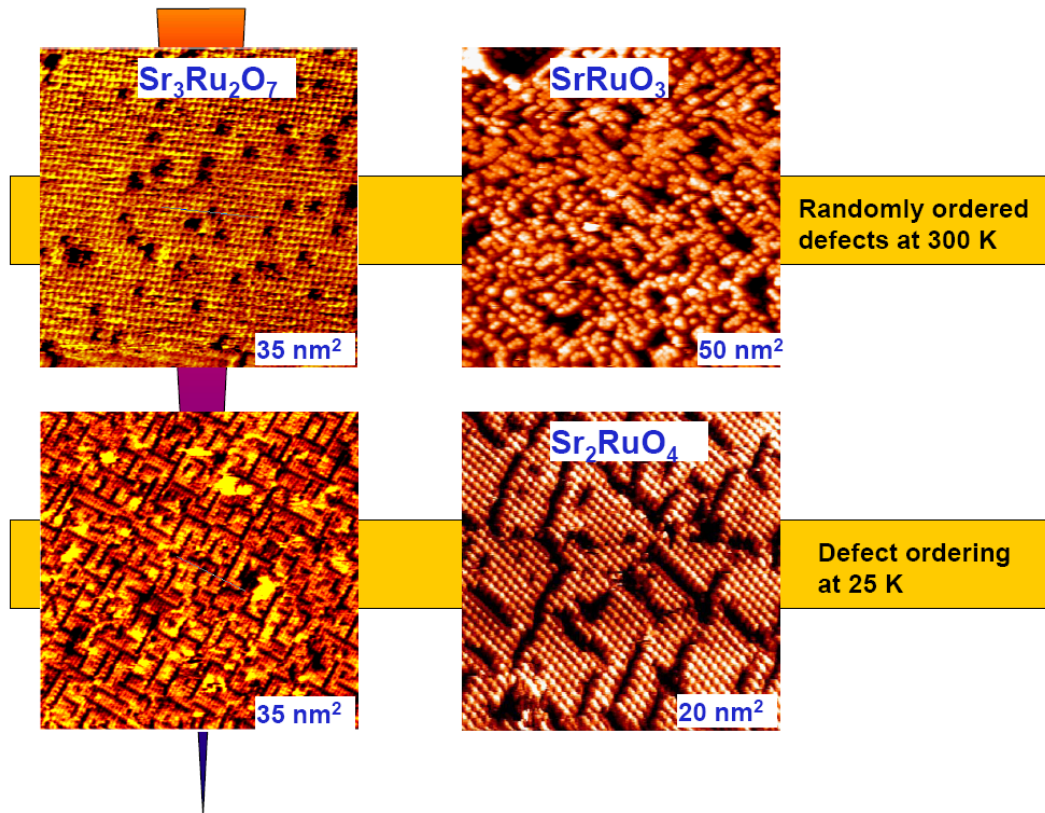


Figure 5.4: Surface defects in ruthenates [50,51].

SrRuO₃ films may be expected to come from SrO vacancies due to the similar shape of patterns. However, even at this point it is clear that these defects, unobservable on standard *ex-situ* AFM, will provide a profound effect on both the surface properties and on subsequent growth of TMOs on SrRuO₃ and are closely linked to the mechanism of oxide thin film growth.

As mentioned before, the randomly ordered defects on the surface of epitaxial SrRuO₃ films look very similar to those of cleaved Sr₂RuO₄ and Sr₃Ru₂O₇ crystals in [Figure 5.4](#). Randomly ordered defects are observed on the surfaces of SrRuO₃ and Sr₃Ru₂O₇ at room temperature [\[51\]](#). Upon lowering the temperature, the defects on Sr₃Ru₂O₇ start to align and be ordered by creating defect lines along the crystal axes [\[51\]](#). A recent study of Sr₂RuO₄ by STM shows that areas with ordered defects exist at low the temperature [\[131\]](#). Well-ordered defects shown to exist on the surface Sr₂RuO₄ and Sr₃Ru₂O₇ preferentially align along the crystal axes [\[50,51\]](#). However, the study of temperature dependence for SrRuO₃ as well as Sr₂RuO₄ is not detailed with regard to defect ordering. Epitaxial SrRuO₃ films may be expected to have well-ordered defects at the low temperatures similar to cleaved Sr₃Ru₂O₇ crystals, which may have significant influence on the transport and electronic properties of the surface of SrRuO₃ [\[55,56\]](#).

5.2 Epitaxial BaTiO₃/SrRuO₃/SrTiO₃ multilayers: polar structure in ultra-thin films

Ferroelectricity has long been viewed as a collective phenomenon and is expected to be strongly influenced by surfaces and finite-size effects [2], i.e., a different degree of ordering may occur near surfaces or interfaces, leading to an intrinsic dependence on sample size. As the dimensions of the perovskite layer decrease, the question of size dependence becomes crucial. Understanding the suppression of ferroelectricity in perovskite thin films is a fundamental issue that has remained unresolved for decades as described in Section 1.3. However, a direct experimental quantification of the ferroelectric polarization, particularly for films in the sub-10 nm thickness range is extremely difficult to measure because of extrinsic effects such as leakage current for the traditional P - E hysteresis loop. As a different approach to confirm ferroelectricity for this issue, we study the surface structure for polarization in ultra-thin (1 – 10 ML) BaTiO₃ films grown on SrRuO₃/SrTiO₃ by *in-situ* LEED-IV measurements.

5.2.1 The LEED experiment

For the LEED analysis, we use excellent structural quality, highly oxidized, and fully strained ultra-thin (≤ 10 ML) epitaxial BaTiO₃ films on SrRuO₃/SrTiO₃ grown by laser MBE as shown in Section 3.4. The bottom electrode SrRuO₃ films, connected to ground, were grown to prevent accumulating charges on BaTiO₃ films for LEED

measurements. After growth, samples were transferred from the growth chamber into the analysis chamber, where UHV conditions (2×10^{-10} Torr) were established, without exposure to air.

After the samples were introduced into the analysis chamber, they were positioned in front of the LEED optics and aligned to normal incidence. The sample holder was allowed to rotate and tilt the sample with (x,y,z) motions to adjust precisely the normal incidence condition, which was controlled by comparing the I(V) curves of symmetrically equivalent beams. After optimal adjustment, data were taken and recorded in energy steps of 1 eV with a high resolution 10 bit digital CCD camera, which is controlled by computer software (v 4.30) from KSA 400. I-V curves were extracted from digitized diffraction patterns by a locally written computer program [132] that provided the intensity in windows, which were positioned on equivalent beams and simultaneously monitored with increasing energy. All available equivalent beams, typical energy ranges of 50 – 500 eV, were collected, averaged, and normalized to the beam current.

For the structure refinement the Barbieri/Van Hove symmetrized automated tensor LEED (SATLEED) package [133] was used in order to fit theoretical I-V curves derived for different trial structures to the experimental data, which generates the lowest reliability factor. For the great part of LEED I-V studies of transition metal oxide surfaces, the reported values of R_p are significantly larger (0.40 – 0.60) [91]. Therefore, the SATLEED codes were modified to incorporate the energy dependence of the real part of the inner potential (V_{or}) [134]. The imaginary part of the potential (V_{oi}) equal to –6.0 eV was used in our calculation. The phase shifts have been obtained by an optimized muffin-tin (MT) potential, in which the spherical MT wells obtained by Mattheiss

prescription include preassigned surface core level shifts and are continuously connected with a flat interstitial potential [135]. Compared to empirical MT radii in typical metallic alloys [77,78], optimized MT radii in complex metal oxides should be considered because the charge transfer between metallic cations and oxygen anions could change the effective MT radii of the ionic chemical species. The detailed calculation methods of this new approach are described in Ref. [134].

5.2.2 The surface structure of ultra-thin BaTiO₃ films

5.2.2.1 The clean surface of BaTiO₃

Symmetry breaking by the surface of ferroelectric perovskites can give rise to a broad spectrum of interesting physical phenomena. The first principle calculations of (001) surface of the bulk BaTiO₃ for the case of in-plane polarization parallel to the surface suggests that the TiO₂-terminated surface has a small enhancement of the ferroelectricity near the surface whereas the BaO-terminated surface has a small reduction [136]. However, theoretical calculations for a polarization perpendicular to the surface have to deal with the additional problem of the correct electrical boundary conditions, which may lead to a suppression of ferroelectric distortion near the surface layers. Meyer and Vanderbilt [4] report that even thin layers near the surface can show a ferroelectric instability in the case of a vanishing internal electric field by applying external electric field. In this case, they considered the case of the tetragonal *c* axis

pointing perpendicular to the surface (z-direction) with the fully relaxed first three layers of BaO-termination surface shown in [Figure 5.5](#). Here, the “rumpling parameter η_i ” [\[4,136\]](#) is defined as the amplitude of the relative displacement between the metal and the oxygen ions: $[\delta_z (M_i) - \delta_z (O_i)]$, where δ_z is the relative displacement of atoms given as a fraction of the ideal unrelaxed structure. η_i is positive if the metal ions are below the oxygen atoms (downward layer dipole moment). Later, we will compare our experimental results with the rumpling parameters due to surface relaxation without external electric field and demonstrate the different phenomena for polarization rather than surface relaxation.

On the atomistic level, the perovskite surfaces can support structural reconstructions resulting in deviations from bulk stoichiometry. This broad spectrum of phenomena on ferroelectric surfaces necessitates experimental studies. However, experimental studies of perovskites surfaces are complicated by the presence of surface defects [\[137\]](#) due to sputtering and annealing process for clean surface, making it difficult to verify the surface stoichiometry. Intrinsic sensitivity of most perovskites surfaces towards contamination, combined with polarization induced reactivity for ferroelectrics, necessitates studies of surfaces under UHV conditions. Since the perovskite structure of BaTiO₃ cannot be cleaved or cleaned using traditional sputtering and annealing, it needs to be prepared by *in-situ* synthesis [\[3\]](#). In this section, we study the surface structure of the *in-situ* ultra-thin BaTiO₃ films epitaxially grown by laser MBE in a specially designed UHV system combining growth and characterization shown in [Section 2.1](#). Furthermore, the thickness of epitaxially grown thin films can be controllable, which means that this approach can easily show new behavior such as the

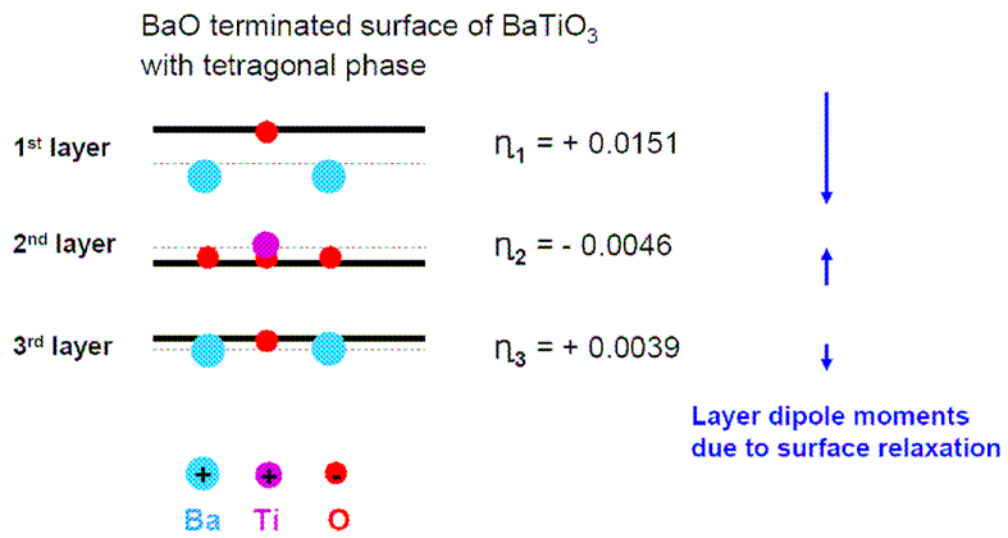


Figure 5.5: Schematics of the fully relaxed structure near the surface of BaTiO₃. Figures adapted from [4]. The rumpling parameters η_i are calculated using Ref. [136].

critical thickness, below which the ferroelectric phase disappears (detailed in [Section 1.3](#)). Here, we investigate the surface structure of ultra-thin BaTiO₃ films by LEED-IV experiments, through which we present experimental measurements of surface polar distortion on the ultra-thin BaTiO₃ films with 10 and 4 ML thickness.

Typical LEED patterns for 4 – 10 ML thin BaTiO₃ films, taken at sample temperature $T = 300$ K, are shown in [Figure 5.6](#). Very sharp (1x1) LEED patterns have been observed in all films at beam energies between 50 and 500 eV, which suggests that the surface of highly strained films still has $P4mm$ group symmetry with excellent structural condition. The observation of $P4mm$ group symmetry in LEED patterns indicates that the surface distortion should be restricted to a tetragonal polar distortion perpendicular to the surface without tilt or rotation of oxygen octahedra.

To determine the surface distortions, structure refinement was performed with restriction to the $P4mm$ group symmetry using the modified Barbieri/Van Hove SATLEED codes.⁷ As described in [Section 3.4](#), a very likely termination on the films is BaO as a top layer. To find out the best fit to the experiment I-V spectra, several possibilities were considered such as non-polarization, upward polarization, downward polarization, or domains with oppositely oriented polarization by shifting Ba, Ti, and O atoms.

Let us start with 10 ML thin BaTiO₃ films first. Experimental LEED I-V curves for these films exhibit as black lines in [Figure 5.7](#). To find the best fitted model to these experimental I-V curves, we have first searched in-plane and out-of-plane lattice parameters using 2 dimensional maps for R_p factor with two parameters shown in [Figure](#)

⁷ Theoretical spectra were calculated by V.B. Nascimento.

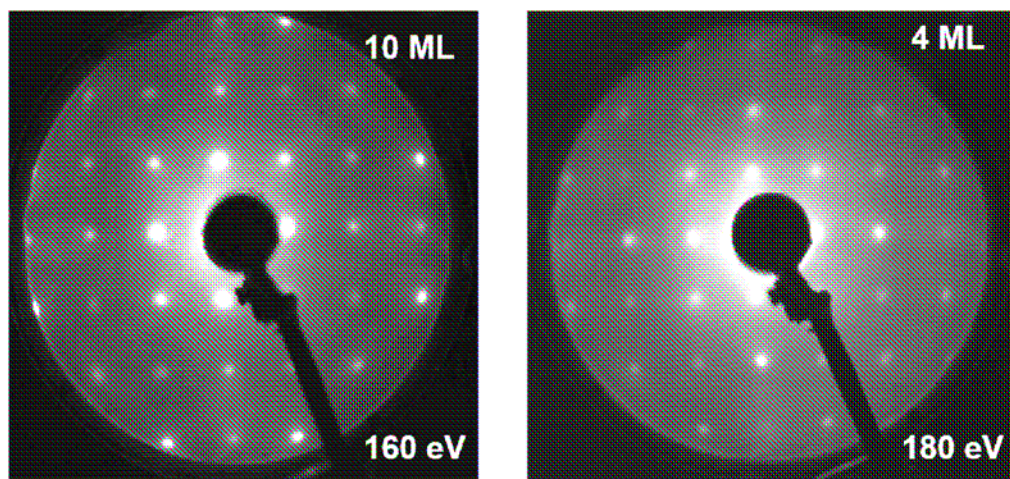


Figure 5.6: *In-situ* (1x1) LEED images of 10 and 4 ML thick BaTiO₃ films taken at RT.

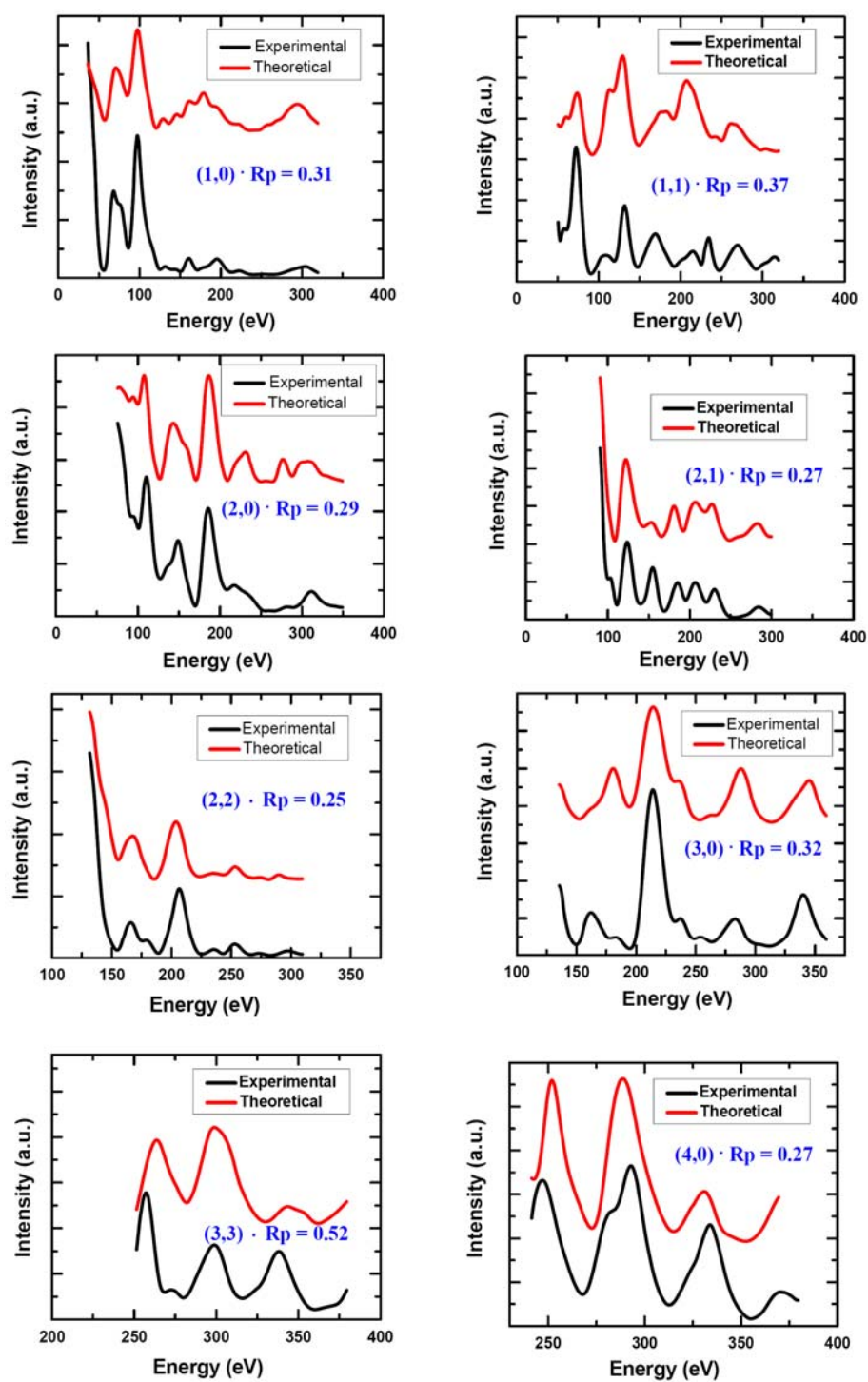


Figure 5.7: I-V curves of 10 ML BaTiO₃ films.

5.8. In the case of surface structure without polarization, the minimum of R_p factor is 0.45 at the lattice constants $a = 3.90 \text{ \AA}$ and $c = 4.10 \text{ \AA}$ [Figure 5.8(a)], which is too high to accept this model. To reduce the R_p factor, a polar structure is required to better fit the experimental spectra. An upward polar surface structure has the lowest R_p factor, which is reduced to 0.34 at $a = 3.91 \text{ \AA}$ and $c = 4.19 \text{ \AA}$ shown in R_p contour plot Figure 5.8(b), which was obtained through optimization of lattice parameter a and c . Therefore, we can conclude that the 10 ML thick BaTiO_3 films are fully strained with an upward surface polarization compared to bulk BaTiO_3 . After performing a lattice parameter grid search, the structures were optimized again for structural refinement search. Figure 5.9 and Table 5.1 show the detailed vertical displacements of each atom showing the upward polarization, and provide the final optimized R_p factor as 0.32 ± 0.04 , which is reliable for confidence in this structure. The error of 0.04 has been calculated using the Equation 2.19 shown in Section 2.3. The comparison between calculated (red) and experimental (black) I-V curves for this structure is presented in Figure 5.7.

Using this model with the best fit to the LEED I-V experimental data, we computed rumpling parameters η_i for each surface layer shown in the second column of Table 5.2. As defined before, the rumpling parameters are given by $\eta(\text{BaO}) = \delta_z(\text{Ba}) - \delta_z(\text{O}_{\text{top}})$ for a BaO plane and $\eta(\text{TiO}_2) = \delta_z(\text{Ti}) - \delta_z(\text{O}_{\text{plane}})$ for a TiO_2 plane, where δ_z are displacement associated with the ferroelectric instability as a fraction of optimized and unrelaxed lattice constant $c = 4.19 \text{ \AA}$. The rumpling parameters in the second column of Table 5.2 have negative signs, which indicate that all layer dipole moments in the surface of the film have upward direction. To compare the LEED I-V results with DFT calculation for surface layers of bulk, the theoretical rumpling parameters are shown in

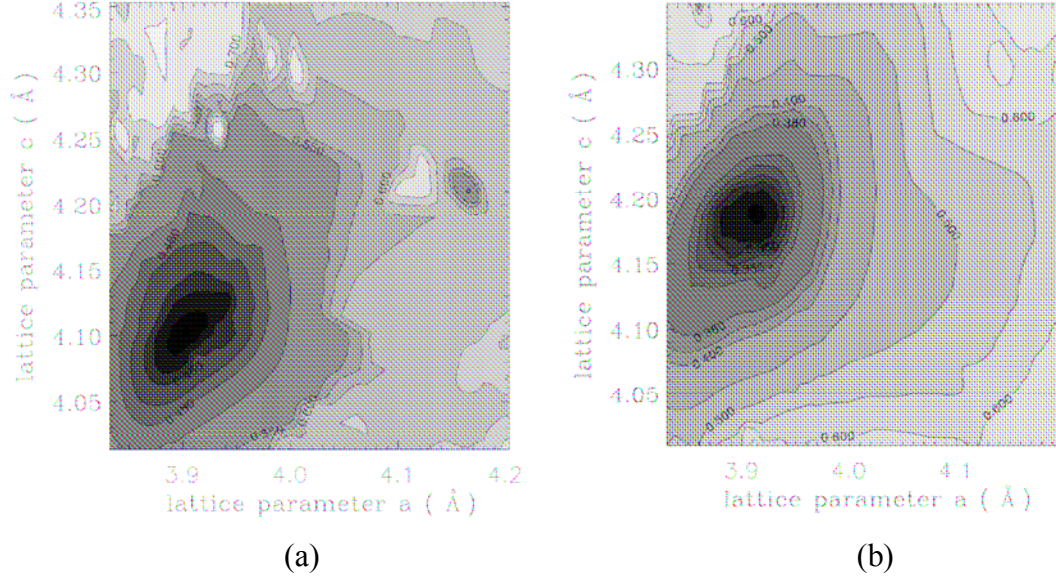


Figure 5.8: R_p contour plot for 10 ML BaTiO₃ films: (a) no polarization in sub-surface (minimum $R_p = 0.45$ at $a = 3.90$ Å and $c = 4.10$ Å) and (b) upward polarization in sub-surface (minimum $R_p = 0.34$ at $a = 3.91$ Å and $c = 4.19$ Å).

Upward polarization

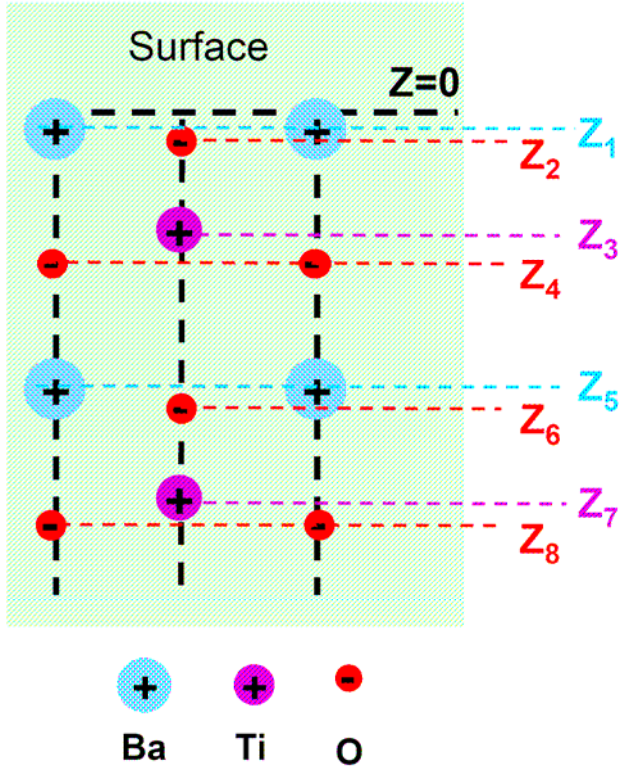


Figure 5.9: Final structure refinement for 10 ML BaTiO₃ films (final $R_p = 0.32$).

Table 5.1: Final structure refinement for 10 ML BaTiO₃ films (final $R_p = 0.32$).

Z_1	$0.0964 \pm 0.04 \text{ \AA}$
Z_2	$0.1185 \pm 0.04 \text{ \AA}$
Z_3	$1.9595 \pm 0.03 \text{ \AA}$
Z_4	$2.1169 \pm 0.05 \text{ \AA}$
Z_5	$4.1854 \pm 0.04 \text{ \AA}$
Z_6	$4.3029 \pm 0.07 \text{ \AA}$
Z_7	$6.1838 \pm 0.05 \text{ \AA}$
Z_8	$6.3039 \pm 0.09 \text{ \AA}$

Table 5.2: Rumpling parameters for 10 ML BaTiO₃ films.

layer	Surface of films	Surface of bulk in paraelectric phase*	Bulk
	LEED-IV exp.	DFT theory (only relaxation)	exp.**
1 st , $\eta(\text{BaO})$	- 0.0053 \pm 0.0191	+ 0.0151	\pm 0.0240
2 nd , $\eta(\text{TiO}_2)$	- 0.0376 \pm 0.0191	- 0.0046	\pm 0.0285
3 rd , $\eta(\text{BaO})$	- 0.0281 \pm 0.0262	+ 0.0039	\pm 0.0240
4 th , $\eta(\text{TiO}_2)$	- 0.0287 \pm 0.0334		\pm 0.0285

* Ref. [4] and [136].

** Ref [138].

the third column. However, in the theoretical calculation, an external electric field is applied to the surface of bulk BaTiO₃ with initially non-polar structure, which is different from the experimental strained films with the polar structure independent of an external electric field. So far, there is no theoretical information of the surface out-of-plane polar distortion in the surface layers independent of external electric field, which corresponds directly to our experimental LEED I-V results. The last columns of Table 5.2 give the bulk values for reference [4,136,138], which are smaller than the surface polar distortion in BaTiO₃ films. This demonstrates that the strained films have more enhanced polar distortions near the surface than the unstrained bulk. Except for the first layer of BaO (half unit cell), moderate values of upward layer dipole moments were observed in Table 5.2, which indicates that BaO terminated surface of the 10 ML thin BaTiO₃ films has upward polar structure in Figure 5.10.

Interestingly, LEED I-V parameters in Table 5.2 shows the reduced rumpling parameter in the top surface layer, which may not be expected in the surface layers of bulk BaTiO₃ [4]. As shown in Figure 5.5 (also fourth column of Table 5.2), theory

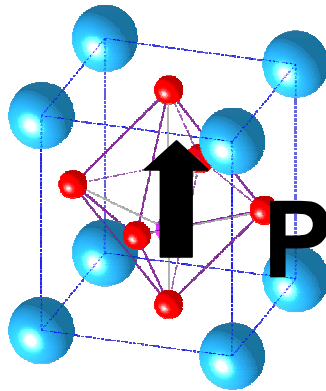


Figure 5.10: Polarization in 10 ML BaTiO₃ films.

predicts the surface of bulk BaTiO₃ is normally relaxed, which results in the appearance of a weak layer dipole moment near the surface even if the sample is in the paraelectric phase. Similar to the surface of bulk BaTiO₃, some relaxation should occur in the surface of epitaxial strained BaTiO₃ films. Figure 5.5 indicates that the first layer in BaO terminated surface of bulk BaTiO₃ has 4 times larger relaxation than other layers. This surface relaxation forms the downward layer dipole moment, which is the opposite direction of the upward enhanced polar structure in our strained films. Therefore, the surface relaxation leads to the reduced (4 ~ 7 times) rumpling parameter in the top surface layer of the BaO terminated strained films. The existence of a reduced top layer polarization is one of the evidences that the rumpling parameters in the surface layers of strained films come from the surface polar distortion as well as surface relaxation. If we take out the effect of surface relaxation from our measurement, the surface distortion in the top layer has a similar value to that of other layers. Therefore, we conclude that the reduced rumpling parameter in the top layer comes from the surface relaxation.

Experimental LEED I-V curves for 4 ML thin BaTiO₃ films are shown as black lines in Figure 5.11. To find the best fitted model to these experimental I-V curves, we have searched in plane and out of plane lattice parameters using 2 dimensional maps for R_p factor in Figure 5.12. R_p contour plot in Figure 5.12 shows that the optimized surface structure with upward polarization has the lowest R_p factor as 0.38 at $a = 3.91 \text{ \AA}$ and $c = 4.11 \text{ \AA}$. After performing this lattice parameter grid search, the structures were optimized again. Figure 5.13 and Table 5.3 show the detailed vertical displacements of the atoms in the surface layers after determined by the structure refinement. For the best fit, the final value $R_p \pm \Delta R_p$ is 0.30 ± 0.03 , which indicates that this upward polar structure in the

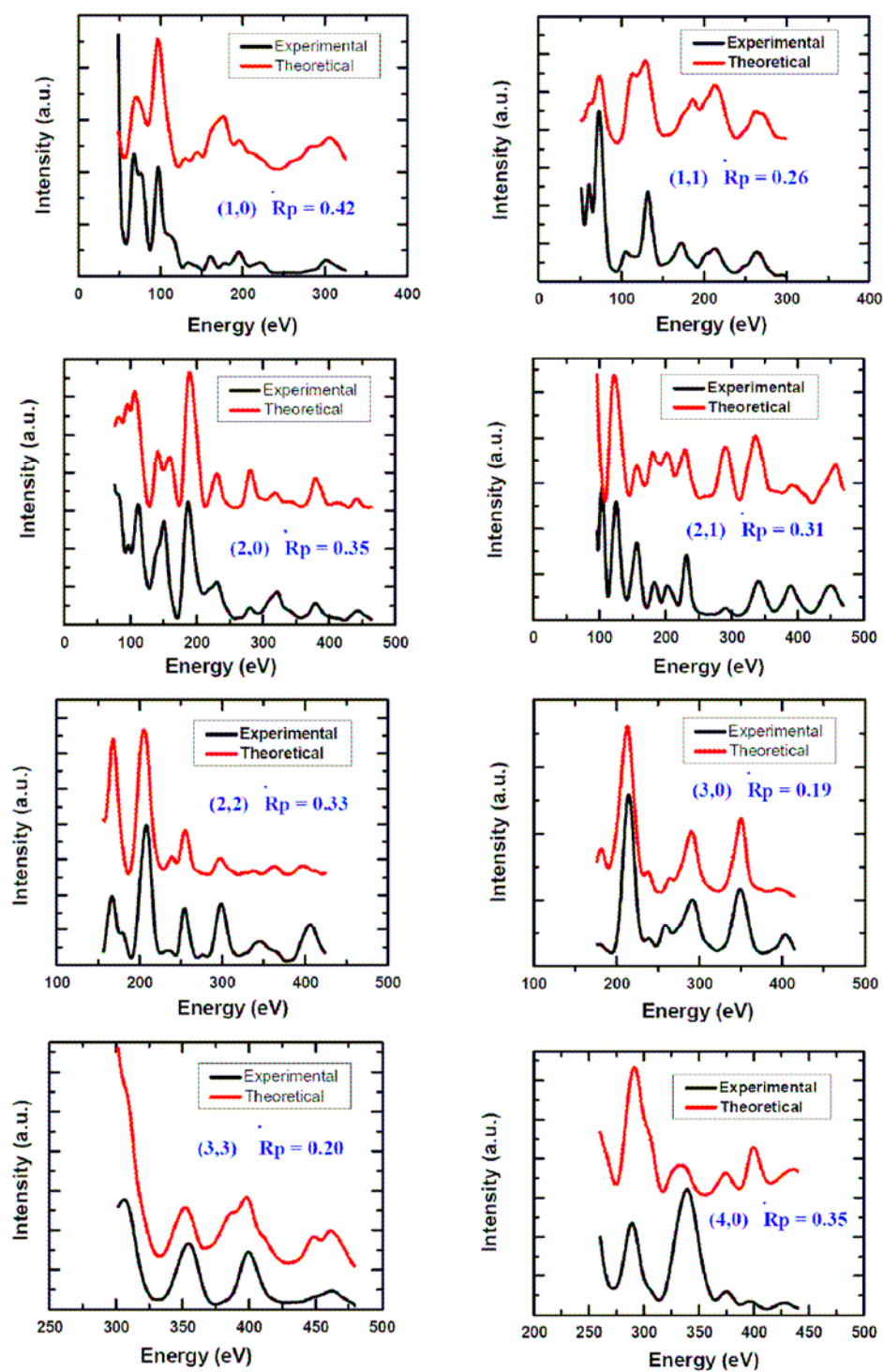


Figure 5.11: I-V curves of 4 ML BaTiO₃ films.

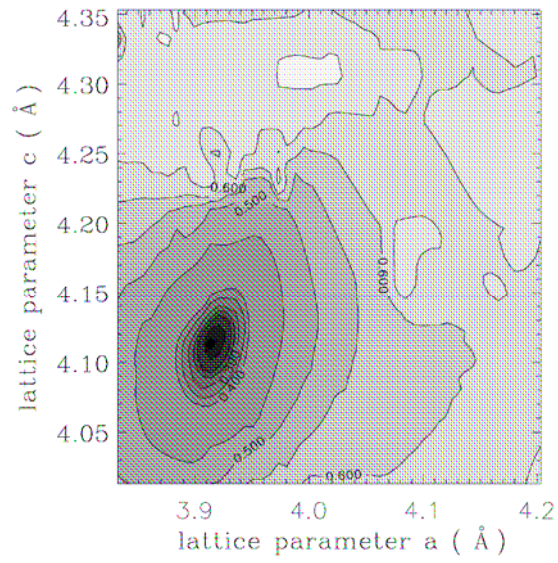


Figure 5.12: R_p contour plot for 4 ML BaTiO₃ films: upward polarization in sub-surface (minimum $R_p = 0.38$ at $a = 3.91$ Å and $c = 4.11$ Å).

Upward polarization

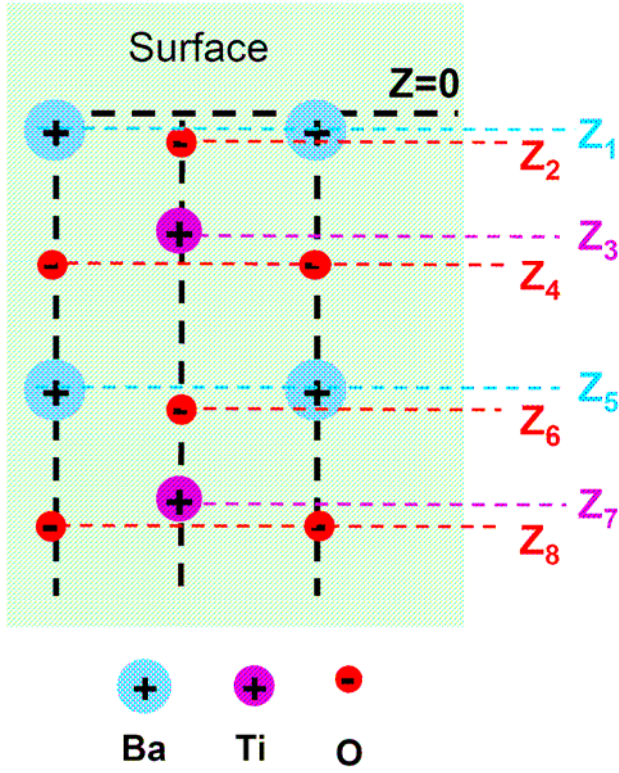


Figure 5.13: Final structure refinement for 4 ML BaTiO₃ films (final $R_p = 0.30$).

Table 5.3: Final structure refinement for 4 ML BaTiO₃ films (final $R_p = 0.30$).

Z_1	$0.0738 \pm 0.03 \text{ \AA}$
Z_2	$0.1078 \pm 0.04 \text{ \AA}$
Z_3	$1.9243 \pm 0.02 \text{ \AA}$
Z_4	$2.0648 \pm 0.05 \text{ \AA}$
Z_5	$4.1308 \pm 0.04 \text{ \AA}$
Z_6	$4.1863 \pm 0.07 \text{ \AA}$
Z_7	$6.0643 \pm 0.04 \text{ \AA}$
Z_8	$6.2046 \pm 0.10 \text{ \AA}$

surface layers is reliable. The comparison between calculated (red) and experimental (black) I-V curves for this structure is presented in [Figure 5.11](#). Similarly to 10 ML thin BaTiO₃ films, [Table 5.4](#) shows larger rumpling parameters in the surface layers of 4 ML thin BaTiO₃ films than that in bulk BaTiO₃ surface except for the top layer, which indicates an overall upward polar structure in [Figure 5.14](#).

Now, one of the fundamental questions for ferroelectric thin films can be asked if the reduced thickness of films affects the stability of the polar phase when the polarization has a component perpendicular to the film plane. The previous theoretical [\[25,42\]](#) and experimental [\[39\]](#) reports show that epitaxially grown BaTiO₃ thin films with a large compressive in-plane strain (-2 % for fully strained film, $a \sim 3.91$ Å) have an out-of-plane domain structure ($P4mm$ group symmetry) at RT as shown in [Section 1.2.2](#). These BaTiO₃ thin films above the critical thickness exhibit a stable ferroelectric state, where the energy gained due to ferroelectric ordering is larger than the electrostatic energy associated with the depolarizing fields due to electrical boundary conditions. However, the fundamental size effects may dramatically alter behavior in ultra-thin films because the trade-off between bulk energy gain and surface cost leads to a suppression of the phase transition to the polar phase as films become thinner. Our experimental results for BaTiO₃ thin films demonstrate surface polar distortion down to 4 ML thickness of the films, which results to upward polarization in a single domain. This suggests the existence of ferroelectricity in BaTiO₃ layers down to 4 ML, which is the lowest record of the critical thickness for ferroelectricity of BaTiO₃. To prove ferroelectricity in the ultra-thin (4 – 10 ML) BaTiO₃ films, the observation of polarization switching should be added to the structure analysis by the LEED experiment, which will be discussed in

Table 5.4: Rumpling parameters for 4 ML BaTiO₃ films.

layer	Surface of films	Surface of bulk in paraelectric phase*	Bulk
	LEED-IV exp.	DFT theory (only relaxation)	exp.**
1 st , $\eta(\text{BaO})$	- 0.0083 \pm 0.0170	+ 0.0151	\pm 0.0240
2 nd , $\eta(\text{TiO}_2)$	- 0.0342 \pm 0.0170	- 0.0046	\pm 0.0285
3 rd , $\eta(\text{BaO})$	- 0.0135 \pm 0.0268	+ 0.0039	\pm 0.0240
4 th , $\eta(\text{TiO}_2)$	- 0.0341 \pm 0.0340		\pm 0.0285

* Ref. [4] and [136].

** Ref. [138].

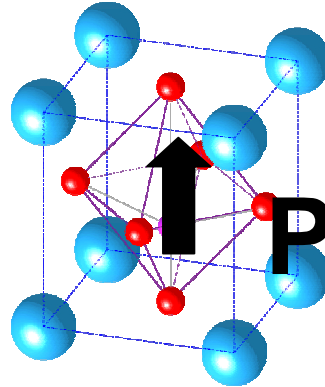


Figure 5.14: Polarization in 4 ML BaTiO₃ films.

Chapter 6. Note that, as mentioned in Section 1.3, the first principle calculations in Ref. [8] show a critical thickness of 6 unit cells for $\text{SrRuO}_3/\text{BaTiO}_3/\text{SrRuO}_3$, which is lowest expectation so far. The difference between theoretical expectation and experimental results may come from the following reasons: (1) fully strained films used in the experiment gives stronger energy for ferroelectric ordering, (2) the different terminations of films (TiO_2 termination in theory and BaO termination in experiment) have the different ferroelectric distortion, or (3) the reducing depolarizing field occurs in the experimental case (even though no top electrode does not exit in our films) due to an imperfectly clean surface, surface defects, or compensated LEED electrons on the surface.

The surface structure of BaTiO_3 films at LT

Based on the first principles DFT calculations, a phase diagram, i.e., a representation of stable ferroelectric phases and domain structures as a function temperature and strain, is constructed and shown in Section 1.2.2. Under sufficiently large compressive in-plane strains such as -2%, the ferroelectric phase at low temperature (~ 130 K) is expected to have tetragonal symmetry with polarization orthogonal to the film/substrate interface. To confirm this structure symmetry at LT, fully strained 4 ML thick BaTiO_3 films with upward polarization domain at RT were cooled down to ~ 130 K and LEED I-V data were taken at this low temperature. After the structural refinement spectra were calculated, an R_p factor for the best fit model was obtained as 0.45 ± 0.05 . Compared to the structure of 4 ML BaTiO_3 films at RT, a little stronger surface polar distortion was still obtained at low temperature with upward polarization phase as

expected to the theoretical phase diagram. However, the uncertainties increase due to a relatively poor value of R_p factor (0.45). This value makes it difficult to pinpoint the exact displacement of atoms and the strength of polar distortion at this temperature. Nevertheless, the data is consistent with an upward polarization normal to the surface.

5.2.2.2 The surface of BaTiO₃ exposed to H₂O

For size effects of thin film ferroelectricity, the role of uncompensated charge density on ferroelectric surfaces has been debated for 50 years. Uncompensated charge changes the surface free energy scale with volume and alters the stability of ultra-thin polar films. It is known that uncompensated surface charges form measurable stray fields that are non-local and controlled by screening of the polarization on ferroelectric surfaces [139]. However, there is little experimental information on the atomic mechanisms behind the polarization screening behavior in ferroelectrics, in part because the surface environment has seldom been controlled. To understand this mechanism, we investigate the changes of structure with polar phase in ferroelectric BaTiO₃ films due to surface compensation by ionic adsorption or desorption. For relatively thick ferroelectric films exposed to ambient atmosphere, there is strong experimental evidence for surface compensation by ionic adsorption [5,140,141,142]. In this section, we show the controlled interaction of H₂O with the surface of ultra-thin ferroelectric BaTiO₃ films with polar phase, which provides a better understanding of atomic mechanisms behind the polarization screening behavior in ferroelectrics.

As shown in the previous section, 10 ML thick BaTiO₃ films with clean surface

have upward polar structure in the subsurface region, determined by LEED I-V. Using *in-situ* LEED I-V measurements we study the structure change of 10 ML thick polarized BaTiO₃ films with surfaces exposed to a controlled water vapor environment. For this experiment, the sample was transferred from the growth chamber to the load lock, in which a high pressure H₂O vapor can be introduced, with high vacuum condition (1×10^{-8} Torr) base pressure. H₂O vapor was introduced at 10^{-4} Torr for 3 min, 10 min, 20 min, and 1 hour respectively. After each end of exposure times, samples were transferred into the analysis chamber with UHV conditions to measure LEED patterns and I-V curves for comparison with those of the clean samples.

Very interestingly, (1x1) LEED patterns were retained as shown in [Figure 5.15](#) even after the samples were exposed to H₂O vapor up to 1 hour (3.6×10^5 L). The observation of sharp LEED patterns indicates that the surface, even though it was exposed to H₂O vapor, retains *P4mm* group symmetry with well ordered structural condition. However, [Figure 5.16](#) shows experimental I-V curves of samples without and with H₂O exposure (10 min exposure = 6×10^4 L) have significantly different shapes, which demonstrates that the surface structure has been changed within *P4mm* symmetry due to exposure of H₂O vapor. The change of I-V curves was not observed until 3 min exposure time. Once LEED intensity is changed by exposure time of 10 min as shown in [Figure 5.16](#) - two different patterns shown in [Figure 5.15\(a\) and \(b\)](#), a longer exposure time (1 hour) does not change intensities at each energy shown in [Figure 5.15\(b\) and \(c\)](#), indicating saturated surface conditions. This LEED experiment suggests that several possible conclusions can be considered to understand the mechanism during the exposure to H₂O. First, it appears only a single ordered H₂O layer is adsorbed epitaxially on the

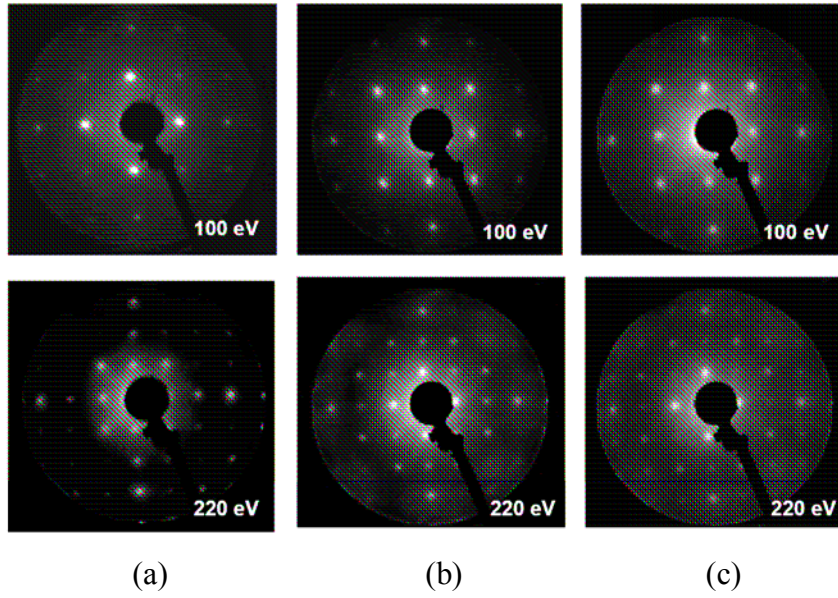


Figure 5.15: LEED patterns for BaTiO₃ films. Images were taken (a) without exposure to H₂O, (b) with exposure to H₂O for 10 min, and (c) with exposure to H₂O for 1 hour.

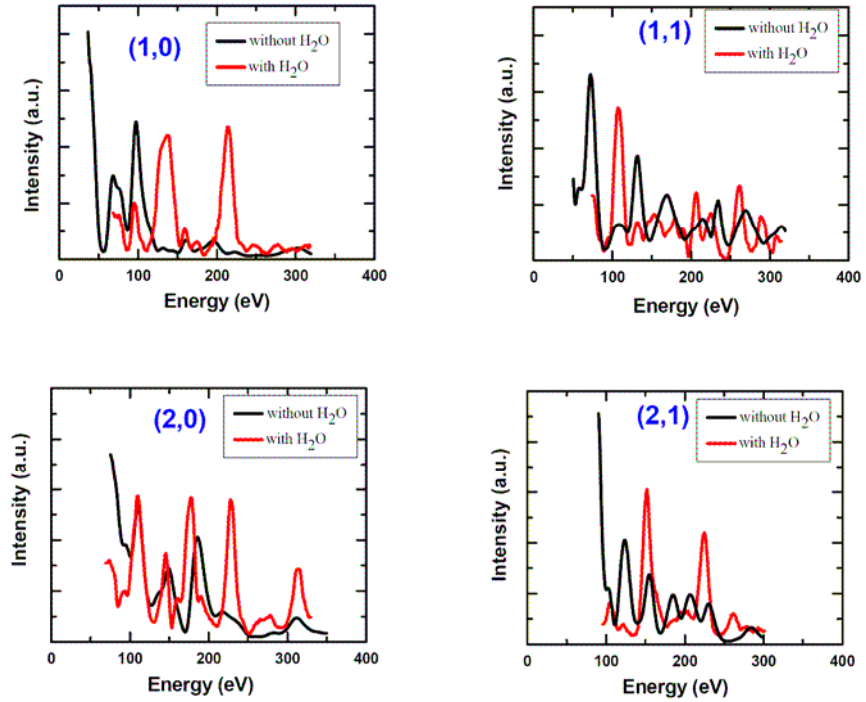


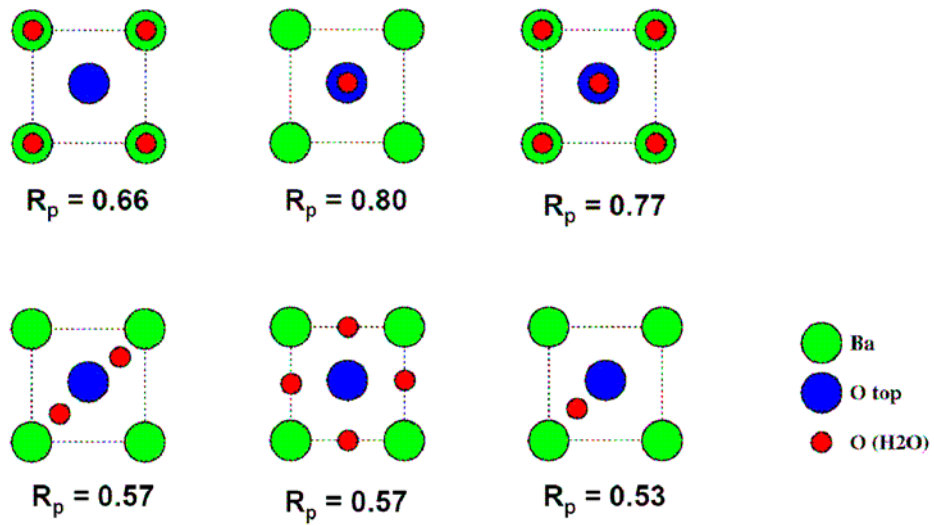
Figure 5.16: Experimental I-V curves of 10 ML BaTiO₃ films without and with exposure to H₂O.

clean BaTiO₃ surface. A second H₂O layer should form an ice structure, which is not consistent with LEED symmetry observations. More than a third layer of H₂O deposition is very unlikely unless a new form of water grows epitaxially. As simple models of absorption shown in Figure 5.17(a), only fractional occupancy of an oxygen or OH adsorbate may be introduced on top of the BaO plane. Hydrogen can be neglected in LEED because only oxygen scatters electrons significantly. Figure 5.17(a) exhibits some R_p factors for models corresponding to different locations of oxygen adsorbates. The R_p factors from these models remain large, which cannot be accepted. The best fits come from a model which assumes that H₂O vapor may partly capture ionic oxygen from the top layers of films - desorption of ionic oxygen from the clean surface:



resulting in an oxygen occupancy in the top BaO layer which is less than 1. Figure 5.17(b, left) shows that a 30 % oxygen occupancy in the top layer has the lowest R_p of 0.39. The best fit retains 100 % Ba occupancy [Figure 5.17(c)]. Compared to exposed films, Figure 5.17(b, right) shows that the clean sample without exposure to H₂O has the minimum R_p factor at 100 % oxygen occupancy. In Table 5.5 and Figure 5.18, the detailed vertical displacements of the atoms in the surface layers exhibit after determined by the structure refinement. The comparison between theoretical and experimental I-V curves for this structure is presented in Figure 5.19.

From the best fit structure, with 30 % oxygen occupancy on the top layer, we found the very interesting rumpling parameters shown in Table 5.6 and Figure 5.20. The surface polar distortion is still observed, with the exception of for the top defect layer but its direction is reversed to that in the surface without H₂O exposure, i.e., polarization is



(a)

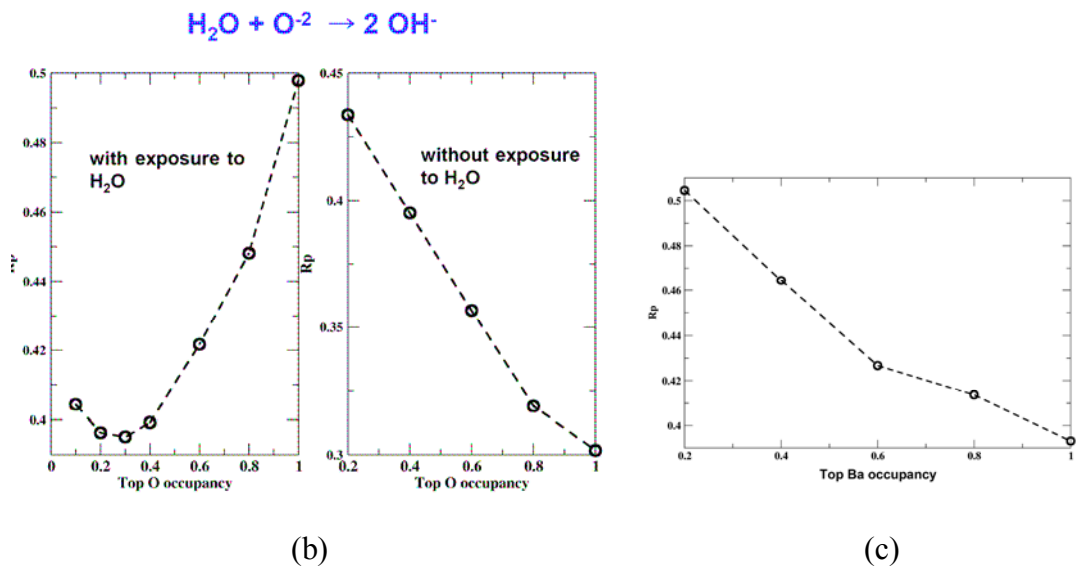


Figure 5.17: Optimizing R_p factors: (a) absorption of ionic oxygen from H_2O and desorption of (b) oxygen or (c) barium from BaO terminated BaTiO_3 films.

Surface

$Z=0$

z_1 z_2 z_3 z_4 z_5 z_6 z_7 z_8

x_1 x_2 x_3

Ba Ti O

Table 5.5: Final structure refinement for 10 ML BaTiO₃ films exposed to H₂O (final R_p = 0.39).

Z_1	$0.0155 \pm 0.03 \text{ \AA}$
Z_2	$-0.0053 \pm 0.08 \text{ \AA}$
Z_3	$2.1136 \pm 0.03 \text{ \AA}$
Z_4	$2.0527 \pm 0.06 \text{ \AA}$
Z_5	$4.1100 \pm 0.08 \text{ \AA}$
Z_6	$3.9299 \pm 0.09 \text{ \AA}$
Z_7	$6.3236 \pm 0.05 \text{ \AA}$
Z_8	$6.2327 \pm 0.12 \text{ \AA}$

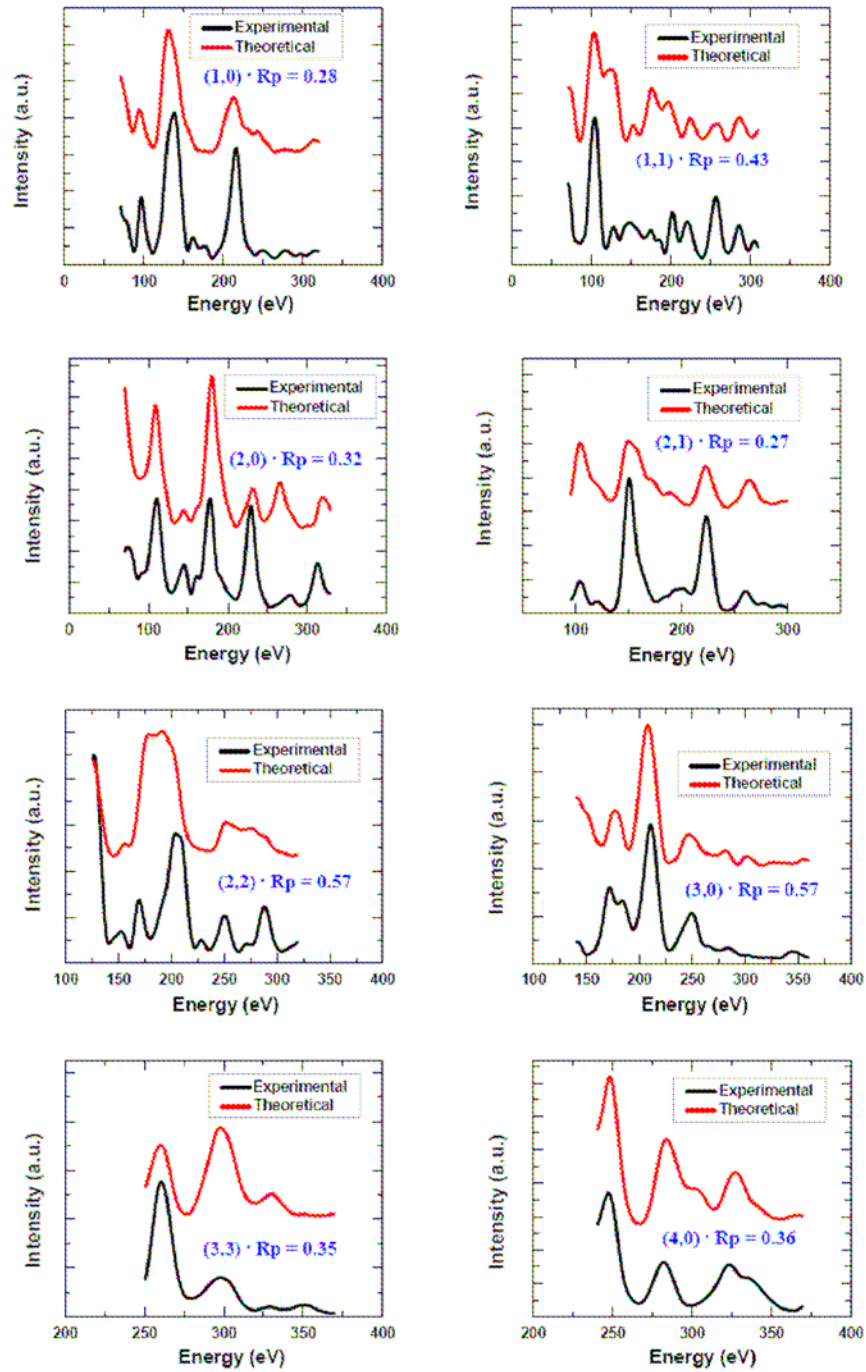


Figure 5.19: I-V curves of BaTiO₃ films exposed to H₂O.

Table 5.6: Rumpling parameters for BaTiO₃ films exposed to H₂O.

layer	Surface of films	Bulk
	LEED-IV exp.	exp.**
1 st , $\eta(\text{BaO})$	+ 0.0050 \pm 0.0262	± 0.0240
2 nd , $\eta(\text{TiO}_2)$	+ 0.0145 \pm 0.0215	± 0.0285
3 rd , $\eta(\text{BaO})$	+ 0.0430 \pm 0.0406	± 0.0240
4 th , $\eta(\text{TiO}_2)$	+ 0.0217 \pm 0.0406	± 0.0285

* Ref. [4] and [136].

** Ref [138].

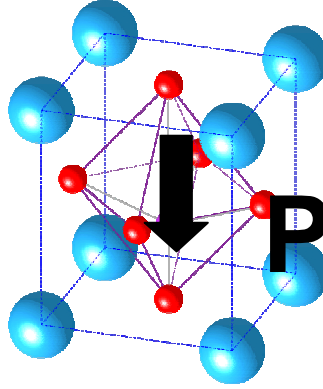


Figure 5.20: Polarization in BaTiO₃ films exposed to H₂O.

now downward. This suggests that negatively charged oxygen deficiencies on the surface affect the polarization state in several top layers, probably resulting from the inversion of dipole moments in ultra-thin films. Interestingly, the structure with 60 % oxygen occupancy, which does not fit as well in the experiment results ($R_p = 0.42$), has a non-polar state (not shown). This may be reasonable because the intrinsic electric field in the films with 60 % occupancy is stronger than that in the films with clean surface but weaker than that in the films with 30 % occupancy. These phenomena probably demonstrate indirectly that surface polar distortion in ultra-thin BaTiO_3 films can be switched by an external electric field. These results are consistent with other recent reports in which Wang *et al.* show that ferroelectric switching in 10 nm thick PbTiO_3 films as a function of vapor environment using *in-situ* grazing-incidence synchrotron x-ray scattering [143,144].

In conclusion, the exposure of the ferroelectric films to ambient atmosphere with H_2O vapor can affect the polarization status in sub-surface layers due to surface compensation. However, the optimal R_p factor of 0.39 after the final refinement is still slightly high, and the exact structure and the strength of polar distortions appear complex and have not yet been determined.

5.2.3 The surface reconstruction of 1~2 ML BaTiO_3 films

As has been shown in the previous section, surface polar distortions were observed down to 4 ML thick BaTiO_3 films. Now, we might be asked if much thinner BaTiO_3 films such as 1 ~ 2 ML thickness still have polar state or become unstable due to

size effects. To address this question, 1 – 2 ML (1 ML and 70 % covered films as the second layer) thick BaTiO₃ films grown on SrRuO₃/SrTiO₃ were investigated by LEED experiments. [Figure 5.21](#) shows quite different p(2x2) reconstruction LEED pattern of 1 – 2 ML thick BaTiO₃ films compared to (1x1) pattern of thicker (4 ML) films. This diffraction pattern looks similar to the p(2x2) LEED pattern of SrRuO₃ films. One possibility is that the diffraction of the buried SrRuO₃ structure is observed through the thin BaTiO₃ film. However, the intensity of the additional diffraction suggests that the structure of 1 – 2 ML thick BaTiO₃ films may also be affected by the SrRuO₃ films grown as bottom electrode.

For comparison, experimental I-V curves for 1 – 2, 4, and 10 ML thick BaTiO₃ films are shown in [Figure 5.22](#). As expected by the differing LEED patterns, I-V curves for 1-2 thick films are different from those of thicker films, especially positions of peak intensity, whereas I-V curves for 4 and 10 ML thick films are very similar. This suggests that surface polar distortions observed in 4 and 10 ML thick films might be absent or modified in 1-2 ML thick films due to film reconstruction or rather than by intrinsic instability by a depolarization field effect. To determine this, structure refinement was performed with several models. The structure in this film is more complicated than thicker films (≥ 4 ML). In view of the complexity, the best fit R_p factor of 0.52 can imply some information of structure but not a full description of structure. In this case, results show the Ti atoms displace upward and perhaps there is still polarization in the final structure refinement.

The observation of reconstruction in 1-2 ML thick films suggests other structural possibilities not found in 4 and 10 ML films such as tilt and rotation of octahedra in

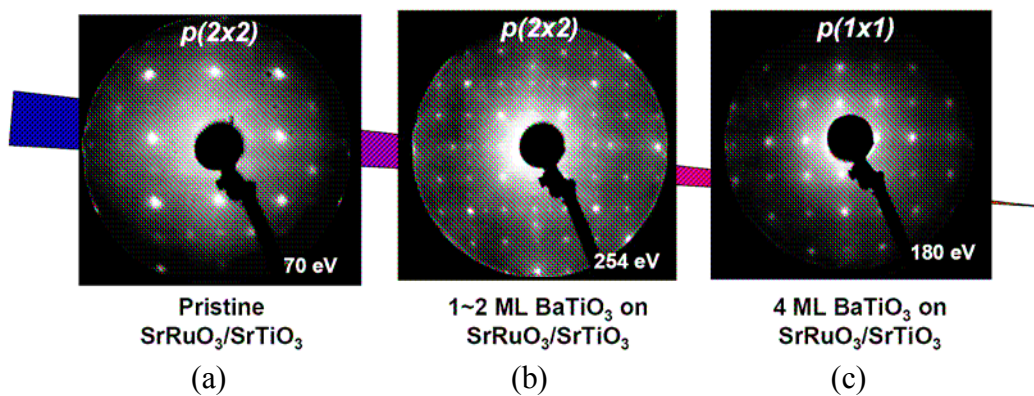


Figure 5.21: Evolution of LEED patterns dependent on BaTiO_3 film thickness.

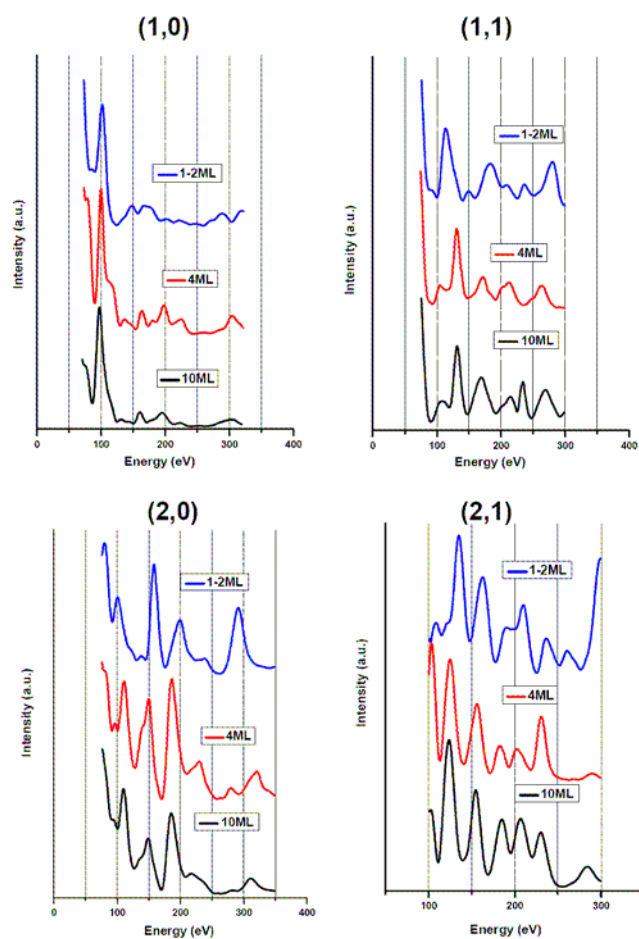


Figure 5.22: Experiment I-V curves of different thick BaTiO_3 films.

BaTiO₃ films due to the SrRuO₃ electrode. Future refinement may need to consider this possibility for the better refinement. However, a major blockade to determining the structure of 1-2 thick BaTiO₃ films is that the exact information of the p(2x2) reconstruction surface of SrRuO₃ films with randomly ordered defects is also unknown.

Interface structure between BaTiO₃ and SrRuO₃ films

To understand the structure of 1 – 2 ML thick BaTiO₃ films, we have investigated the interface between BaTiO₃ and SrRuO₃ films. For a 10 ML thick BaTiO₃ film grown on SrRuO₃/SrTiO₃ a Z-contrast STEM of a cross-sectional sample is shown in [Figure 5.23](#). As shown in [Figure 5.23\(bottom\)](#), Ti and Ru layers appear well separated in view of the uniformly distributed intensities. The gradually sloping intensities in the profile result from a decreasing specimen thickness towards the edge. However, unlike Ti and Ru layers, the Ba^{*} layer at the interface has a significantly lower intensity than the rest of the Ba rows, which suggests that the first monolayer of BaTiO₃ is Ba deficient and has mixed stoichiometry of SrO/BaO. Unfortunately, Ti layers have the least bright of the lot because the tilt is not perfect for Z contrast. This is a technical problem in optimizing tilt for the substrate instead of the very thin film itself. However, weak Ti layers can be seen in the image and it would be very obvious if they were Ru layers instead.

The most probable conclusion on the nature of the defects in epitaxially grown SrRuO₃ films is that these are SrO ad-atoms. In other words, the surface layer is depleted of volatile Ru oxides coming from ceramic SrRuO₃ target and hence excess SrO makes an ad-layer on SrO termination of the SrRuO₃ films. After BaTiO₃ growth on this defect filled surface, the result is a mixed layer at the interface with both Sr and Ba oxide.

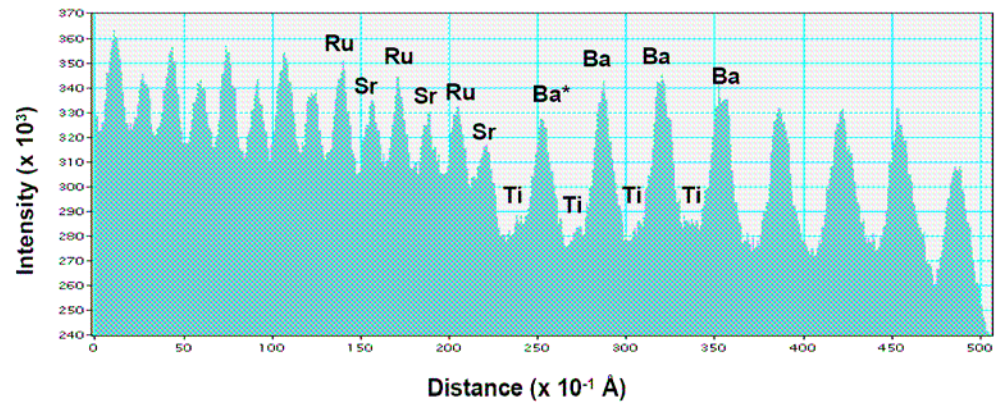
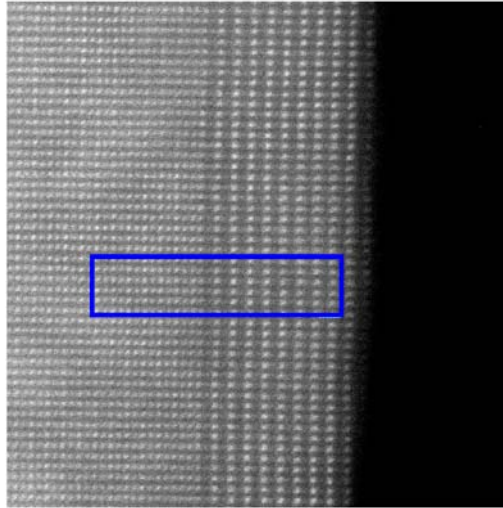


Figure 5.23: STEM for 10 ML BaTiO₃ films on SrRuO₃/SrTiO₃.

Chapter 6

Ferroelectric tunnel junctions at the nanoscale and future directions

6.1 Ferroelectricity of ultra-thin BaTiO₃ films

The observation of surface polar distortion in ultra-thin BaTiO₃ films cannot guarantee the ferroelectricity of the films. To demonstrate the existence of ferroelectricity, a spontaneous electric dipole moment must be reoriented from one crystallographic direction to another by an applied electric field, which means that the polar structure should be switchable to opposite directions. For this reason, we study ferroelectric tunneling effects (FTE), which should exhibit different tunneling current dependent on the direction of the polarization in a ferroelectric tunnel junction (FTJ) in [Section 1.4](#).

Due to the difficulties in fabrication of ultra-thin FTJ, experimental studies of the tunneling across ferroelectric barriers have just started [\[65\]](#). All experiments to date have been on micron scale junctions with possible inhomogeneous interfaces and defects. In [Ref. \[65\]](#), 4 ~ 6 nm thick PZT thin films with 4 ~ 200 μm^2 junction area were used to get hysteretic I-V curves for asymmetric electrodes (Pt and SrRuO₃ electrodes). According to observed I-V characteristics, the resistive switching was seen at the critical voltage due to polarizing reversal. These experimental results show that the theoretical approach using the converse piezoelectric effect can be reliable but did not provide clear

evidence on the effect of the depolarization field. Private discussion with the authors suggests that the hysteretic I-V curve in [Ref. \[65\]](#) is very difficult to reproduce.

To get reproducible results, we chose to make nanoscale measurements to avoid the leakage current due to film defects and to tunnel through a homogenous film. Therefore, we need to observe results for I-V characteristics using a local measurement such as SPM. This should produce a local tunneling current dependent on polarization due to the converse piezoelectric effect in ferroelectric materials. If we choose several different electrodes (still symmetric), we might observe much clearer converse piezoelectric effect by tracing the I-V curves. To observe the evidence on the depolarization field effect, we can use different top electrodes (from bad metal to good metal) with fixed bottom electrode (SrRuO_3). With asymmetric electrodes, we might observe conductance changes at zero voltage (no converse piezoelectric effect) reflecting the different potential profile seen by transport electrons for the two opposite polarization orientation. These experiments make it possible to understand the physical phenomena of electron transport by tunneling through a FTJ with ultra-thin barriers and its dependence on the polarization state of the barrier.

For this experimental measurement, we used ultra-thin (4~10 ML) BaTiO_3 films grown on $\text{SrRuO}_3/\text{SrTiO}_3$ with upward polar state in the sub-surface confirmed by LEED-IV experiments described above. The bottom electrode was conductive 15 nm thick SrRuO_3 films, whereas there is no top electrode – a vacuum gap behaves as top electrode. Therefore, our experiment corresponds to an asymmetric FTJ. Tunneling current (I-V curve) was measured using *in-situ* UHV STM. Compared to the previous work [\[65\]](#), our experiment was done by local measurement and with thinner ferroelectric

films, which should provide more reproducible measurement. As shown in [Figure 6.1](#), the bottom electrode SrRuO₃ films were connected to the sample plate through clips and screw for ground. When a chemically etched W-tip is biased, a net current of electrons flows through the ultra-thin BaTiO₃ films to ground by tunneling. A typical I-V characteristic of 4 and 10 ML thick BaTiO₃ films was obtained at RT. The data were taken in voltage steps of 0.05 V from +3 V to -3 V for backward I-V curve and then from -3 V to +3 V for forward I-V curve without stopping. Acquisition time of each data was 640 μ s with delay time of 200 μ s. Total time for one complete cycle was \sim 250 ms.

[Figure 6.2](#) shows the interesting features in the I-V curves of both 4 and 10 ML thick films, i.e., clear switching events at $\pm 2 \sim 3$ V and a crossover at the origin, which displays similar shapes as expected in theoretical approaches (asymmetric shape). As shown in [Figure 6.2](#), switching events in backward bias occur only negative voltage region (+2 \sim 3 V) whereas those in forward bias occur only positive region. This indicates that initially upward polarization changes to downward at the negative coercive voltage. However, when voltage is applied from negative to positive, downward polarization switches to upward at positive coercive voltage. These switching events provide the evidence of the hysteresis phenomena observed in ultra-thin BaTiO₃ films. Interestingly, these switching events could not be observed in every I-V loops and positions, which suggests that the features of STS data might have the stochastic nature of switching just a few unit cells. This is probably possible because the signal generation volume in STS is very small, resulting in the free energy landscape is much shallower and the path between initial and final state can meander subject to thermal disorder.

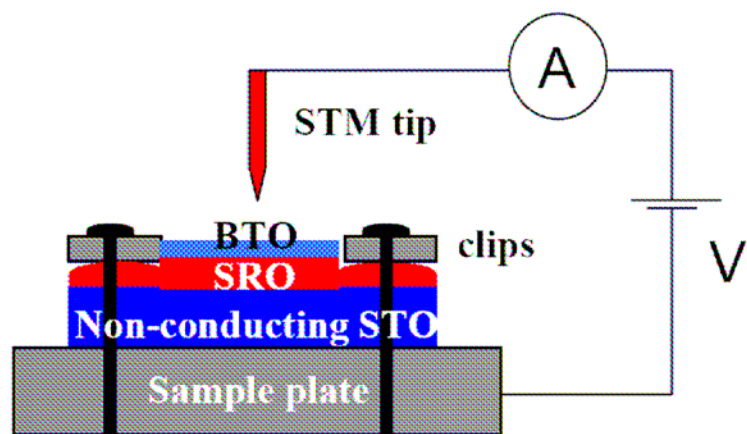


Figure 6.1: Experimental setting for FTJ using STS.

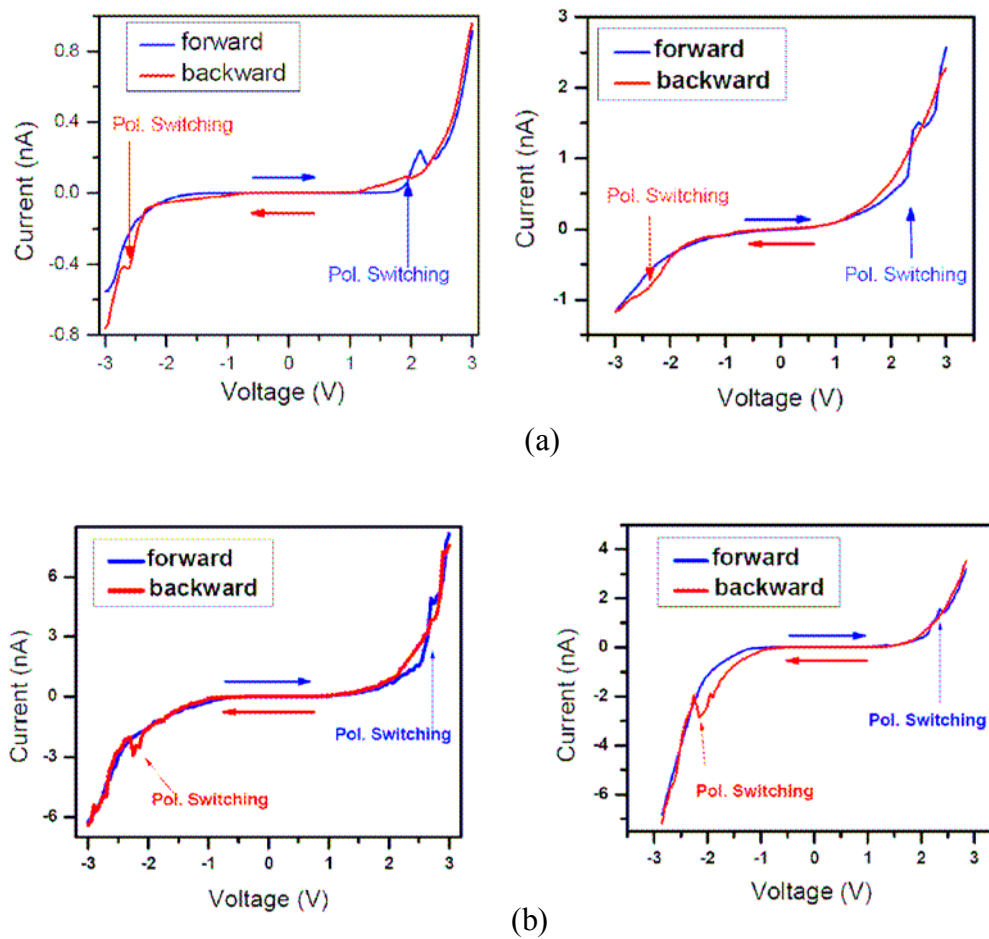


Figure 6.2: I-V curves for FTJ. Curves correspond to (a) 10 ML (b) 4 ML thick BaTiO₃ films on SrRuO₃/SrTiO₃.

Characteristics of dI/dV at coercive voltages through the local measurements were not clear probably due to very small tunneling current (a few nA).

This is reproducible as shown in Figure 6.2. All I-V curves have an asymmetric shape with similar coercive voltages. When the loop has two complete cycles shown in Figure 6.3, the repeated patterns are observed with similar results providing evidence that the spurious features seen on the I-V curves are the signature of a switching process. Indirectly, we also demonstrated this claim from no observation of these features in I-V curves of 10 ML SrTiO₃ films on SrRuO₃/SrTiO₃ in Figure 6.4, which do not have ferroelectric properties at RT.

6.2 Summary and future directions

To summarize, LEED experiment in Chapter 5 exhibits the polar state in sub-surface of the BaTiO₃ films down to 4 ML thickness. In addition, STS measurement in this Chapter indicates the polarization switching of 4 ML thick BaTiO₃ films at positive and negative coercive voltages. Through these experiments, we can say that epitaxial grown BaTiO₃ films have ferroelectricity down to 4 ML thickness, which is thinner than the theoretical expectation [8]. This may result from different strained and terminated films, or reducing depolarizing field in the films. Interestingly, 1~2 ML thick BaTiO₃ films have quite different structure and properties compared to thicker films, which may cause to lose ferroelectricity, due to reconstruction or the mixed stoichiometry, whereas the previous reports described that the critical thickness mostly comes from the imperfect screening of the depolarization field. This is very interesting and quite different reason

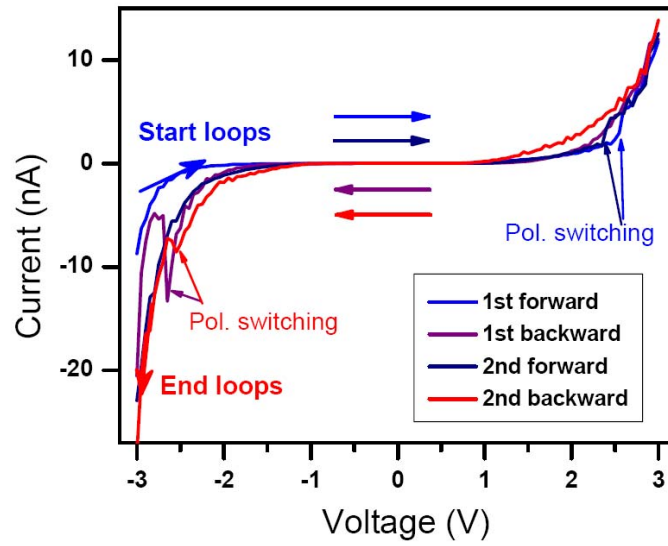


Figure 6.3: Two loops of I-V curves for FTJ. Curves correspond to 4 ML thick BaTiO₃ films on SrRuO₃/SrTiO₃.

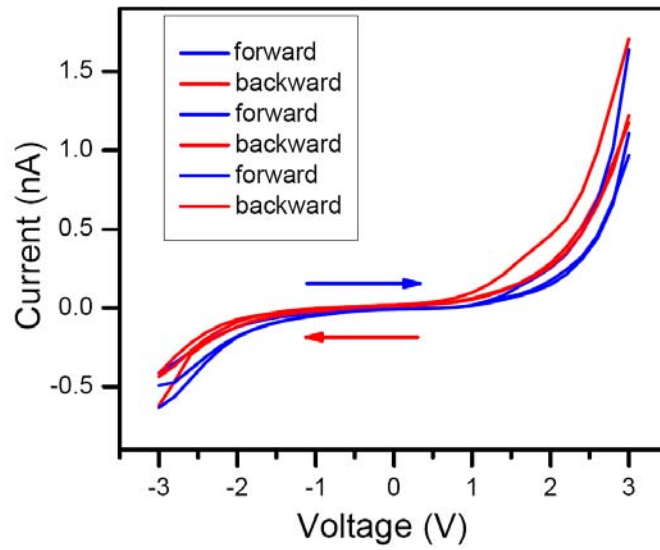


Figure 6.4: IV curves of non-ferroelectric 10 ML SrTiO₃ films on SrRuO₃/SrTiO₃.

for the existence of critical thickness, leads to more incentive study required. The polarized BaTiO₃ films with surfaces exposed to a controlled water vapor environment show that the polarization direction in sub-surface layers can be reversed by surface compensation.

Due to difficulty in cleaning the surface of non-cleavable TMOs with a 113-perovskite structure, very little information on surface structure and its properties is known so far. One of the great possible approaches to investigate the surface of non-cleavable TMOs is characterization through *in-situ* synthesis. Especially the ferroelectric transitions and transport properties in ultra-thin films must be explored with *in situ* techniques highly sensitive to the surface after careful synthesis. This dissertation shows very interesting and successful results of ultra-thin ferroelectric films with conductive bottom electrode by *in-situ* characterization, which suggest that this new approach for studying non-cleavable TMOs is very prospective in the future works.

Beyond this dissertation, we have several assignments left for ultra-thin ferroelectric films, which is very important to understand their fundamental physical properties. First, the features of STS data in Section 6.1 were stochastic. In comparison, other measurements such as ambient piezoresponse force microscopy have very reproducible hysteresis loops in the fine structure [145]. For this view, we might need more statistical STS data to understand stochastic behavior for ferroelectric polarization switching. The second is the study of symmetric FTJ using SrRuO₃ films grown on ferroelectric films or conductive tip in vacuum AFM as a top electrode. Compared to this symmetric FTJ, we can understand more clearly the general characteristics in transport properties by tunneling current dependent on ferroelectric polarization switching. The

other important issue is the understanding reconstruction of 1~2 ML thin film, which may change the physical properties of the material by the effect of the films below or substrate, i.e., the rotation and tilt of the octahedra in ultra-thin BaTiO₃ film or polar distortion in ultra-thin SrRuO₃ films.

References

- [1] L.D. Landau, *Phys. Z. Sowjun* **11**, 545 (1937).
- [2] M.E. Lines, and A.M. Glass, *Principles and Applications of Ferroelectrics and Related Materials*, Clarendon press, Oxford, 1977.
- [3] D.D. Fong, *et al.*, Ferroelectricity in ultrathin perovskite films. *Science* **304**, 1650 (2004).
- [4] B. Meyer, and D. Vanderbilt, Ab initio study of BaTiO₃ and PbTiO₃ surfaces in external electric fields. *Phys. Rev. B* **6320**, 205426 (2001).
- [5] T. Tybell, *et al.*, Ferroelectricity in thin perovskite films. *Appl. Phys. Lett.* **75**, 856 (1999).
- [6] Y.S. Kim, *et al.*, Critical thickness of ultrathin ferroelectric BaTiO₃ films. *Appl. Phys. Lett.* **86**, 102907 (2005).
- [7] V. Nagarajan, *et al.*, Size effects in ultrathin epitaxial ferroelectric heterostructures. *Appl. Phys. Lett.* **84**, 5225 (2004).
- [8] J. Junquera, and P. Ghosez, Critical thickness for ferroelectricity in perovskite ultrathin films. *Nature* **422**, 506 (2003).
- [9] P. Ghosez, and K.M. Rabe, Microscopic model of ferroelectricity in stress-free PbTiO₃ ultrathin films. *Appl. Phys. Lett.* **76**, 2767 (2000).
- [10] S.K. Streiffer, *et al.*, Observation of nanoscale 180 degrees stripe domains in ferroelectric PbTiO₃ thin films. *Phys. Rev. Lett.* **89**, 067601 (2002).
- [11] C.H. Ahn, *et al.*, Ferroelectricity at the nanoscale: Local polarization in oxide thin films and heterostructures. *Science* **303**, 488 (2004).
- [12] C.G. Duan, *et al.*, Interface effect on ferroelectricity at the nanoscale. *Nano Lett.* **6**, 483 (2006).

- [13] N. Sai, *et al.*, Ferroelectricity in ultrathin perovskite films. *Phys. Rev. B* **72**, 020101 (2005).
- [14] J. Valasek, Piezo-Electric and Allied Phenomena in Rochelle Salt. *Physical Review* **17**, 475 (1921).
- [15] I.V. Kurchatov, *Segnetoelektriki*, Moscow, 1933.
- [16] P.R. Courtney, and K.G. Brand, *Nature* **157**, 297 (1946).
- [17] B.M. Wul, and J.M. Goldman, *Dolk. Akad. Navk. S.S.S.R* **46**, 154 (1945).
- [18] S. Miyake, and R. Ueda, *J. Phys. Soc Japan* **1**, 32 (1946).
- [19] A.F. Devonshire, *Philosophical Magazine* **40**, 1040 (1949).
- [20] O. Dieguez, *et al.*, First-principles study of epitaxial strain in perovskites. *Phys. Rev. B* **72**, 144101 (2005).
- [21] D. Damjanovic, Ferroelectric, dielectric and piezoelectric properties of ferroelectric thin films and ceramics. *Rep. Prog. Phys.* **61**, 1267 (1998).
- [22] R.E. Waser, *Nanoelectronics and information technology*, WILEY-VCH, Aachen, Germany, 2003.
- [23] V.L. Ginzburg, *Zh. Eksp. Teor. Fiz.* **15**, 739 (1945).
- [24] M.J. Haun, *et al.*, Thermodynamic Theory of the Lead Zirconate-Titanate Solid-Solution System. *Ferroelectrics* **99**, 63 (1989).
- [25] N.A. Pertsev, *et al.*, Effect of mechanical boundary conditions on phase diagrams of epitaxial ferroelectric thin films. *Phys. Rev. Lett.* **80**, 1988 (1998).
- [26] N. Grandjean, and J. Massies, Extension of the Layer-by-Layer Growth Regime of $\text{In}_x\text{Ga}_{1-x}\text{As}$ on GaAs (001). *Semicond. Sci. Technol.* **8**, 2031 (1993).
- [27] M.G. Lagally, and Z.Y. Zhang, Materials science - Thin-film cliffhanger. *Nature* **417**,

907 (2002).

- [28] Schwoebe.RI, Step Motion on Crystal Surfaces. *J. Appl. Phys.* **40**, 614 (1969).
- [29] S.J. Liu, *et al.*, Schwoebel-Ehrlich barrier: from two to three dimensions. *Appl. Phys. Lett.* **80**, 3295 (2002).
- [30] K. Sangwal, and R. Rodriguez-Clemente, *Surface Morphology of Crystalline Solids*, Trans Tech, Zurich, 1991.
- [31] J.S. Horwitz, and J.A. Sprague, *Pulsed Laser Deposition of Thin Films*, Wiley, New York, 1994.
- [32] M.Y. Zhuravlev, *et al.*, Giant electroresistance in ferroelectric tunnel junctions. *Phys. Rev. Lett.* **94**, 246802 (2005).
- [33] H. Kohlstedt, *et al.*, Theoretical current-voltage characteristics of ferroelectric tunnel junctions. *Phys. Rev. B* **72**, 125341 (2005).
- [34] E.Y. Tsybal, and H. Kohlstedt, Applied physics - Tunneling across a ferroelectric. *Science* **313**, 181 (2006).
- [35] R.E. Cohen, Origin of Ferroelectricity in Perovskite Oxides. *Nature* **358**, 136 (1992).
- [36] R.S. Beach, *et al.*, Enhanced Curie Temperatures and Magnetoelastic Domains in Dy/Lu Superlattices and Films. *Phys. Rev. Lett.* **70**, 3502 (1993).
- [37] J. Wang, *et al.*, Epitaxial BiFeO₃ multiferroic thin film heterostructures. *Science* **299**, 1719 (2003).
- [38] J.H. Haeni, *et al.*, Room-temperature ferroelectricity in strained SrTiO₃. *Nature* **430**, 758 (2004).
- [39] K.J. Choi, *et al.*, Enhancement of ferroelectricity in strained BaTiO₃ thin films. *Science* **306**, 1005 (2004).

- [40] H.N. Lee, *et al.*, Strong polarization enhancement in asymmetric three-component ferroelectric superlattices. *Nature* **433**, 395 (2005).
- [41] V.G. Koukhar, *et al.*, Thermodynamic theory of epitaxial ferroelectric thin films with dense domain structures. *Phys. Rev. B* **64**, 214103 (2001).
- [42] O. Dieguez, *et al.*, Ab initio study of the phase diagram of epitaxial BaTiO₃. *Phys. Rev. B* **69**, 212101 (2004).
- [43] W. Zhong, *et al.*, Phase-Transitions in BaTiO₃ from First Principles. *Phys. Rev. Lett.* **73**, 1861 (1994).
- [44] Y. Maeno, *et al.*, Superconductivity in a Layered Perovskite without Copper. *Nature* **372**, 532 (1994).
- [45] D.G. Schlom, *et al.*, Growth of epitaxial (Sr,Ba)_(n+1)Ru_nO_{3n+1} films. *Supercond. Sci. Technol.* **10**, 891 (1997).
- [46] G. Cao, *et al.*, From antiferromagnetic insulator to ferromagnetic metal: a brief review of the layered ruthenates. *Mater. Sci. Eng. B-Solid State Mater. Adv. Technol.* **63**, 76 (1999).
- [47] D.J. Singh, Relationship of Sr₂RuO₄ to the Superconducting Layered Cuprates. *Phys. Rev. B* **52**, 1358 (1995).
- [48] R. Matzdorf, *et al.*, Surface structural analysis of the layered perovskite Sr₂RuO₄ by LEED I(V). *Phys. Rev. B* **65**, 085404 (2002).
- [49] R. Matzdorf, *et al.*, Ferromagnetism stabilized by lattice distortion at the surface of the p-wave superconductor Sr₂RuO₄. *Science* **289**, 746 (2000).
- [50] R. Matzdorf, *et al.* unpublished data.
- [51] L. Petersen, *et al.* unpublished data.

- [52] J. Choi, *et al.*, Growth mode transition from layer by layer to step flow during the growth of heteroepitaxial SrRuO₃ on (001) SrTiO₃. *Appl. Phys. Lett.* **79**, 1447 (2001).
- [53] A. Kanbayasi, Magnetic-Properties of SrRuO₃ Single-Crystal. *J. Phys. Soc. Jpn.* **41**, 1876 (1976).
- [54] J. Shin, *et al.*, Surface stability of epitaxial SrRuO₃ thin films in vacuum. *J. Mater. Res.* **19**, 3447 (2004).
- [55] P.B. Allen, *et al.*, Transport properties, thermodynamic properties, and electronic structure of SrRuO₃. *Phys. Rev. B* **53**, 4393 (1996).
- [56] L. Klein, *et al.*, Transport and magnetization in the badly metallic itinerant ferromagnet SrRuO₃. *J. Phys.-Condes. Matter* **8**, 10111 (1996).
- [57] A.T. Zayak, *et al.*, Structural, electronic, and magnetic properties of SrRuO₃ under epitaxial strain. *Phys. Rev. B* **74**, 094104 (2006).
- [58] J.C. Jiang, *et al.*, Domain structure of epitaxial SrRuO₃ thin films on miscut (001) SrTiO₃ substrates. *Appl. Phys. Lett.* **72**, 2963 (1998).
- [59] A.F. Marshall, *et al.*, Lorentz transmission electron microscope study of ferromagnetic domain walls in SrRuO₃: Statics, dynamics, and crystal structure correlation. *J. Appl. Phys.* **85**, 4131 (1999).
- [60] N.W. Ashcroft, and N.D. Mermin, *Solid State Physics*, Saunders College Publishing, New York, 1976.
- [61] T.M. Shaw, *et al.*, The properties of ferroelectric films at small dimensions. *Annu. Rev. Mater. Sci.* **30**, 263 (2000).
- [62] I.P. Batra, *et al.*, Depolarization Field and Stability Considerations in Thin

- Ferroelectric Films. *Journal of Vacuum Science & Technology* **10**, 687 (1973).
- [63] I.P. Batra, *et al.*, New Type of First-Order Phase-Transition in Ferroelectric Thin-Films. *Phys. Rev. Lett.* **30**, 384 (1973).
- [64] I.P. Batra, and Silverma.Bd, Thermodynamic Stability of Thin Ferroelectric Films. *Solid State Commun.* **11**, 291 (1972).
- [65] J.R. Contreras, *et al.*, Resistive switching in metal-ferroelectric-metal junctions. *Appl. Phys. Lett.* **83**, 4595 (2003).
- [66] J.R. Contreras *Ferroelectric Tunnel Junctions*. Ph.D., Universitat zu Koln (2003).
- [67] O. Auciello, *Handbook of Crystal Growth*, Elsevier Science, Amsterdam, 1994.
- [68] B.D. Cullity, and S.R. Stock, *Elements of X-ray Diffraction*, Prentice Hall, New Jersey, 2001.
- [69] B.E. Warren, *X-Ray Diffraction*, Dover Publications, 1990.
- [70] K. Ploog, Microscopical Structuring of Solids by Molecular-Beam Epitaxy - Spatially Resolved Materials Synthesis. *Angew. Chem.-Int. Edit. Engl.* **27**, 593 (1988).
- [71] C. Davission, and L.H. Germer, Diffraction of electrons by a crystal of nickel. *Physical Review* **30**, 705 (1927).
- [72] C. Davission, and L.H. Germer, The scattering of electrons by a single crystal of nickel. *Nature* **119**, 558 (1927).
- [73] http://www.fhi-berlin.mpg.de/th/lectures/summer_term_2006/merged.pdf.
- [74] http://whome.phys.au.dk/~philip/q1_05/surflec/node22.html.
- [75] K. Heinz, Leed and Dleed as Modern Tools for Quantitative Surface-Structure Determination. *Rep. Prog. Phys.* **58**, 637 (1995).

- [76] R.G. Moore *Manifestations of Broken Symmetry: The Surface Phases of $\text{Ca}_{2-x}\text{Sr}_x\text{RuO}_4$* . Ph.D., University of Tennessee (2006).
- [77] J.B. Pendry, *Low Energy Electron Diffraction*, Academic Press, New York, 1974.
- [78] M.A. Van Hove, *et al.*, *Low-Energy Electron Diffraction Experiment, Theory and Surface Structure Determination*, Springer-Verlag, Berlin, 1986.
- [79] M.A. Van Hove, and S.Y. Tong, *Surface Crystallography by LEED*, Springer-Verlag, Berlin, 1979.
- [80] J.L. Beeby, Diffraction of Low-Energy Electrons by Crystals. *Journal of Physics Part C Solid State Physics* **1**, 82 (1968).
- [81] J.B. Pendry, New Perturbation Theory for Low-Energy Electron-Diffraction Intensities. *Phys. Rev. Lett.* **27**, 856 (1971).
- [82] R.L. Park, and H.E. Farnsworth, The structure of clean nickel crystal surfaces. *Surf. Sci.* **2**, 527 (1964).
- [83] J.B. Pendry, Reliability Factors for Leed Calculations. *Journal of Physics C-Solid State Physics* **13**, 937 (1980).
- [84] G. Binnig, *et al.*, Atomic Force Microscope. *Phys. Rev. Lett.* **56**, 930 (1986).
- [85] http://en.wikipedia.org/wiki/Image:Atomic_force_microscope_block_diagram.png.
- [86] http://center.kookmin.ac.kr/Data/DataBank/spm_kor.pdf.
- [87] Q. Zhong, *et al.*, Fractured Polymer Silica Fiber Surface Studied by Tapping Mode Atomic-Force Microscopy. *Surf. Sci.* **290**, L688 (1993).
- [88] S.V. Kalinin, *et al.*, Vector piezoresponse force microscopy. *Microsc. microanal.* **12**, 206 (2006).
- [89] J. Shin, *et al.*, Simultaneous elastic and electromechanical imaging by scanning

- probe microscopy: Theory and applications to ferroelectric and biological materials. *J. Vac. Sci. Technol. B* **23**, 2102 (2005).
- [90] *Landolt-Bornstein: Numerical Data and Functional relationships in Science and Technology*, Springer, Heidelberg, 1982.
- [91] V.E. Henrich, and P.A. Cox, *The Surface Science of Metal Oxides*, Cambridge University Press, Cambridge, 1994.
- [92] M. Kawasaki, *et al.*, Atomic Control of the SrTiO₃ Crystal-Surface. *Science* **266**, 1540 (1994).
- [93] <http://lippmaa.issp.u-tokyo.ac.jp/projects/dynamics/etching/etch.html>.
- [94] H.N. Lee, *et al.*, Thermal stability of epitaxial SrRuO₃ films as a function of oxygen pressure. *Appl. Phys. Lett.* **84**, 4107 (2004).
- [95] G. Koster, *et al.*, Quasi-ideal strontium titanate crystal surfaces through formation of strontium hydroxide. *Appl. Phys. Lett.* **73**, 2920 (1998).
- [96] J. Shin, *et al.* *Layer-by-layer and Pseudo-2D growth modes for heteroepitaxial BaTiO₃ films: exploiting kinetic limitations and dislocation networks.*
- [97] G. Cao, *et al.*, Observation of itinerant ferromagnetism in layered Sr₃Ru₂O₇ single crystals. *Phys. Rev. B* **55**, R672 (1997).
- [98] W. Hong, *et al.*, Persistent step-flow growth of strained films on vicinal substrates. *Phys. Rev. Lett.* **95**, 095501 (2005).
- [99] G. Rijnders, *et al.*, Enhanced surface diffusion through termination conversion during epitaxial SrRuO₃ growth. *Appl. Phys. Lett.* **84**, 505 (2004).
- [100] T. Aytug, *et al.*, Enhancement of flux pinning and critical currents in YBa₂Cu₃O_{7-δ} films by nanoscale iridium pretreatment of substrate surfaces. *J. Appl. Phys.*

98, 114309 (2005).

- [101] H. Zheng, *et al.*, Multiferroic BaTiO₃-CoFe₂O₄ nanostructures. *Science* **303**, 661 (2004).
- [102] Y. Nomura, *et al.*, Surface-Diffusion Length of Ga Adatoms on (111)B Surfaces During Molecular-Beam Epitaxy. *Appl. Phys. Lett.* **64**, 1123 (1994).
- [103] J.F. Scott, *Ferroelectric Memories*, Springer, Germany, 2000.
- [104] J. Appenzeller, *Nanoelectronics and information technology*, Wiley-VCH, Germany, 2003.
- [105] K.-H. Hellwege, and A.M. Hellwege, (Eds.), *Landolt-Bornstein: Numerical Data and Functional relationships in Science and Technology*, Springer, Heidelberg, 1982.
- [106] T. Suzuki, *et al.*, Analysis of misfit relaxation in heteroepitaxial BaTiO₃ thin films. *Philos. Mag. A-Phys. Condens. Matter Struct. Defect Mech. Prop.* **79**, 2461 (1999).
- [107] H.P. Sun, *et al.*, Evolution of dislocation arrays in epitaxial BaTiO₃ thin films grown on (100) SrTiO₃. *Appl. Phys. Lett.* **84**, 3298 (2004).
- [108] J. Zhang, *et al.*, Structural behavior of thin BaTiO₃ film grown at different conditions by pulsed laser deposition. *Jpn. J. Appl. Phys. Part 1 - Regul. Pap. Short Notes Rev. Pap.* **36**, 276 (1997).
- [109] S.B. Mi, *et al.*, Heterostructures of BaTiO₃ bilayer films grown on SrTiO₃ (001) under different oxygen pressures. *J. Cryst. Growth* **283**, 425 (2005).
- [110] J.Q. He, *et al.*, Growth dynamics and strain relaxation mechanisms in BaTiO₃ pulsed laser deposited on SrRuO₃/SrTiO₃. *Phys. Rev. B* **73**, 125413 (2006).

- [111] A. Visinoiu, *et al.*, Initial growth stages of epitaxial BaTiO₃ films on vicinal SrTiO₃ (001) substrate surfaces. *J. Appl. Phys.* **91**, 10157 (2002).
- [112] T. Zhao, *et al.*, Thickness and oxygen pressure dependent structural characteristics of BaTiO₃ thin films grown by laser molecular beam epitaxy. *J. Appl. Phys.* **87**, 7442 (2000).
- [113] H. Shigetani, *et al.*, BaTiO₃ thin films grown on SrTiO₃ substrates by a molecular-beam-epitaxy method using oxygen radicals. *J. Appl. Phys.* **81**, 693 (1997).
- [114] J.P. Maria, *et al.*, The influence of energetic bombardment on the structure and properties of epitaxial SrRuO₃ thin films grown by pulsed laser deposition. *J. Appl. Phys.* **83**, 4373 (1998).
- [115] Y.S.e.a. Touloukian, *Thermal Expansion Nonmetallic Solids, Thermophysical Properties of matter*, IFI/Plenum, New York-Washington, 1977.
- [116] J. Shin, *et al.*, Surface stability of epitaxial SrRuO₃ films. *Surf. Sci.* **581**, 118 (2005).
- [117] C.B. Eom, *et al.*, Single-Crystal Epitaxial Thin-Films of the Isotropic Metallic Oxides Sr_{1-x}Ca_xRuO₃. *Science* **258**, 1766 (1992).
- [118] J.P. Mercurio, *et al.*, Fabrication of SrRuO₃ powders and thin films by metalorganic decomposition. *J. Alloy. Compd.* **308**, 77 (2000).
- [119] H.N. Lee, *et al.*, Ferroelectric Bi_{3.25}La_{0.75}Ti₃O₁₂ films of uniform a-axis orientation on silicon substrates. *Science* **296**, 2006 (2002).
- [120] W. Bensch, *et al.*, Structure and Thermochemical Reactivity of CaRuO₃ and SrRuO₃. *Solid State Ion.* **43**, 171 (1990).
- [121] C. Mallika, and O.M. Sreedharan, Potentiometric Determination of the

- Thermodynamic Stability of SrO-RuO₂ System. *J. Alloy. Compd.* **191**, 219 (1993).
- [122] K.T. Jacob, *et al.*, Calcium ruthenates: Determination of Gibbs energies of formation using electrochemical cells. *J. Electrochem. Soc.* **150**, E227 (2003).
- [123] A. Banerjee, *et al.*, Thermodynamic properties of SrRuO₃(s). *J. Alloy. Compd.* **353**, 263 (2003).
- [124] I. Barin, *Thermochemical Data for Pure Substances, 2nd Edition*, VCH, New York, 1989.
- [125] J.J. Randall, and R. Ward, The Preparation of Some Ternary Oxides of the Platinum Metals. *J. Am. Chem. Soc.* **81**, 2629 (1959).
- [126] Ismail, *et al.*, Surface lattice dynamics of layered transition metal oxides: Sr₂RuO₄ and La_{0.5}Sr_{1.5}MnO₄. *Phys. Rev. B* **67**, 035407 (2003).
- [127] D.A. Shirley, High-Resolution X-Ray Photoemission Spectrum of Valence Bands of Gold. *Phys. Rev. B* **5**, 4709 (1972).
- [128] P.A. Cox, *et al.*, The Metal-to-Semiconductor Transition in Ternary Ruthenium(IV) Oxides - a Study by Electron-Spectroscopy. *Journal of Physics C-Solid State Physics* **16**, 6221 (1983).
- [129] J.F. Moulder, *et al.*, *Handbook of X-ray Photoelectron Spectroscopy*, Physical Electronics, Inc., Minnesota, 1995.
- [130] S.V. Kalinin, *et al.*, Electronic transport imaging in a multiwire SnO₂ chemical field-effect transistor device. *J. Appl. Phys.* **98**, 044503 (2005).
- [131] E.W. Plummer, *et al.*, The next 25 years of surface physics. *Prog. Surf. Sci.* **67**, 17 (2001).
- [132] K. Gorbachev, and S.V. Kalinin

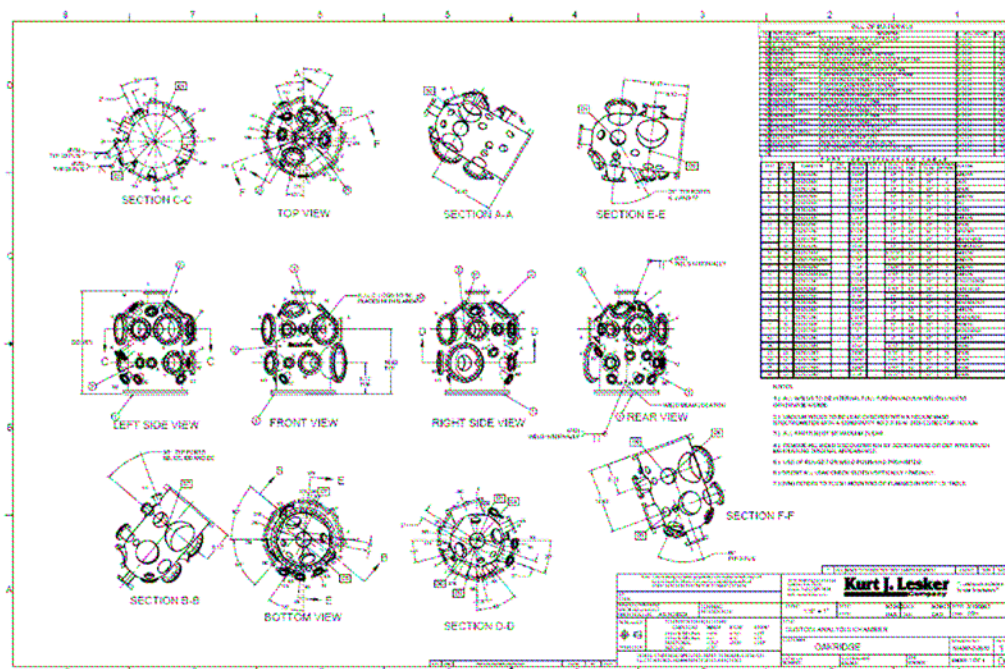
- [133] <http://www.sitp.lbl.gov/index.php?content=/leedpack/>
- [134] V.B. Nascimento, *et al.*, Procedure for LEED I-V structural analysis of metal oxide surfaces: $\text{Ca}_{1.5}\text{Sr}_{0.5}\text{RuO}_4$ (001). *Phys. Rev. B* **75**, 035408 (2007).
- [135] J. Rundgren, Optimized surface-slab excited-state muffin-tin potential and surface core level shifts. *Phys. Rev. B* **68**, 125405 (2003).
- [136] J. Padilla, and D. Vanderbilt, Ab initio study of BaTiO_3 surfaces. *Phys. Rev. B* **56**, 1625 (1997).
- [137] B. Cord, and R. Courths, Photoemission-Study of BaTiO_3 (100) Surfaces. *Surf. Sci.* **152**, 1141 (1985).
- [138] J. Harada, *et al.*, X-Ray and Neutron Diffraction Study of Tetragonal Barium Titanate. *Acta Crystallographica Section a-Crystal Physics Diffraction Theoretical and General Crystallography* **A 26**, 336 (1970).
- [139] V.M. Fridkin, *Ferroelectric Semiconductors*, Consultants Bureau, New York, 1980.
- [140] S.V. Kalinin, and D.A. Bonnell, Local potential and polarization screening on ferroelectric surfaces. *Phys. Rev. B* **63**, 125411 (2001).
- [141] S.V. Kalinin, *et al.*, Domain polarity and temperature induced potential inversion on the BaTiO_3 (100) surface. *J. Appl. Phys.* **91**, 3816 (2002).
- [142] F. Peter, *et al.*, Piezoresponse in the light of surface adsorbates: Relevance of defined surface conditions for perovskite materials. *Appl. Phys. Lett.* **85**, 2896 (2004).
- [143] R.H. Wang, *et al.*, Chemical Control of Ferroelectric Switching in PbTiO_3 films, APS meeting, Denver, CO (2007).
- [144] J. Spanier, Scanning probe microscopy of ferroelectric nanostructures, APS

meeting, Denver, CO (2007).

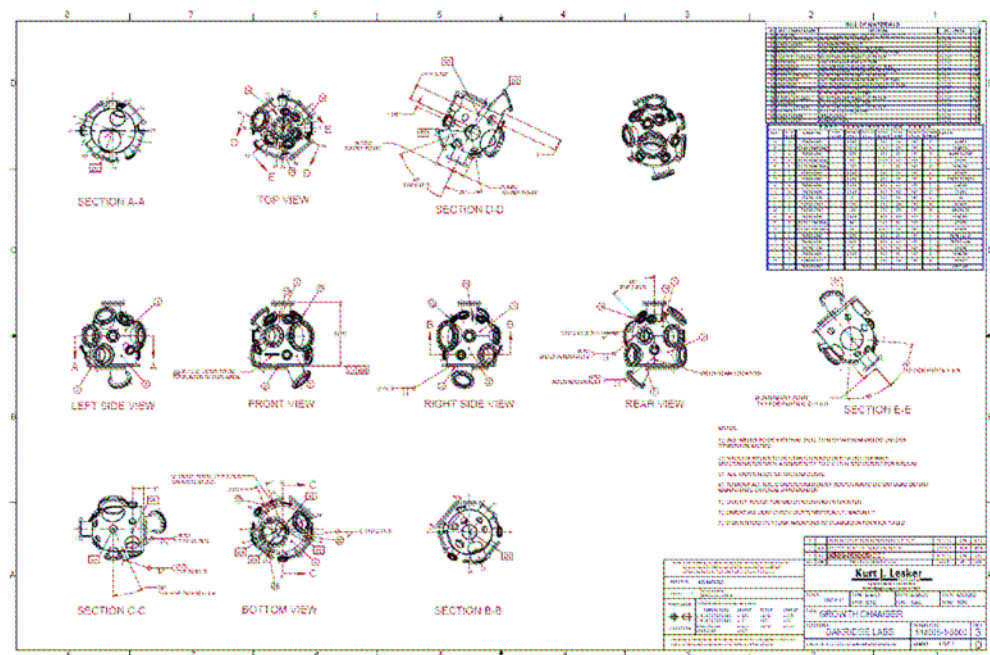
[145] S.V. Kalinin, (private communication).

Appendix

Appendix A.1. Chamber Construction



Characterization chamber



Growth chamber

Vita

Junsoo Shin was born and raised in Seoul, Korea. After graduating from Yonsan High School, he attended Yonsei University, Seoul, Korea, and received a Bachelor of Science degree in Electrical Engineering in 1990. After that, he switched his major to fundamental science and returned to Yonsei University, Seoul, Korea to study high energy physics and field theory. He earned a Masters degree in the physics department of Yonsei University in 1993. After graduation, he worked with Dr. Jae Hyung Yee as a post-master and research assistant in Yonsei University for 3 years. During the time, he studied the 2-dimensional vortex in Chern-Simons field theory.

In 1997 – 1999, he earned another masters degree in physics department at Virginia Tech, Blacksburg, VA. After graduating from Virginia Tech, he went to the University of Tennessee, Knoxville, TN to pursue his doctorate in physics. In Feb. 2002, he joined the surface science group in UT to study the surface of TMO epitaxial thin films. While as a doctoral student, he designed and built the multi-functional UHV system combined with PLD growth chamber, successfully deposited high quality epitaxial thin films, and characterized them for investigating of the ferroelectric properties at nanoscale. He completed his Doctor of Philosophy degree in Physics in May 2007.